Università degli Studi di Ferrara

DOTTORATO DI RICERCA IN
FISICA

CICLO XXVII

COORDINATORE Prof. Guidi Vincenzo

COMPARISON CALIBRATION OF LOW-COST PROTOTYPES OF ACOUSTIC PRESSURE-VELOCITY PROBES AND SOME APPLICATION CASE-STUDIES

Settore Scientifico Disciplinare FIS/07

Dottorando	**Tutore**
Dott. Buiat Martina	Prof. Stanzial Domenico

Anni 2011/2014

To my family, and to myself.

Abstract

The main topic of this work is the acoustical characterisation and the comparison calibration of a new low cost prototype of a pressure-velocity probe based on MEMS and CMOS technologies. The development during the last years of micro sensors using the double hot-wire anemometric transduction principle, has permitted to directly measure the velocity of the air particle, thus giving a fundamental contribution to the intensimetric measurements. This in turn required a more deep study of the calibration techniques as at least two acoustical signals (pressure and axial velocity) have to be processed simultaneously in order to obtain precise and affordable measurements of energetic properties of sound. In particular this work is devoted to the analysis and experimental validation of the "comparison calibration" methodology when applied to pressure-velocity probes still in their early stage of prototypes.

After an introduction on the Acoustical Energetics, in which the main quantities are described and simulated for a monochromatic field, the next chapters are dedicated to the probe realised within the SIHT (Sogliano Industrial High Technology) project, which is based on the collaboration between the Institute of Acoustics and Sensors Corbino-CNR, of the CNR-IEIIT and of the Deltatech industry in Sogliano al Rubicone (FC, Italy). We describe the different prototypes that have been realised and their relative characterization, that have been useful to design new and improved prototypes. The particular geometry of the prototypes has also required a new procedure of comparison calibration, in which the probe under test is calibrated using a reference one, in a generic field.

The possible applications of the new probe are various, and go from audiometric field to condition monitoring, and are investigated in the last chapter.

Table of contents

Introduction

During the last decades a new kind of sound intensity probes has been developed based on the direct measure of both the acoustic pressure and air particle velocity. This is mainly due to the appearance of MEMS technologies which have permitted to fabricate acoustic velocimetric microsensors, thus giving a fundamental contribution to the intensimetric measurements. In fact at the beginning only standard intensimetric probes were available, and the velocity had to be derived indirectly from the measurement of two in-phase pressure microphones.

The first producer in Europe of such probes is the Microflown Technologies, which realised an anemometer based on the transduction principle of double heated wires. The innovative nature of this probe goes with the necessity to find a new calibration method, and at present there's no a universally approved procedure.

Given the importance of the p-v probes, the CNR-IDASC at Ferrara, has realised the SIHT (Sogliano Industrial High Technology) project, in collaboration with the Deltatech industry in Sogliano al Rubicone and IEIIT at Pisa. Within this project a new p-v probe has been realised. This work resumes the process of production, calibration and the applications of such probe.

The first chapter is an introduction to the Acoustical Energetics, that is the discipline studying the radiative and oscillatory fluxes of acoustic energy based on the four-dimensions formulations of the energy momentum tensor of the acoustic field. After a theoretical introduction, the acoustic energetic quantities are simulated for a monochromatic 1-D field.

The second chapter illustrates two methods of calibration of the p-v probes: the same device, a Microflown match size, has been calibrated during an interlaboratory comparison using the piston in a sphere method during my visit to Microflown (Arnhem, The Netherlands) and using the progressive plane wave calibration developed at Ferrara University.

The next chapter is dedicated to the prototypes realised during the project. The new p-v probe has been used for the realisation of a new kind of tympanometric probe: the relative characterisation and the calibration are here described. In a second moment the probe has been inserted in a carbon fibre horn that turned out to be a natural velocity amplifier. The effects of the geometry of the horn are studied through experimental measures and numerical simulations.

The comparison calibration of the prototype is described in chapter 4: the Microflown probe has been calibrated inside the Larix laboratory in Ferrara and has become the reference probe on which we calibrated the prototype.

Finally, in the last chapter, a series of case studies are illustrated. The new prototype in fact has been applied to many fields, from tympanometry to the railway safety, to the condition monitoring.

Chapter 1

Simulation of acoustic energetic quantities

The quasi-stationary plane wave is one of the most accepted models for the study of the Acoustical Energetics, that is the theoretical-experimental discipline that studies the radiative and oscillatory fluxes of acoustic energy based on the four-dimensional formulation of the energy-momentum tensor of the acoustic field. The great importance of such model comes from the necessity to quantitatively describe the phenomenon of reflection by considering each energetic implication. To this aim the various energetic quantities for a quasi-stationary plane wave have been numerically simulated and graphically visualized: in particular, we start from the simplest case of a monochromatic wave, strictly applying the methods of energetic acoustics in order to deduce conclusions which are useful for future developments.

1.1 The acousto-electro-mechanic analogy

Monochromatic plane-waves are made up of the superposition of two components, one progressive and another regressive, which represent the incident and reflected wave with the same direction but propagating in opposite ways, and with the same frequency [1]. In [2] it is clearly stated that the purely reactive (imaginary) aspect of the complex acoustic impedance is associated with the absence of net energy transport, so obtaining an image of standing waves in which the energy is delimited between the nodes of pressure and velocity into isolated cells with a back-and-forth movement. On the contrary the resistive (real) part of impedance is associated with sound energy that passes by each point in space in a series of pulses. This model has been generalised in [3] giving rise to a complete acousto-electro-mechanic analogy, where the well known concept of power factor derived in the electric AC circuits analysis is extended to acoustics. In [3] the fundamental physical concept of energy trajectory is assimilated to a continuous line network of electric circuits, and the complex intensity vector field is defined by means of three spatial directions: the tangent, the principal normal and the binormal direction at each point of any energy path.

1.2 Definition of the quantities in a general field

1.2.1 The four-dimensional energy-momentum tensor

In the unified space-time approach proposed in [4], similar to the relativistic formulation of electromagnetism, a 4 x 4 acoustic energy-momentum tensor T is introduced:

$$T := [\rho_e \phi^\mu \phi^\nu + g^{\mu\nu} L] g_\mu \otimes g_\nu \in M_4 \otimes M_4 \tag{1.1}$$

and can be represented by the 4 x 4 matrix

$$A = \begin{pmatrix} W & \mathbf{t} \\ \mathbf{t} & \mathbf{T} \end{pmatrix} \tag{1.2}$$

The component T^{00} is the acoustic energy density W, $T^{i0} = T^{0i}$ is the acoustic energy-flux density $\mathbf{j}$/c and $\mathbf{T}$ is the tensor represented by:

$$\mathbf{T} = \rho_e \mathbf{v} \otimes \mathbf{v} - L\mathbf{e} = \rho_e [\mathbf{v} \otimes \mathbf{v} + \frac{1}{2}(p^2/z^2 - \mathbf{v}^2)\mathbf{e}] \tag{1.3}$$

The tensor $\mathbf{T}$ is denoted by [1] with -W and is called wave-stress tensor. One of the properties of it is that the trace is equal to twice the Lagrangian density:

$$Tr(T) := T^\mu_\mu = \rho_e \phi^\mu \phi_\mu + g^\mu_\mu L = 2L \tag{1.4}$$

Furthermore, the divergence of T vanishes identically. If we put $\phi_{\mu\nu} := \partial_\mu \partial_\nu \phi$, we find:

$$\partial_\nu T^{\mu\nu} = \rho_e \partial_\nu [\phi^\mu \phi^\nu + g^{\mu\nu} L] = \rho_e \left[\phi^\mu_\nu \phi^\nu - \frac{1}{2}(\phi^\nu \phi^\mu_\nu + \phi^\mu_\nu \phi^\nu) \right] \equiv 0 \tag{1.5}$$

The component $\mu = 0$ represents the conservation law of acoustic energy and is expressed as:

$$\partial_\nu T^{0\nu} = \partial_0 T^{00} + \partial_1 T^{01} + \partial_2 T^{02} + \partial_3 T^{03} = \frac{1}{c}\left(\frac{\partial W}{\partial t} + \nabla \cdot \mathbf{j} \right) = 0 \tag{1.6}$$

The components μ = i = 1, 2, 3 can be written as:

$$\frac{\partial \mathbf{q}(x,t)}{\partial t} + \nabla \cdot T(x,t) = 0, \qquad \nabla \cdot T := \mathbf{e}_i \partial_j T^{ij} \tag{1.7}$$

Such equation represents the acoustic momentum conservation law, if the vector **-**$\nabla$$\cdot$**T** is seen as a force density.

1.2.2 Acoustic radiation pressure

Starting from equation 1.3, that is the wave momentum flux density, the quantity

$$\mathbf{s} = -\rho_e \left[v_n + \frac{1}{2}\left(\frac{p^2}{z^2} - \mathbf{v}^2\right)\mathbf{n}\right] \tag{1.8}$$

describes the acoustic radiation pressure, that is the density of the radiation force applied on an arbitrary surface having normal **n** within the field itself.

The decomposition of **T** into irreducible parts gives:

$$\begin{aligned} \mathbf{T}^{(0)} &= \frac{1}{2}\rho_e\left(\frac{p^2}{x^2} - \frac{1}{3}\mathbf{v}^2\right)\mathbf{e}, \\ \mathbf{T}^{(1)} &= \mathbf{0}, \\ \mathbf{T}^{(2)} &= \rho_e\left(\mathbf{v}\otimes\mathbf{v} - \frac{1}{3}\mathbf{v}^2\mathbf{e}\right). \end{aligned} \tag{1.9}$$

Having the trace Tr(e) = 3 and Tr($\mathbf{v}\otimes\mathbf{v}$) = $\mathbf{v}^2$, it follows that Tr($\mathbf{T}^{(0)}$)=(1/2)ρ_e(3p^2/z^2-$\mathbf{v}^2$) and Tr($\mathbf{T}^{(2)}$) = 0.

The radiation pressure of $\mathbf{T}^{(0)}$ on the surface element with normal **n**, that is the *isotropic* part, is

$$\mathbf{s}^{(0)} = -\mathbf{T}^{(0)} \cdot \mathbf{n} = \frac{1}{2}\rho_e\left(\frac{1}{3}\mathbf{v}^2 - \frac{p^2}{z^2}\right)\mathbf{n} \tag{1.10}$$

This part of **s** is called isotropic, since it has the direction of **n** and its modulus doesn't depend on **n**. From equation 1.10 it follows

$$\mathbf{s}^{(0)} \cdot \mathbf{n} = \frac{1}{3}K - U = \frac{1}{3}(2L - W) \tag{1.11}$$

It may be observed that the isotropic radiation acts as a compression if $z^2 v^2 < 3p^2$ and as an expansion in the opposite case.

1.2.3 Decomposition of the velocity

The author in [5] explains the decomposition of **v** into a component in phase and a component in quadrature with the pressure p, but only for a monochromatic case. A description of such components for general fields instead can be found in [6]. We can in fact decompose the velocity **v** into the sum of a term $\mathbf{v}_p$ with the same time dependence as p and another $\mathbf{v}_q$, such that $\langle p\mathbf{v}_q\rangle = 0$. So we can write:

$$\mathbf{v}(\mathbf{x},t) = \mathbf{v}_p + \mathbf{v}_q \tag{1.12}$$

with

$$\mathbf{v}_p = \frac{\langle p\mathbf{v}\rangle}{\langle p^2\rangle}p; \qquad \mathbf{v}_q = \frac{\langle p^2\rangle\mathbf{v} - \langle p\mathbf{v}\rangle p}{\langle p^2\rangle} \tag{1.13}$$

The first of the equations 1.13 is the "pressure-in-phase" velocity, and has important spatial and temporal properties. The spatial one regards the direction: $\mathbf{v}_p$ is aligned as the time-stationary averaged sound intensity; as regards the time property the $\mathbf{v}_p$ components reproduce the sametime history of the pressure signal but multiplied by the factor $\langle j\rangle / \langle\, p^2 \,\rangle$. The second equation of 1.13 is the "pressure-in-quadrature" component, which is defined by adding the velocity to the opposite of $\mathbf{v}_p$ in order to have the condition $\langle\, \mathbf{v}_p\ \mathbf{v}_q \,\rangle = 0$. In this way, $\mathbf{v}_p$ and $\mathbf{v}_q$ can be considered as the projections over the directions of the Hilbert vector p and the orthogonal one, of the velocity components v_i (i=1,2,3). Finally, the instantaneous intensity $\mathbf{j}(\mathbf{x},\mathrm{t}) = p\mathbf{v}$, which can be decomposed in $\mathbf{j} = p\mathbf{v}_p + p\ \mathbf{v}_q$. In this last expression we introduced the active $\mathbf{a}{:=}p\mathbf{v}_p$ and the reactive $\mathbf{r}{:=}p\mathbf{v}_q$:

$$\mathbf{a}(x,t) = \frac{\langle p\mathbf{v}\rangle p^2}{\langle p^2\rangle}, \qquad \mathbf{r}(\mathbf{x},t) = \frac{p\mathbf{v}\langle p^2\rangle - \langle p\mathbf{v}\rangle p^2}{\langle p^2\rangle} \tag{1.14}$$

whose averages are $\langle\mathbf{a}\rangle = \langle p\mathbf{v}\rangle$ and $\langle\mathbf{r}\rangle = 0$.

It's demonstrated in [3] that

$$\langle p\mathbf{v}_p\rangle = \left\langle p\frac{p\mathbf{v}}{p^2}p\right\rangle = \frac{\langle p^2\rangle}{p^2}\langle p\mathbf{v}\rangle = \langle p\mathbf{v}\rangle, \tag{1.15}$$

$$\langle p\mathbf{v}_q\rangle = \left\langle p\frac{\langle p^2\rangle\mathbf{v} - \langle p\mathbf{v}\rangle p}{p^2}\right\rangle = \left\langle\frac{\langle p^2\rangle\langle p\mathbf{v}\rangle p^2}{p^2}\right\rangle = \frac{\langle p^2\rangle\langle p\mathbf{v}\rangle - \langle p\mathbf{v}\rangle\langle p^2\rangle}{\langle p^2\rangle} = 0 \tag{1.16}$$

so we can say that the following equalities are proved:

$$\langle p\mathbf{v}_p\rangle \equiv \langle p\mathbf{v}\rangle; \qquad \langle p\mathbf{v}_q\rangle \equiv 0. \tag{1.17}$$

1.2.4 The acoustic power factor

We will see in the plots of section 1.4 that the intensity I presents a bounding condition. In fact given the equations in the previous section, we can express it as $I^2 = \langle p^2 \rangle \langle \mathbf{v}_p^2 \rangle$. Considering that $\langle \mathbf{v}_p \mathbf{v}_q \rangle = 0$, we obtain

$$I^2 = \langle p^2 \rangle \left[\langle \mathbf{v}^2 \rangle - \langle \mathbf{v}_q^2 \rangle \right], \tag{1.18}$$

which shows that $0 \leq I^2 \leq \langle p^2 \rangle \langle \mathbf{v}^2 \rangle$ or

$$0 \leq I \leq \sqrt{\langle p^2 \rangle \langle \mathbf{v}^2 \rangle} \equiv p_{rms} v_{rms} \tag{1.19}$$

This equation allows to understand the physical meaning of the power factor $\Delta\phi$. We define the reactive intensity as:

$$Q = \sqrt{\langle p^2 \rangle \langle \mathbf{v}_q^2 \rangle} \tag{1.20}$$

so we have:

$$I^2 + Q^2 = \langle p^2 \rangle \langle \mathbf{v}^2 \rangle \tag{1.21}$$

from which the power factor for general fields can be expressed as

$$cos\Delta\phi = \frac{I}{\sqrt{I^2 + Q^2}} \equiv \xi, \qquad -\frac{\pi}{2} \leq \Delta\phi \leq \frac{\pi}{2} \tag{1.22}$$

The power factor is then the ratio of the active intensity at every field point to the time-averaged total intensity ξ. On the other hand the reactive intensity is expressed as:

$$\mathbf{I}(x) = (p_{rms} v_{rms} cos\Delta\phi)\hat{t} \tag{1.23}$$

We can insert the term Q in a complex quantity $\hat{S}$ called complex velocity and expressed as $\hat{S} = I + iQ$, that is a phase vector of magnitude $\sqrt{I^2 + Q^2}$ and angle $\Delta\phi = arccos\xi$.

1.2.5 Sound energy conductance and susceptance

To complete the acousto-electro-mechanic analogy, we introduce the concept of energy susceptibility, and define the reactivity index μ as:

$$\mu \equiv Q/cW \tag{1.24}$$

which is the imaginary part of the sound energy admittance $\overline{\sigma}$

$$\overline{\sigma} \equiv \eta + i\mu \tag{1.25}$$

The magnitude of the $\rho_0 c$-normalized sound energy admittance consists in the energy partition index $\sigma = 2W_k W_p/(W_k + W_p)$, i.e., the ratio of the geometric to arithmetic mean of the time-averaged kinetic and potential densities W_k and W_p.

Finally, we introduce the energy resistance R and energy reactance X, that can be obtained as the real and imaginary parts of the $\rho_0 c$-normalised energy impedance $\overline{\sigma}^{-1}$:

$$\overline{\sigma}^{-1} = \frac{1}{\eta + i\mu} = \frac{\eta}{\sigma^2} - i\frac{\mu}{\sigma^2} \equiv R + iX \tag{1.26}$$

1.3 Monochromatic case

Monochromatic plane-waves reflection is the simplest case of wave reflection phenomena: the incident and the reflected waves have the same direction but propagate in opposite ways. In these conditions the velocity potential ϕ(x,t) can be expressed as:

$$\phi(x,t) = Ac[e^{i(kx-\omega t)} + Re^{i(kx+\omega t+\vartheta)}] \tag{1.27}$$

where A is the displacement amplitude, $k = \omega/c$ is the wave number, R is the scaling factor of the reflected wave and θ is the phase shift between the incident and the reflected wave. The solutions of pressure and velocity are derived by differentiating $\phi(x,t)$ and setting $z_0 = \rho_0 c$ are:

$$p(x,t) = -\rho\frac{\partial\phi}{\partial t} = \Re(Az_0(i\omega)[e^{i(kx-\omega t)} - Re^{i(kx+\omega t+\vartheta)}]), \tag{1.28}$$

$$v(x,t) = \nabla\phi = \Re(A(i\omega)[e^{i(kx-\omega t)} + Re^{i(kx+\omega t+\vartheta)}]) \tag{1.29}$$

where $z_0 = \rho_0 c$ is the characteristic impedance of air. It is known tat the combination of the equations 1.28 and 1.29 contributes to the energy transport inside the acoustic field described by the potential 1.27.

In order to calculate the energetic quantities, it's necessary to define the averaging operation $\langle\cdot\rangle \equiv (2T)^{-1}\int_{-T}^{T} \cdot dt$ over a complete cycle $T = 2\pi\omega^{-1}$ where ω is the circular frequency of the monochromatic wave. By applying the stationary average the analytic expressions of the energetic quantities such as the active (or radiative) intensity A and the mean densities of potential w_u and kinetic w_k energy:

$$A = \langle pv \rangle = \frac{1}{2} z_0 (a\omega)^2 (1 - R^2) \quad [W/m^2] \tag{1.30}$$

$$W_u = \frac{1}{2\rho_0 c^2} \langle p^2 \rangle = \frac{1}{2} \rho_0 (a\omega)^2 \left[\frac{1+R^2}{2} - Rcos(kx+\theta) \right] \quad [J/m^3] \tag{1.31}$$

$$W_k = \frac{1}{2} \rho_0 \langle v^2 \rangle = \frac{1}{2} \rho_0 (a\omega)^2 \left[\frac{1+R^2}{2} + Rcos(kx+\theta) \right] \quad [J/m^3] \tag{1.32}$$

From equations 1.31 and 1.32 we can derive the expression of total energy:

$$W_{tot} = W_u + W_k = \frac{1}{2} \rho_0 (a\omega)^2 (1 + R^2) \quad [J/m^3] \tag{1.33}$$

From Eq. 1.30,1.31 and 1.32 we can derive-by normalizing it with respect to c- the conductance η, which is the velocity of the energy inside the wave field, and the acoustic power factor ξ:

$$\eta = \frac{A}{c(W_u + W_k)} = \frac{\frac{1}{2}(A\omega)^2 z_0 (1-R^2)}{\frac{c}{2}(\frac{\langle p^2 \rangle}{\rho_0 c^2} + \rho_0 \langle u^2 \rangle)} = \frac{\frac{1}{2}(A\omega)^2 z_0 (1-R^2)}{\frac{c}{2}\frac{1}{2}(A\omega)^2 \rho_0 (1+R^2)} = \frac{1-R^2}{1+R^2} \tag{1.34}$$

$$\xi = \frac{A}{2c\sqrt{W_u W_k}} = \frac{1-R^2}{\sqrt{(1+R^2)^2 - 4R^2 cos^2(2kx+\theta)}} \tag{1.35}$$

$$\Delta\varphi = cos^{-1}(\xi) \tag{1.36}$$

where $\Delta\varphi$ is the phase shift between the pressure and the velocity wave.

The power factor ξ is then the ratio of the active intensity at every field point to the time-averaged total intensity at the same point. The reflection coefficient can be expressed in terms of normalized conductance as:

$$R = \sqrt{\frac{1-\eta}{1+\eta}} \tag{1.37}$$

We can conclude that starting from pressure and velocity measurements (acoustic observables) we can derive some quantities of the energetic acoustics. Starting from their expressions in terms of R and θ we can realise the simulation of the sound field represented by the potential. This method clearly allows a direct check of the simulated model with experimental data obtained with p-v intensimetry and gives at the same time a key to the models of a quasi stationary wave fields directly based on the calculation of impedance.

In the next section, the just described quantities will be illustrated through a synoptic visualization [7].

1.4 Synoptic visualization of the simulation results

The simulation has been realized using an algorithm written in Maple®, in which once defined the principal parameters, the required energetic quantities are derived. The initial parameters are: f= 429 Hz, c= 343.4 m/s, ρ_0= 1.204 kg/m^3, L_p= 95 dB. The pressure level, here used to calculate the amplitude of kinetic potential using the expression $a = p_{RMS} / \omega\rho_0 c$ with $p_{RMS} = p_0 \cdot 10^{L_p/20}$, arises from experimental data. With this premises a value of a= $1.0046 \cdot 10^{-6}$ m is derived. The results of the simulations are resumed in figures from 1.1 to 1.10. The horizontal axes indicate the ratio x/λ, where λ is the wavelength and x is the length.

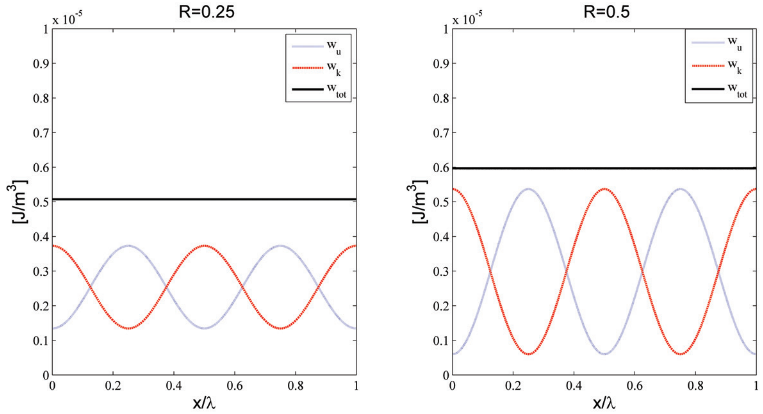

Fig. 1.1 Trend of potential, kinetic and total energy with R=0.25 (left) and R=0.5 (right), for θ=0.

The plots in figure 1.1 and 1.2 show the behaviour of the mean energy densities, w_u, w_k and w_{tot} for increasing R from 0.25 to 1 (stationary wave), with $\theta = 0$. The increase of the amplitude of the reflected wave emphasizes the maxima of the potential and of the kinetic energy, and therefore enlarges the total energy density until the maximum value of $W_{tot} = a^2\omega^2\rho_0$. Figures 1.3a and 1.3b illustrate the phase change of the potential and of kinetic energy by varying the phase θ from 0 to 1, while in figure 1.4 the Lagrangian L for different values of R is simulated. The oscillation of this quantity is maximum for a stationary

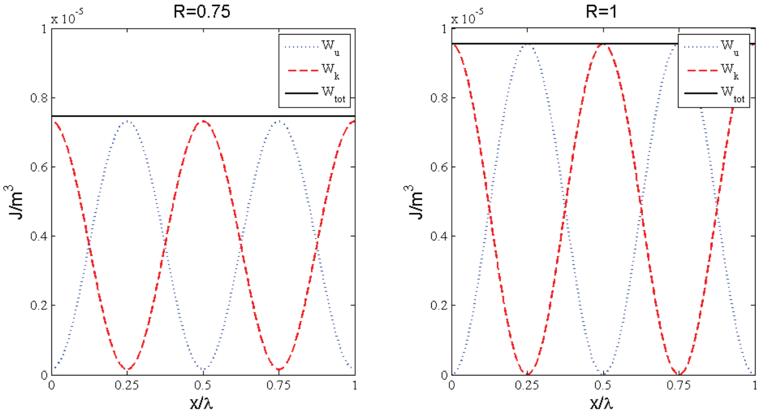

Fig. 1.2 Trend of potential, kinetic and total energy with R=0.75 (left) and R=1 (right), for θ=0.

wave, while in the opposite case of progressive wave the kinetic energy equals the potential energy and the Lagrangian is null at each point.

In Fig. 1.6 are shown, on the left, the values of the active intensity for different values of R (in [W/m^2]), while on the right the relative values of the velocity of acoustic energy η in units of c are displayed. The decreasing trend of the intensity indicates how the flux of the absorbed energy (and therefore irradiated by the field) is maximum when the pressure-velocity wave that transports the energy is totally progressive (R=0). This aspect is more easily explained by the modulus of the energy velocity that-being normalised with c- is 1 when the energy transport has the same velocity of the propagation of acoustic waves.

Figures 1.6 and 1.7 show respectively the behaviour of the power factor ξ, expressed in 1.35 and of the phase shift $\Delta\ \varphi$ of the p-v wave when the amplitude of the reflected wave R (top) and the phase difference between the incident and the reflected wave are varied. It's clear how, by increasing R, the power factor of the wave diminishes: nevertheless it's extremely significant the fact that for all the values 0<R<1 the power factor reaches the maximum with a period of $\lambda/4$. The effect of varying θ is a simply spatial shift of the highest power points (where ξ=1).

In Fig. 1.8 and 1.9 are shown other energetic quantities with varying R: in the first one we can see the behaviour of pv_p and pv_q, where v_p and v_q derive from the decomposition of the air particle velocity $\mathbf{v}$:

Figure 1.10 represents the isotropic component of the acoustic radiation pressure for different values of R, which is described by the expression 1.11. Different values of the radiation pressure correspond to an energetic compression state, so it's evident from the plot that the energy transported by the progressive plane wave is always compressed. In particular at values or $R \leq 0.27$ the pressure remains negative, oscillating around the constant value

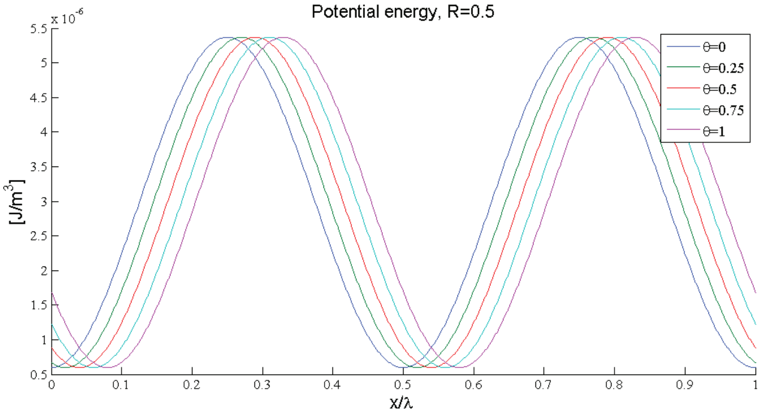

(a) Potential energy.

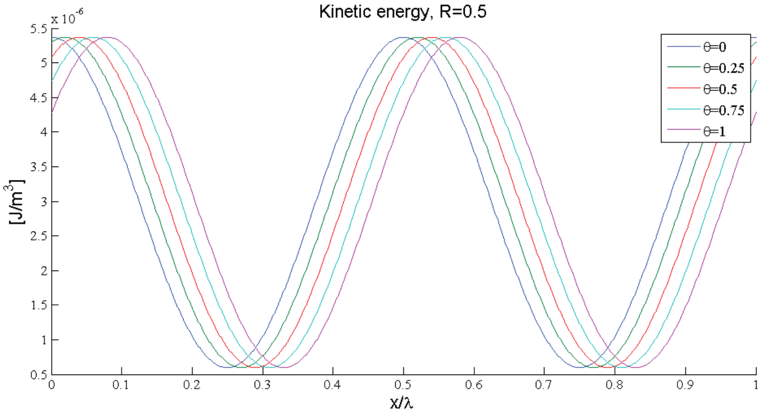

(b) Kinetic energy.

Fig. 1.3 Trend of potential (top) and kinetic (bottom) energy.

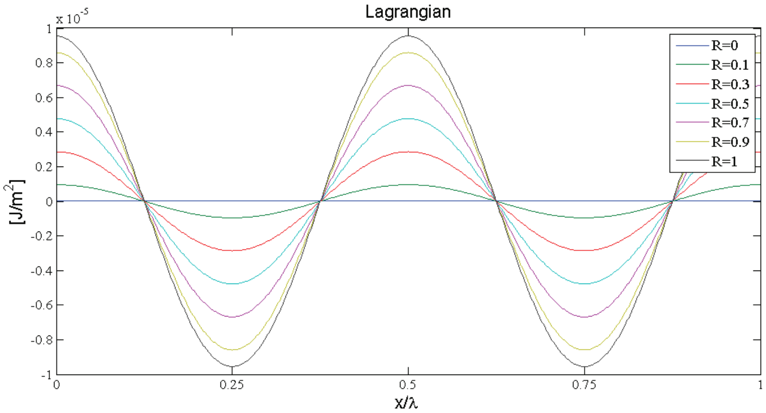

Fig. 1.4 Lagrangian for varying R.

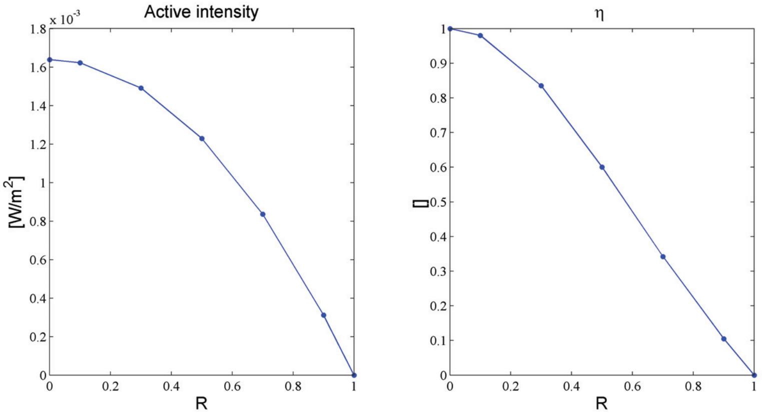

Fig. 1.5 Trend of active intensity A and of η varying R.

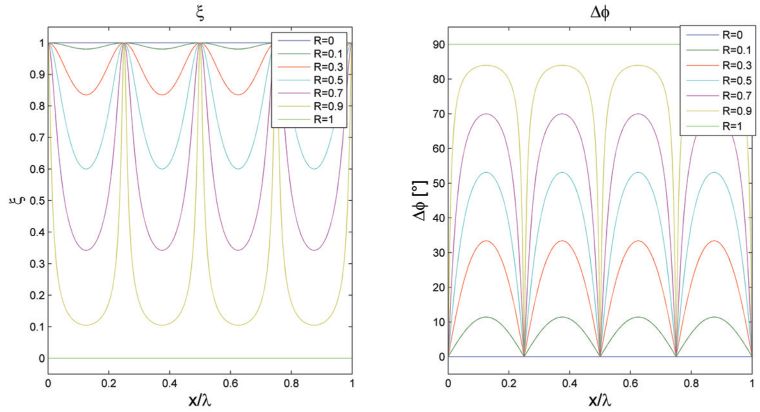

Fig. 1.6 Trend of ξ and of $\Delta\varphi$ with varying R, θ=0.

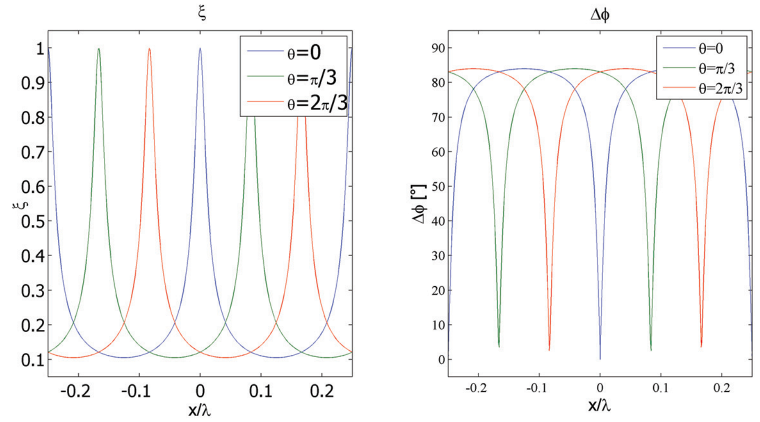

Fig. 1.7 Trend of ξ and of $\Delta\varphi$ with varying θ, R=0.9.

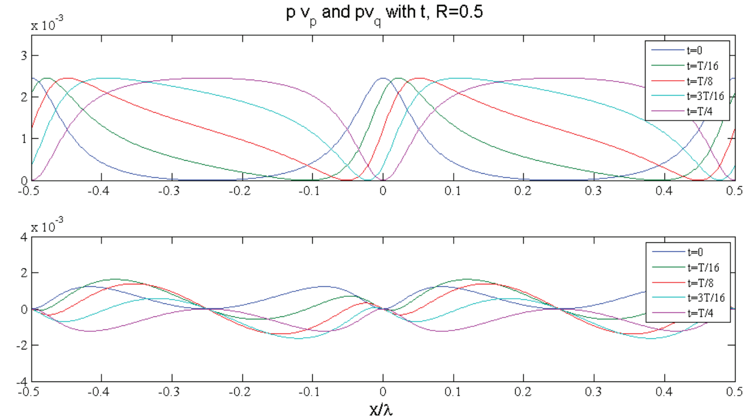

Fig. 1.8 Trend of pv$_p$ and pv$_q$ with R.

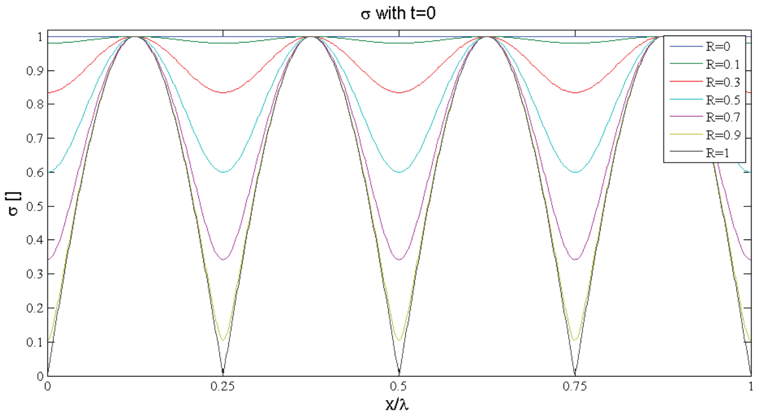

Fig. 1.9 Trend of σ for different R.

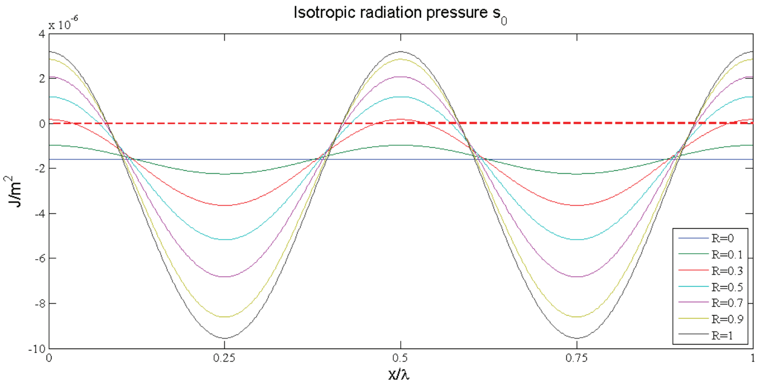

Fig. 1.10 Isotropic radiation pressure for different R.

given by the plane wave (R=0). During the simulations we have verified, as expected, that the radiation pressure of a progressive plane wave is proportional to the value of the pressure level L_p.

Chapter 2

Interlaboratory comparison of the calibration of a commercial pressure-velocity probe

In this chapter two methods of calibration are applied to the same probe and the results are compared. The first one is the piston in a sphere method and is used at the Microflown laboratory in Arnhem, while the second one is the plane wave progressive field and is adopted at Ferrara, inside the Larix laboratory. A short digression in the first section introduces the main techniques to calculate the impulse response of a system.

2.1 Identification of linear system: a qualitative review

There are several methods to caculate the impulse response of a system: a complete review can be found in [8] or in [9]. The study of the acoustic phenomena can be described considering the process as a dynamical system, dominated by a relationship of cause and effect [10]. If the process depends only on a single variable, such as time, we can define an operator that transforms an input function *s(t)* in an output funciton *f(t)*. If the system is linear (in which a combination of input signals produces the same combination of output signals) and time-invariant, the impulse response can be described by the relation:

$$f(t) = \int_{-\infty}^{+\infty} s(\tau)h(t-\tau)d\tau \tag{2.1}$$

where *h(t)* is the response of the linear system and is called *impulse response*. In the frequency domain the convolution can be expressed as:

$$F(\omega) = S(\omega) \cdot H(\omega) \tag{2.2}$$

with H the transfer function of the system. The sine sweep method has been developed only in the second part of the last century, after quite a number of different ways to measure the transfer function and its relative impulse response. Every method is based on an excitation signal (stimulus) characterised by the frequencies of interest to feed the device under test [9]. Then the response of the device is compared with the original signal. The different methods are listed hereinafter:

1. **The level recorder:** the logarithmic sweep generated by an analogue generator is filtered through a low-pass filter. The voltage becomes the input to a differential amplifier whose other input is linked to a writing pen after passing through a potentiometer. This is one of the oldest methods and doesn't give information on the phase.

2. **Time delay spectrometry (TDS):** this method is particularly used for the measurement of loudspeakers, but is also applicable to room acoustics. The analyser consists of a generator which produces a swept sine and a cosine. The firts signal goes to the loudspeaker and its response is multiplied by both the input signals. The multiplier outputs are filtered by a low-pass.

   The reflections are controlled by the use of a linear sweep instead of a logarithmic one, but there are various disadvantages, such as SNR at low frequencies, the necessity to have a very long sweep because of the poor spectral energy distribution, and the presence of ripples, especially at low frequencies.

3. **Dual channel FFT analysis:** such method captures both the input and the output signal of the device under test, and the signal is cut in segments which are windowed and transformed to the spectral domain via FFT. The two resulting spectra are then averaged through three processes, two for the autospectra and one for the cross-spectrum.

   The advantage of such method is the unique possibility to measure sound systems unobtrusively during the performance.

4. **Stepped sine:** it consists in exciting the DUT step by step with pure tones of increasing frequency. The response can be analysed by filtering and rectifying the fundamental, or by performinf an FFT and alalysing the fundamental from the spectrum.

5. **Impulses:** this method uses impulse as excitation signal. The impulse's response by the DUTis captured by a microphone, amplified and digitized by an AD converter, and to increase the SNR, the pulse can be repeated periodically thus producing a periodic IR (PIR) [11].

   The averaging guarantees a reduction of uncorrelated noise, but this method requires a low noise floor and doesn't allow identifying distortion. On the contrary, it has the advantage of being a very simple procedure which doesn't require sophisticated signal processing.

6. **Maximum length sequences (MLS):** this is the most popular method after the sine sweep. It has got a discrete nature: the excitation signal is made up of a pseudo-casual binary sequence with values 1 and 0, of length of L=2^m - 1, transformed in signals of amplitude ± V_0. In this case the excitation signal corresponds to white noise, in a way that the mutual correlation between input and output directly furnishes the system impulse response.

   The advantages in such method are the handiness of a deterministic creation of arbitrarily long sequences, the possibility of using very rapid cross-correlation algorithms (such as the well-known fast Hadamard transform- FHT), and finally good results in terms of signal to noise ratio. Despite the great success of this method, it presents some drawbacks, such as the vulnerability to distortion and time variance.

7. **Periodic signals:** this method is more efficient than the MLS, because in this case the excitation signal has 2^N samples instead of 2^N-1, and the DUT response can be transformed directly to the spectral domain, omitting the FHT. Such a method is more powerful and flexible, allowing the use of arbitrary signals of 2^N, but, performing two FFTs instead of one single FHT, it consumes more processing time. Here the spectrum needs to be calculated only once and can be used in all subsequent measurements. This makes a second channel no more necessary, or allows the analysis of two inputs simultaneously.

8. **Non periodic sweeps:** this methiod is based on the fact that the spectrum of non-repeated single sweep is almost identical to that of its periodic repetition, so it's no more necessary to repeat the signal two times to establish the final spectrum. In this way the DUT's response can be measured and elaborated immediately, so reducing the duration of the measurement. Moreover, the harmonic distortion components can be entirely isolated from the acquired IR.

9. **Sine sweep:** This is the most important case of FT technique of measuring the impulse response. The sine sweep is a sinusoidal signal of constant amplitude and time-varying frequency, and can be described by the expression s(T) = sin [f(t)]. The most used kind of sweeps are the linear and the logarithmic one [12]. In both cases the frequency is an increasing function in time. For acoustic measurements, the used frequencies interval is included in the audible range, and in our case we used the band from ω_1=20 Hz to ω_2=20 KHz, with a T of few seconds. A linear sweep is defined by:

$$\frac{df(t)}{dt} = \omega_1 + \frac{\omega_2 - \omega_1}{T} t \tag{2.3}$$

which gives

$$f(t) = \omega_1 t + \frac{\omega_2 - \omega_1}{2T} t^2 \tag{2.4}$$

and

$$s(t) = sin\left[\omega_1 t + \frac{\omega_2 - \omega_1}{2T} t^2\right] \tag{2.5}$$

The linear sweep is also called "time stretched pulse" ([13], [14]) because of the constantly spread energy in each frequency band: i.e. the energy of the interval 100 Hz-200 Hz is the same as in 1000 Hz-1100 Hz. So we can say that:

$$\int\limits_{t_1}^{t_1+\Delta t} s^2(\tau)d\tau = \int\limits_{t_2}^{t_2+\Delta t} s^2(\tau)d\tau \tag{2.6}$$

or, similarly,

$$\int\limits_{\omega(t_1)}^{\omega(t_1+\Delta t} S^2(\omega)d\omega = \int\limits_{\omega(t_2)}^{\omega(t_2+\Delta t} S^2(\omega)d\omega \tag{2.7}$$

with S(ω) the Fourier transform of s(ω), and, being the sweep linear, we have $\omega(t_1 + \Delta t) - \omega(t_1) = \omega(t_2 + \Delta t) - \omega(t_2)$. The other type of sweep is the logarithmic one, and is described in [8] as:

$$x(t) = sin\left[K\left(e^{t/L} - 1\right)\right] \tag{2.8}$$

Such signal has a starting frequency called ω_1 and an ending frequency ω_2, and a duration of T seconds; the conditions are:

$$\frac{d}{dt}\left[K\left(e^{t/L} - 1\right)\right]\Bigg|_{t=0} = \omega_1 \qquad \frac{d}{dt}\left[K\left(e^{t/L} - 1\right)\right]\Bigg|_{t=T} = \omega_2 \tag{2.9}$$

After solving the previous, we have:

$$K = \frac{T\omega_1}{log(\omega_2/\omega_1)} \qquad\qquad L = \frac{T}{log(\omega_2/\omega_1)} \tag{2.10}$$

therefore the final equation of the logarithmic sweep is:

$$s(t) = sin\left[\frac{T\omega_1}{log(\omega_2/\omega_1)}\left(e^{\frac{t}{T}log(\frac{\omega_2}{\omega_1})} - 1\right)\right] \tag{2.11}$$

In this case the energy is constant for bands of frequency of constant logarithmic length, that is:

$$\int_{t_1}^{kt_1} s^2(\tau)d\tau = \int_{t_2}^{kt_2} s^2(\tau)d\tau \tag{2.12}$$

and in the frequency domain

$$\int_{\omega(t_1)}^{\omega(kt_1)} S^2(\omega)d\omega = \int_{\omega(t_2)}^{\omega(kt_2} S^2(\omega)d\omega \tag{2.13}$$

Finally, for the logarithmic sweep, we have $\omega(k\cdot t_1)/\omega(t_1) = \omega\ (k\cdot t\ _2)\ /\omega(t_2)$ The advantage of such method is a higher SNR compared to the other ones. In fact a background noise is always present in the measurement systems in the shape of environmental background noise, or thermal, electronic noise. So the response is always affected by casual biases, that are generally distributed throughout the frequencies, especially in correspondence of the audible range. Even if it's impossible to completely remove the background noise from a measure, it has been observed how the high value of SNR within the sine sweep method, guarantees optimal results just with one single measure. Moreover, the longer is the sweep duration, the higher is the signal-to-noise ratio, therefore if the background noise during a set of measures is high, it's sufficient to increase the sweep duration.

2.2 Calibration at the Microflown Lab in Arnhem: Piston in a sphere method

A good review of the methods of calibration used at Microflown in Arnhem can be found in [15]. First of all, a clarification on the measure units: the sensitivity of pressure microphones is usually expressed in mV/Pa, while for the velocity sensors we measure the output voltage relative to the velocity of the air particles, and then we define the sensitivity in mV/(m/s). Since 1 Pa corresponds to a level of 94 dB_{SPL}, and 1m/s to 146 dB_{SPL}, we deduce that the two values are difficult to compare. Therefore a new unit has been defined: the Pa* is the velocity that corresponds to a 1 Pa of pressure in a plane wave, that is 1 Pa*=1Pa/ρc=2.4 mm/s. The sensitivity of the velocity sensor will be expressed in mV/Pa*. This is due to the fact that the calibration methods are based on the normalised specific acoustic impedance, that is the real impedance divided by ρc, and the real value of the impedance is not known.

Among the various methods of calibration of a pressure-velocity probe, the Microflown draws on two standard methods:

- a piston in a sphere method, in which the probe is put outside a spherical source, and it's calibrated in a free field through two steps for two different range of frequency;
- the short standing wave tube method, which is efficient only at low frequencies, in a 20 Hz-3.5 KHz bandwidth.

During my visit to Microflown I personally calibrated a match size p-v probe with the piston in a sphere method, producing a calibration report that will be illustrated later. Jacobsen demonstrated in [16] that it's possible to calibrate a p-v sensor in free field conditions at high frequencies by using the a-priori known impedance at a certain distance from a spherical speaker, but such method is not feasible at lower frequencies because the velocity is no longer derivable from the pressure and the impedance with good results. The authors in [17] extended the method to low frequencies bandwidth by directly measure the acoustic pressure inside the spherical source. At low frequencies the sound pressure inside the sphere is proportional to the movement of the loudspeaker membrane, so by measuring the movement, we the particle velocity in front of the loudspeaker can be derived.

The final step of the procedure consists in combining the low and high frequencies measures so obtaining a full bandwidth calibration procedure whose results can be used in free field conditions.

2.2.1 High frequency set up

The image in figure 2.1 shows the setup for the high frequency calibration: the Microflown probe and the reference microphone with a known sensitivity (a G.R.A.S. 40AC with G.R.A.S. 26AF preamplifier) are positioned at a certain distance in front of the speaker, nearly at the same position, as can be seen in the scheme 2.2. In this configuration the pressure microphone can be calibrated in a range between 20 Hz and 10 KHz. We must say that

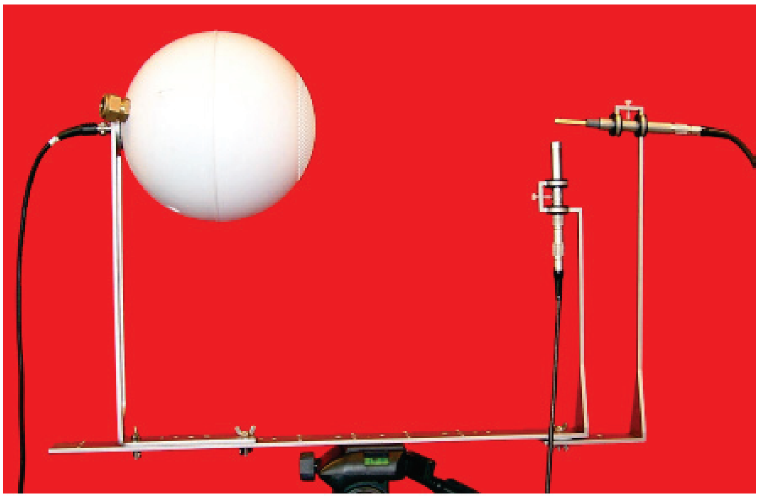

Fig. 2.1 Piston in a sphere set up for the calibration at high frequencies.

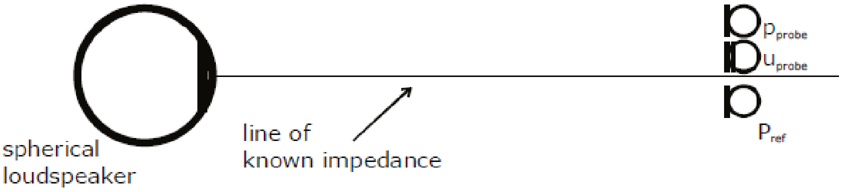

Fig. 2.2 The piston in a sphere set up.

the possible presence of background noise doesn't invalidate the process, because both the microphones are omnidirectional and therefore the input energy remains the same. In order to calibrate the velocity sensor, a monopole as signal source is necessary, in order to have an omnidirectional source in a large bandwidth. The source consists of a loudspeaker put inside a spherical plastic sphere, which can be modeled as a sphere of radius a and an internal piston of radius b. The impedance on the axis of the piston can be derived using the expression:

$$Z_{sphere}(r) = -i\rho c \frac{\sum_{m=0}^{\infty}(P_{m-1}(cos\alpha))\frac{h_m(kr)}{h'_m(ka)}}{\sum_{m=0}^{\infty}(P_{m-1}(cos\alpha))\frac{h'_m(kr)}{h'_m(ka)}} \tag{2.14}$$

where r is the distance from the centre of the sphere, *a=arcsin(b/a)*, a is the radius of the sphere, b is the radius of the loudspeaker and P_m is the Legendre function of the order m, h_m is the spherical Hankel function of the second kind and order m, h'_m is its derivative, k is the wave number. The term ρc is the acoustic specific impedance of air, which depends on external conditions like temperature, atmospheric pressure and relative humidity. The last values are integrated in the model calculated during the calibration.

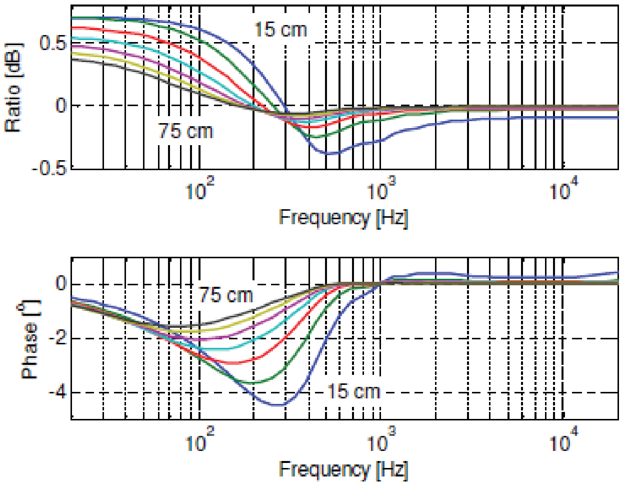

Fig. 2.3 The ratio between the impedance of a piston in a sphere and of a monopole [15]. The different curves indicates distances from the front of the sphere with values from 15 to 75 cm.

The impedance in 2.14 is similar to the acoustic impedance of a monopole source, given by:

$$Z(r) = \rho c \frac{ikr}{1+ikr} \tag{2.15}$$

The ratio of the normalised impedance of the piston in a sphere (equation 2.14) to the impedance of a monopole (equation 2.15) is shown in figure 2.3 for different distances between the microphone and the loudspeaker. It can be seen that the piston in a sphere model becomes more similar to a monopole source model at higher frequencies, while for the lower ones it will be necessary an additional step, that will be described in the next section. It has been demonstrated that smaller spheres better follow the monopole model, besides being more easy to transport, so the calibration has been conducted using a 9 cm sphere (figure 2.4). Such setup has been modified so the probe to calibrate can easily be shifted from the high frequency calibration position (far from the loudspeaker) to the low frequency calibration position (close to the sphere).

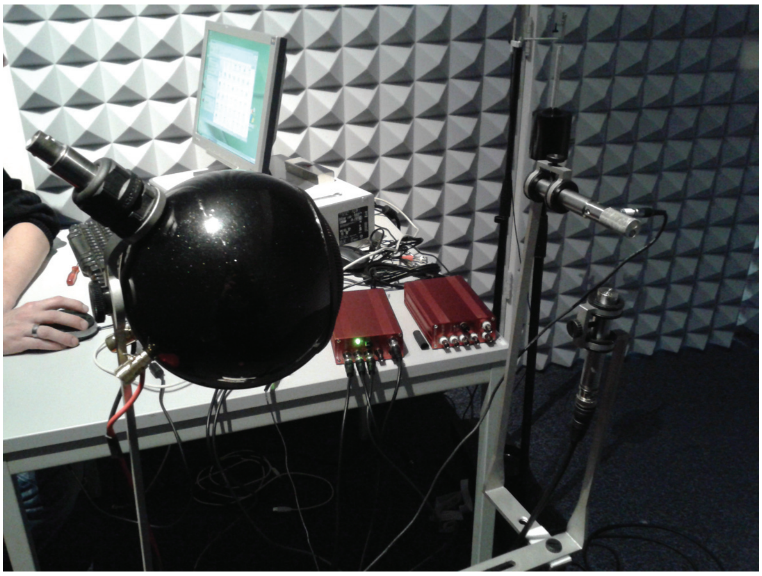

Fig. 2.4 The setup used for the calibration during my visit at Microflown.

2.2.2 Low frequency setup

At low frequencies the calibration described in the previous section presents some problems. In this bandwidth the background noise has higher pressure levels than the noise generated by the source itself, in particular below 50 Hz. The ratio between the particle velocity and the pressure increases in the near field, and it's significant for low frequencies when the probe is in front of the loudspeaker. On the contrary for the background noise, with the probe in the far field, such ratio has almost the same values at all frequencies.

In an anechoic room, with no background noise, the previous method of calibration is feasible down to 50 Hz, but in a common room, where the background noise is higher, the far

Fig. 2.5 The setup used for the calibration at low frequencies.

field method starts working from 100 Hz to 200 Hz. Therefore when the background noise is dominant, equation 2.14 is no longer usable, and a new approach must be followed.

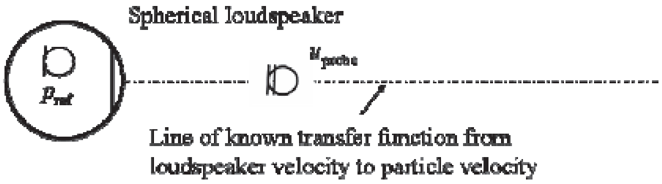

Fig. 2.6 The scheme for the low frequencies calibration, with the reference microphone inside the sphere.

Figures 2.5 and 2.6 show the setup for the low frequencies calibration: the reference microphone is directly put inside the sphere through a hole, while the p-v probe under test is positioned in front of the loudspeaker. The reference microphone directly measures the pressure variations inside the sphere, and the relation between the internal pressure and the particle velocity in front of the sphere is used for the calibration.

In fact the pressure inside the sphere is high enough to be measured at low frequencies and the relation between the pressure and the velocity outside the speaker is linear. Moreover, the particle velocity just in front of the speaker is similar to the velocity of the membrane, thanks to the continuity condition.

So the relation between the pressure inside the sphere and the velocity outside the sphere is given by:

$$u_{piston} = -\frac{i\omega V_0}{\gamma A_0 p_0} p_{ref} \tag{2.16}$$

with ω the angular frequency, V_0 the interior volume of the sphere, A_0 is the surface area of the moving piston, p_0 the ambient pressure and γ the ratio of specific heats. We assume that the compression and rarefaction of the air inside the sphere is an adiabatic process.

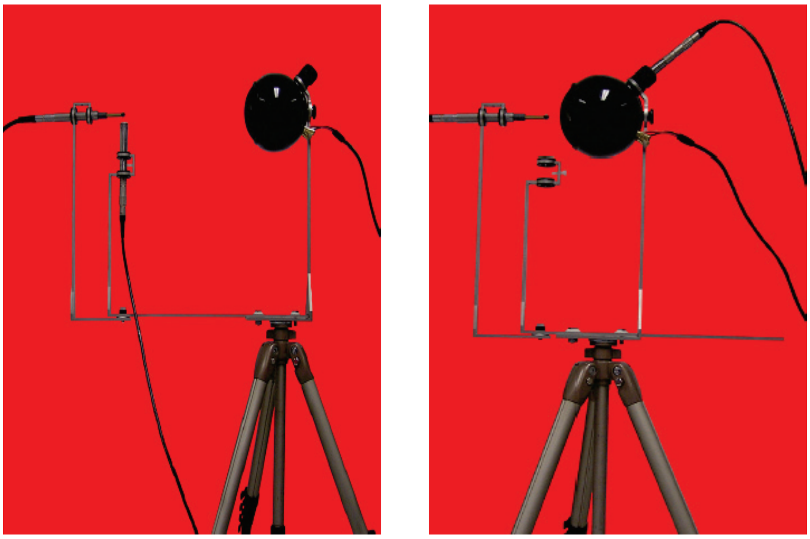

Fig. 2.7 The calibration set up: on the left the far field, on the right the near field.

Figure 2.7 shows the two set up for the calibration in the far (left) and in the near (right) field. Being known the acoustic field around the sphere, it's possible to derive the particle velocity at a certain distance from the sphere from the velocity in front of the piston. Such quantity is then related to the pressure inside the sphere.

The relation between the particle velocity in front of the speaker u_n and the velocity at a certain distance r from the centre of the sphere is given by:

$$u(r) = -\frac{u_n}{2} \sum_{m=0}^{\infty} (P_{m-1}(cos\alpha) - P_{m+1}(cos\alpha)) \frac{h'_m(kr)}{h'_m(ka)} \tag{2.17}$$

where r is the distance from the speaker membrane and the other parameters have already been described for the equation 2.14. The relation between the particle velocity at position r and the pressure inside the sphere is given by combining eq.2.16 and 2.17:

$$\frac{u(r)}{p_{ref}} = \frac{j\omega V_0}{2\gamma A_0 p_0} \cdot \sum_{m=0}^{\infty} (P_{m-1}(cos\alpha) - P_{m+1}(cos\alpha)) \frac{h'_m(kr)}{h'_m(ka)} \tag{2.18}$$

2.2.3 Combination of the two steps

We have seen how Microflown uses a two steps method to calibrate its p-v probe, one for high frequencies (far field), and another for low frequencies (near field, with the microphone inside the speaker). The final step is to determine a full bandwidth sensitivity by combining the results of the previous phases. There are similar results with the two methods at central frequencies, around 300 Hz, so the two curves will be connected within this bandwidth.

The first step consists in measuring the transfer functions between the sensors in far field configuration, with the reference microphone and the probe under test nearly in the same position along the axis in front of the speaker, at a known distance. The sensitivity S$_p$ of the pressure sensor is calculated from the reference microphone output (in Volts) and the output of the pressure sensor (in Volts):

$$S_p\left[\frac{mV}{Pa}\right]=\frac{p}{p_{ref}}\left[\frac{V}{V}\right]\cdot S_{ref}\left[\frac{mV}{Pa}\right] \tag{2.19}$$

where S_{ref} is the sensitivity of the reference microphone, that is known from the data sheet and is considered independent of frequency.

The sensitivity of the velocity sensor is derived from the model of a piston in a sphere through

$$S_u\left[\frac{mV}{Pa*}\right]=\frac{u}{p_{ref}}\left[\frac{V}{V}\right]\cdot Z_{sphere}\left[\frac{Pa}{Pa*}\right]\cdot S_{ref}\left[\frac{mV}{Pa}\right] \tag{2.20}$$

While the sensitivity found for the pressure sensor is working in the full bandwidth, it's necessary to calculate the sensitivity of the velocity sensor for low frequencies, by inserting the reference microphone directly inside the spherical loudspeaker and the probe under test in front of the membrane. White noise is emitted from the source and the transfer functions are measured; the particle velocity sensitivity is then calculated substituting in 2.19 the term Z_{sphere}.

$$S_u\left[\frac{mV}{Pa*}\right]=\frac{u}{P_{ref}}\left[\frac{V}{V}\right]\cdot\frac{u_n}{u}\left[\frac{Pa*}{Pa*}\right]\cdot\frac{p_{ref}}{u_n}\left[\frac{Pa}{Pa*}\right]\cdot S_{ref}\left[\frac{mV}{Pa}\right]= \tag{2.21}$$

$$=\frac{u}{p_{ref}}\left[\frac{V}{V}\right]\cdot\frac{p_{ref}}{u(r)}\left[\frac{Pa}{Pa*}\right]\cdot S_{ref}\left[\frac{mV}{Pa}\right] \tag{2.22}$$

Finally, the sensitivity curves are smoothed through a moving average filter, and the low frequencies one is vertically shifted until the two curves coincide around 300 Hz. This is the final sensitivity curve that will be used for the calibration.

2.2.4 The Microflown model

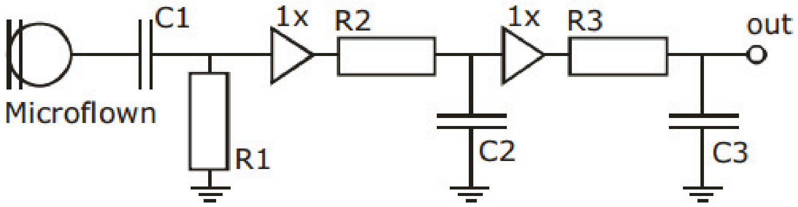

Fig. 2.8 Electrical model of the behaviour of a Microflown probe [15].

Although as it has been said before, the sensitivity is independent from the frequency for pressure, this is not true for velocity sensors. That's why Microflown has developed a model which includes the effect of the frequency, by introducing the parameters called *corner frequencies*. Such parameters are strictly connected to the electrical model of the probes (Fig. 2.8), which includes three filters: R_1C_1 is a high pass filter with a corner frequency around 100 Hz, R_2C_2 depends on the volumetric heat capacity [18], while R_3C_3 marks the thermal mass of the wires in the velocimeter. The last two are low pass filters, with corner frequencies respectively in the order of 1 KHz and of 10 KHz.

The model that describes the sensitivity behaviour of the pressure sensor is:

$$S_p[mV/Pa] = S_p@1KHz \frac{\sqrt{1+\left(\frac{f}{f_{c3p}}\right)^2}}{\sqrt{1+\left(\frac{f_{c1p}}{f}\right)^2}\sqrt{1+\left(\frac{f_{c2p}}{2}\right)^2}} \tag{2.23}$$

The phase of the pressure microphone is:

$$\varphi_p[deg] = arctan\left(\frac{C_{1p}}{f}\right) + arctan\left(\frac{C_{2p}}{f}\right) + arctan\left(\frac{f}{C_{3p}}\right) + 180 \tag{2.24}$$

The sensitivity of the velocity in uncorrected mode is described by the model:

$$S_u[V/(m/s)] = \frac{S_u@250Hz}{\sqrt{1+\left(\frac{f_{c1u}}{f}\right)^2}\sqrt{1+\left(\frac{f}{f_{c2u}}\right)^2}\sqrt{1+\left(\frac{f}{f_{c3u}}\right)^2}\sqrt{1+\left(\frac{f_{c4u}}{f}\right)^2}} \tag{2.25}$$

and the phase is:

$$\varphi_u[deg] = arctan\left(\frac{C_{1u}}{f}\right) - arctan\left(\frac{f}{C_{2u}}\right) - arctan\left(\frac{f}{C_{3u}}\right) + arctan\left(\frac{C_{4u}}{f}\right) \tag{2.26}$$

If the velocity signal is equalised in amplitude and phase (corrected mode), the pressure and the velocity have the same phase. In this case the velocity model is described by:

$$S_u[V/(m/s)] = \frac{S_u@250Hz}{\sqrt{1+\left(\frac{f_{c1u}}{f}\right)^2}\sqrt{1+\left(\frac{f_{c4u}}{f}\right)^2}} \tag{2.27}$$

The phase of the velocity sensor in corrected mode is:

$$\varphi_u[deg] = arctan\left(\frac{C_{1u}}{f}\right) + arctan\left(\frac{C_{4u}}{f}\right) \tag{2.28}$$

The previous model is then fit on the calibration curve, then finding the values of the corner frequencies relative to the probe under test.

The results of the calibration process are collected in a report which is supplied with the probe. The following tables summarise the parameters obtained during the calibration realised at Microflown.

Table 2.1 Calibration of the pressure microphone

Parameters pressure equations		
Sensitivity		
S_p @ 1 KHz	61.9	[mV/Pa]
Sensitivity corner frequencies		
f_{c1p} =	52	[Hz]
f_{c2p} =	1	[Hz]
f_{c3p} =	100000	[Hz]
Phase corner frequencies		
C_{1p} =	35	[Hz]
C_{2p} =	30	[Hz]
C_{3p} =	57658	[Hz]

Figures 2.9 and 2.10 show the result of the fitting or the calibration curve to the model.

In section 2.4 these models will be the reference curves for the data collected inside the Larix laboratory in Ferrara.

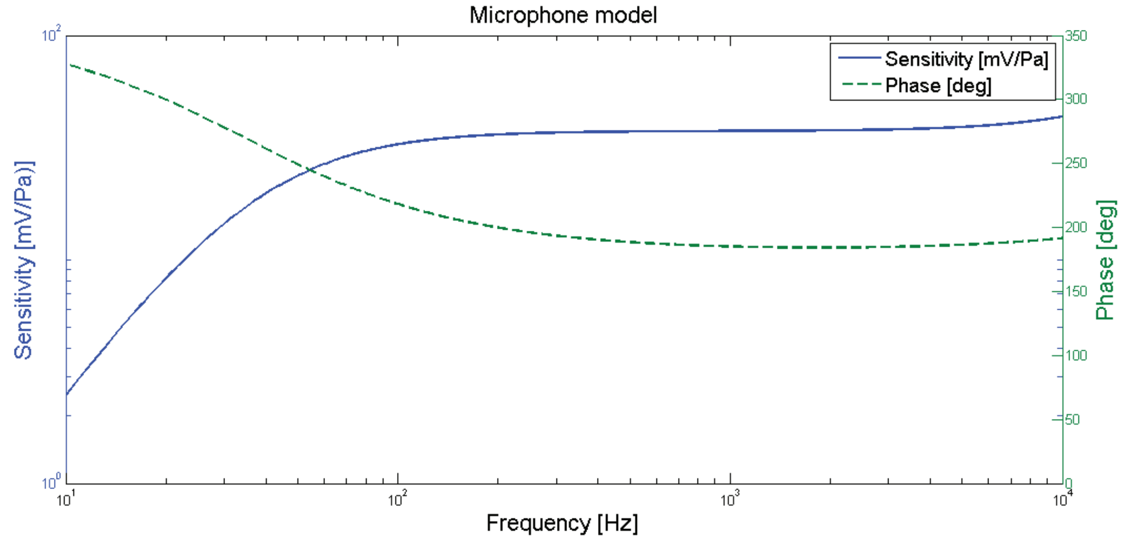

Fig. 2.9 Microphone model: amplitude (blue, continuous line) and phase (green, dotted line).

Table 2.2 Calibration of the velocity sensor

Parameters velocity equations		
Sensitivity in high gain		
S_u @ 250 Hz	25.1	[V/(m/s)]
Sensitivity in low gain		
S_u @ 250 Hz	0.251	[V/(m/s)]
Sensitivity corner frequencies		
f_{c1u} =	137	[Hz]
f_{c2u} =	554	[Hz]
f_{c3u} =	5069	[Hz]
f_{c4u} =	1	[Hz]
Phase corner frequencies		
C_{1u} =	125	[Hz]
C_{2u} =	480	[Hz]
C_{3u} =	55856	[Hz]
C_{4u} =	1	[Hz]

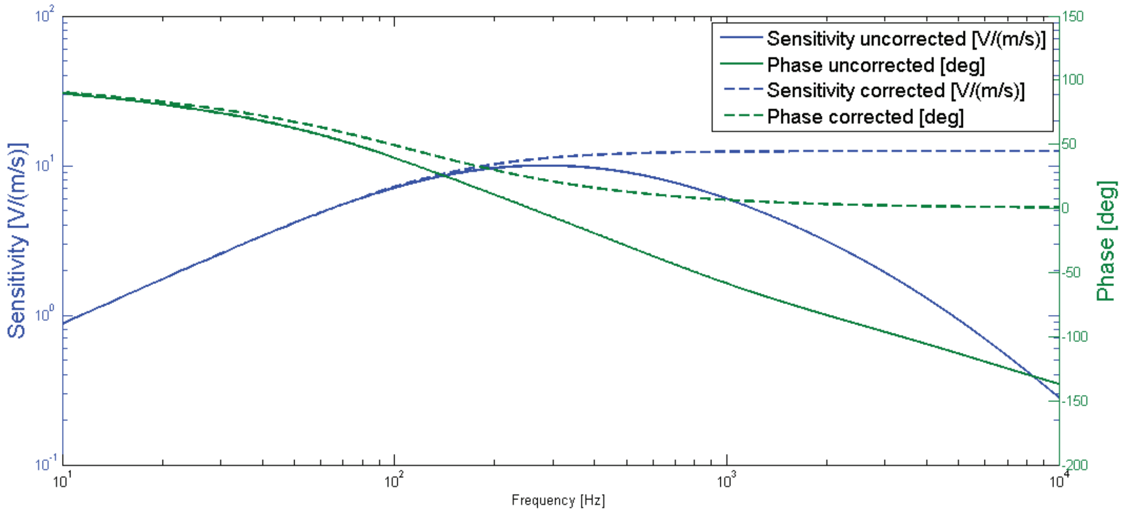

Fig. 2.10 Velocity model: amplitude in blue (continuous= uncorrected mode, dotted= corrected mode) and phase in green (continuous= uncorrected moed, dotted= corrected mode).

Fig. 2.11 The pressure velocity probe which has been calibrated at Microflown and at Ferrara.

2.3 Progressive plane wave calibration at the Larix Lab in Ferrara

A description of the procedure used at Ferrara for calibrating pressure-velocity (p-v) probes can be found in [17] and in [19]. This procedure is based on a progressive plane wave as reference field generated by a loudspeaker in the range 20 Hz-20 KHz through an impedance adaptor. For the calibration process we used a linear sweep generated by a Matlab algorithm. The development of new kind of pressure-velocity probes has required the design of new calibration methods, in order to reach a standardization in the measures of energetic acoustic quantities. A new method of calibration has been realised at the University of Ferrara: it differs from the other techniques because it's independent from the point of measurement and allows good results in just one set of measurement in wide band. Such a field is generated inside the Larix laboratory, in a 36 m tube with a diameter of 1.8 cm which will described in the next section.

The terms g(t) and $\mathbf{g}_m$(t) represent the input and the output of the measuring apparatus, in this case the p-v probe which is characterised by the impulse response m(t). These elements are linked by the correlation:

$$g_m(t) = (m * g)(t) =: \int_{-\infty}^{+\infty} m(\tau)g(t-\tau)d\tau \tag{2.29}$$

which, given a link between g and g_m continuous, linear and invariant under time translations, can be expressed through the Fourier-transformed quantities

$$G_m(\omega) = M(\omega)G(\omega) \tag{2.30}$$

However the connection between g and g_m is characterised by a transduction process, so the dimensions of the two quantities are not the same. It's necessary a parameter called S, sensitivity, which allows one to read a measurement in Pascals from a scale expressed in Volts.

So, distinguishing between the acoustic input $p(t)=\hat{p}(t)$ Pa and the electric output $\tilde{p}(t) = \tilde{\hat{p}}(t)$ V, equation 2.30 becomes

$$\tilde{p}(t) = (m * p)(t) = \int_{-\infty}^{+\infty} m(\tau)p(t-\tau)d\tau \tag{2.31}$$

Substituting in 2.31 p(t-τ)=P$_0$ δ(t- τ), we derive the impulse response m(t):

$$m(t) = \frac{\tilde{\hat{p}}(t)}{\hat{P}_0} \frac{V}{Pas} \tag{2.32}$$

with P$_0$ is a constant whose determination corresponds to the calibration of the microphone. In fact by defining

$$S = \frac{1}{\hat{P}_0} \int_{-\infty}^{+\infty} \tilde{\hat{p}}(t) dt \frac{V}{Pa} \tag{2.33}$$

one obtains

$$p(t) = S^{-1} \tilde{p}(t) \Longleftrightarrow \hat{p}(t)Pa = \hat{S}^{-1} \frac{Pa}{V} \tilde{\hat{p}}(t)V \tag{2.34}$$

The term $\hat{P}_0$ is determined by simply reading the output $[\tilde{p}]$ corresponding to a 1 Pa sample of sound pressure, usually expressed in millivolts. Since in acoustics 1 Pa corresponds to 94 dB SPL (sound pressure level), it's necessary to calculate the root mean square of the input during calibration, through a factor $1/\sqrt{2}$. The sensitivity can be determined through an absolute primary calibration, or by comparing the readings of the instrument under calibration with those measured by a pre-calibrated instrument: the last one is called *comparison calibration*. However this procedure can only be applied to pressure microphones, while the calibration of the velocity sensors is still complicated because no pre-calibrated velocity sensors are available. To calibrate the velocity sensors it's necessary to impose a relation between the pressure sensor and the velocity one: this is done by putting the probe under test in a sound reference field of a priori known impedance, and it's called *relative calibration*.

A pressure-velocity probe is clearly made up of two different sensors, a pressure and a velocity one, with their characteristic sensitivities. If both the sensors would be ideal, there would be a simple relation between the two measures, and the calibration would be accomplished by simply putting $S_2 = [\tilde{v}][p]^{-1}\rho_0 c$, where S_2 is the sensitivity of the velocity sensor [1]. However, the sensitivity of a sensor is dependent from the frequency, and a relative calibration is necessary. This procedure is based on two steps:

- comparison calibration of the microphone under test with a reference pressure microphone;

---

[1] The symbol ^ refers to the quantities expressed in Volts. The symbol ~ means the numerical (a-dimensional) value in a certain system of units [19]. In this case $\hat{S}$ refers to [V/ms^{-1}]

- correction of the velocity transfer function (magnitude and phase) over the calibrated pressure.

The second step is done by calculating the correction function Γ, which is linked to the velocity sensitivity S_2 through:

$$S_2(\omega) = \frac{\hat{S}_1(\omega)}{|\hat{\Gamma}(\omega)|} Vm^{-1}s \tag{2.35}$$

Equation 2.31 can be generalised into the equation

$$x_m(t) = \int_{-\infty}^{+\infty} x_(\tau)k(t-\tau)d\tau \tag{2.36}$$

which expresses the relation between the true signals under measurement and its recorded value, where *k* is the response of the instrument which only depends on the characteristics of the instrument. We can call p_v^0(t) and v $_v^0(t)$ the true values in the reference field, and p_m^0 (t) and v_m^0 (t) the measured values, so the quantities are linked by the expressions

$$p_m^0(t) = (u * p_v^0)(t), \qquad v_m^0(t) = (r * v_v^0)(t) \tag{2.37}$$

that can be rewritten as:

$$P_m^0(\omega) = U(\omega)P_v^0(\omega), \qquad V_m^0(\omega) = R(\omega)V_v^0(\omega) \tag{2.38}$$

from which the transfer functions of pressure and velocity can be derived:

$$U(\omega) = \left(\frac{P_m^0}{P_v^0}\right)(\omega), \qquad R(\omega) = \left(\frac{V_m^0}{V_v^0}\right)(\omega) \tag{2.39}$$

Due to the reference field conditions we can say that 2.39 only depend on the intrinsic characteristics of the sensors, then in a general field we can express the previous equation in a more general form:

$$P_m(\omega) = U(\omega)P_v(\omega) \qquad V_m(\omega) = R(\omega)V_v(\omega) \tag{2.40}$$

where the superscript 0 has been dropped just to indicate that the measurement is done in general filed conditions. Therefore the true values of pressure and velocity can be found in any point of any unknown sound field using:

$$P_v = \frac{P_m}{U} = P_m \frac{P_v^0}{P_m^0} \qquad\qquad V_v = \frac{V_v^0}{V_m^0} V_m \tag{2.41}$$

The two quantities p and $\mathbf{v}$ are correlated through the Euler equation in a single expression, that is the admittance operator Y(ω):

$$Y_v(\omega) \equiv \frac{V_v}{P_v} = \left(\frac{V_v^0}{V_m^0} \frac{P_m^0}{P_v^0} \right) \frac{V_m}{P_m} \to Y(\mathbf{x}) = \frac{Y^0}{Y_m^0} Y_m(\mathbf{x}) \tag{2.42}$$

Equation 2.42 means that the true admittance is to the measured one in a general acoustic field, as the true admittance is to the one measured in a reference field. The relative calibration ends by applying the true admittance Y(ω)= Γ Y$_m$(ω) to the true pressure signal P(ω), therefore obtaining the complex velocity signal

$$V(\mathbf{x}, \omega) = Y(\omega) P(\mathbf{x}, \omega) \tag{2.43}$$

The Larix tube represents the most simple kind of acoustic field, that is the progressive plane wave. As it's said before, in a progressive plane wave field, the value of impedance remains the same at each point, then simplifying the calibration of the device. In this field the true acoustic admittance corresponds to a real constant equal to the reciprocal of the characteristic impedance of the medium z_0:

$$Y_v^0(\omega) = \frac{V_v^0}{P_v^0} = z_0^{-1} = \frac{1}{\rho_0 c} \tag{2.44}$$

with ρ_0 the density of the air and c the velocity of the sound. The correction curve in this reference field assumes the value:

$$\Gamma^0(\omega) = \frac{Z_m^0}{\rho_0 c} \tag{2.45}$$

where Z$_m^0$ is the wave impedance measured in the calibration field, and z$_0 = \rho c$ is the characteristic impedance of the air in a progressive plane wave field.

Equation 2.45 can be expressed in a generic field as it follows [20]:

$$\Gamma(\omega) = \frac{Z_m^0}{Z_M^0} \tag{2.46}$$

where Z_M^0 is the impedance measured with a reference probe.

After defining the sensitivity of the pressure channel

$$S_p = \frac{P_m}{P_M} \tag{2.47}$$

with P_m and P_M respectively the pressure measured with the probe under calibration and the reference one, we can derive the sensitivity of the velocity channel:

$$S_v = \frac{S_p}{\Gamma} \tag{2.48}$$

2.3.1 Progressive plane wave calibration set up

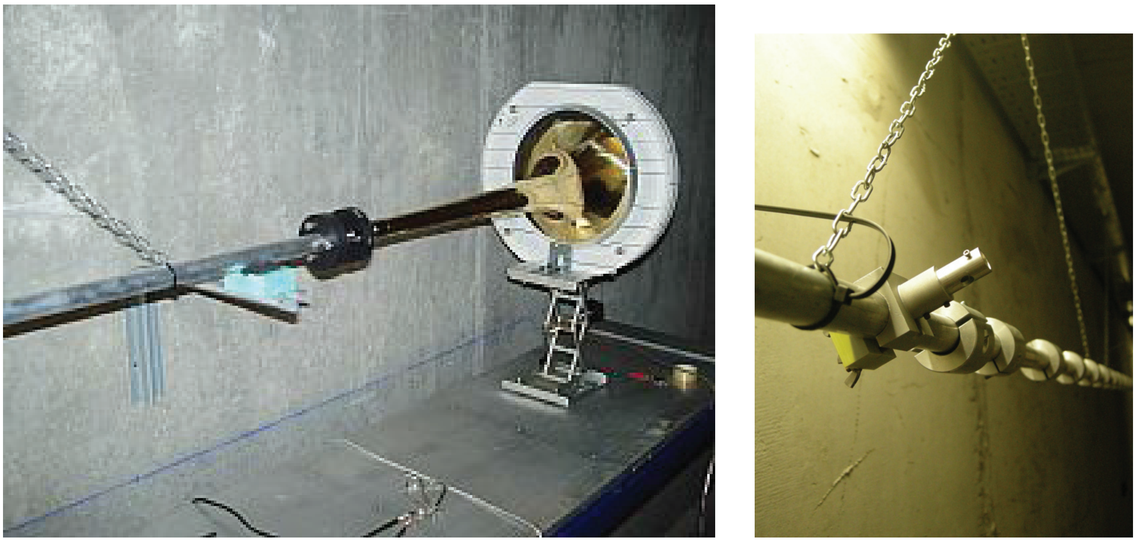

Fig. 2.12 Progressive plane wave set up: the tube.

As we said before, the comparison calibration must be done in a reference field whose impedance is known a-priori from a physical model.. The most simple model of a known impedance is the progressive plane wave field. This field has been realised inside the Larix laboratory: an underground corridor 100 m long at the University of Ferrara.

The calibration environment is represented in figure 2.12: it consists of a 36 m long, 1.8 cm wide alluminum tube, coupled at one end with a Tannoy biconical loudspeaker. A modified trombone bell, used as an impedance adaptor, grants an optimal excitation of the air column. The geometric characteristics of the wave guide guarantee the internal acoustic field to be a progressive plane wave until 10 KHz. The Larix corridor provides a good homogeneity of environmental conditions, such as humidity and temperature. The

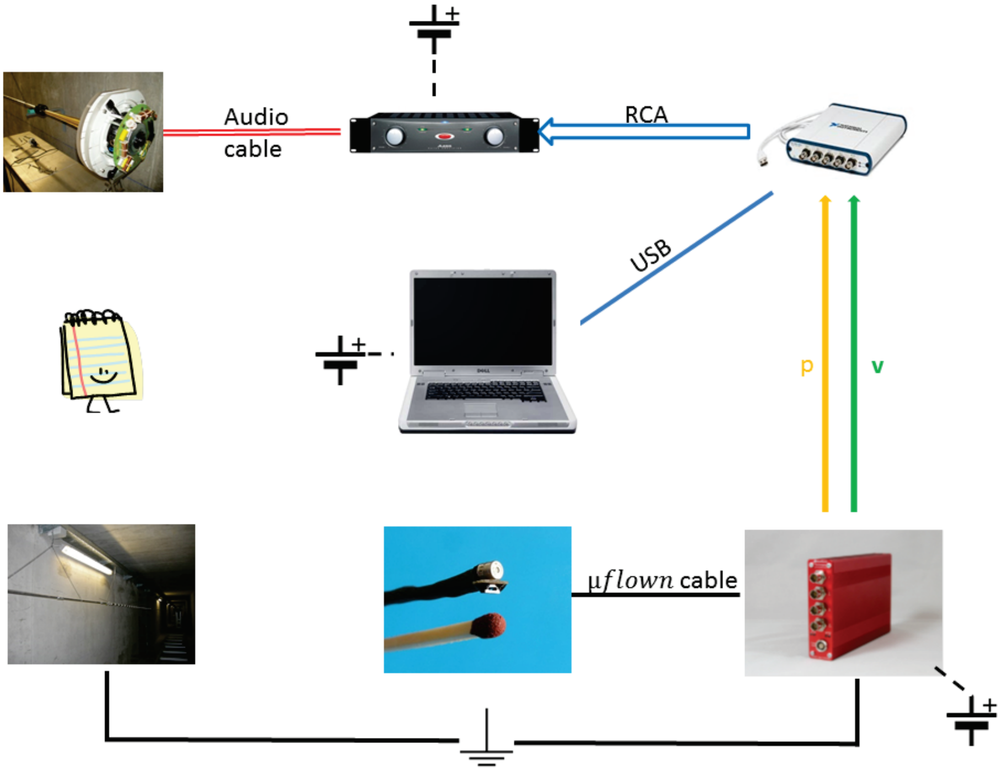

Fig. 2.13 Set up for the calibration inside Larix.

electroacoustic measurement chain is illustrated in figure 2.13 and consists of a personal computer equipped with a National Instruments®I/O USB data acquisition device (DAQ) and a power amplifier for signals driving the loudspeaker. The probe under test is the same Microflown p-v match size I calibrated during my visit in Arnhem. Digital signal processing and the dual channel fast Fourier transform (FFT) were made with dedicated Matlab routines.

For the relative calibration of the pressure channel, a 1/4 in. B&K type 4939 pressure microphone powered by a B&K Nexus conditioning amplifier was used. The first step of the calibration required the use of a B&K pistonphone (type 4231), whose nominal accuracy is ±0.2 dB.

2.4 Comparison between the calibrations

The calibration has been made with two different approaches. In the first set of measures the excitation signal was a single sine sweep of initial frequency of 20 Hz, and final frequency of 20 KHz. In order to improve the SNR, we decided to divide the measurement in three frequency bands: the first from 20 Hz to 1200 Hz, the second from 900 Hz to 2200 Hz and the last from 2 KHz to 15 KHz. For each band we raised the amplifier gain until a limit value in which the tube started vibrating. In this way each band could have the highest possible SNR.

The three bands are illustrated in figure 2.14: 20 Hz to 1200 Hz in red, dashed line; 900 Hz to 2000 Hz in green, continuous line and 2 KHz to 15 KHz in blue, dotted line. Therefore, after calibrating the pressure channel with the reference B&K microphone, we have joined the three curves by reciprocally normalising them, in order to have one single, ideal, curve.

The Matlab algorithms written for the calibration and the fitting of the correction curves can be found in appendix B, and are:

1. *imp_cat.m*: this algorithm reads the sweeps relative to the three bands of frequency (high, medium, low), it normalises and it connects them into a single sweep;

2. *calculation_of _Sp.m*: it calculates the correction curve Γ starting from the single or triple sweep recorded inside Larix. This quantity can be simply evaluated, from the experimental point of view, operating with the FFT algorithm over the synchronised responses of PV and VT [19];

3. *fitting.m*: this algorithm compare the experimental correction curve found within the previous step with the correction curve of the Microflown model, illustrated in section 2.2.4, best fitting the two curves through a number of iterations.

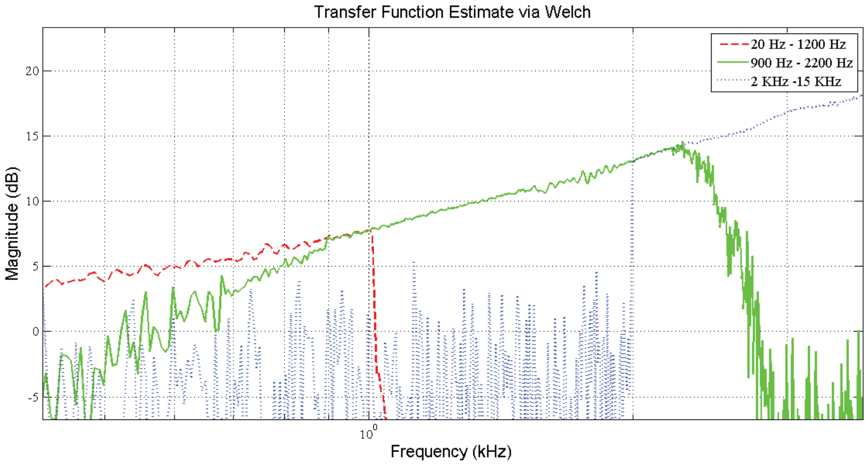

Fig. 2.14 The three bands used for the calibration of the probe: 20 Hz 1200 Hz (red, dashed line), 900 Hz - 2200 Hz (green, continuous line), 2 KHz - 15 KHz (blue, dotted line).

Figures from 2.15 to 2.17 show the results for the single sweep measurement, while figures from 2.18 to 2.20 refer to the three bands measurement.

The plots show the comparison of the fitting of correction curve with the Microflown model: blue, dashed lines are the experimental data; red, dotted lines are the Microflown models and black, continuous lines are the optimised filters by best-fitting experimental data with the analytical model curve. It can be seen that the amplitude of the experimental curve is more linear in the three sweeps measurement than in the one with a single sweep. That is because, as explained earlier, we increased the gain for each band so improving the SNR.

The nominal and the best fitted curves have a quite similar behaviour diverging at most by 10 dB at lower frequencies, where the Microflown model is less precise and there's the influence of electro acoustic shortage.

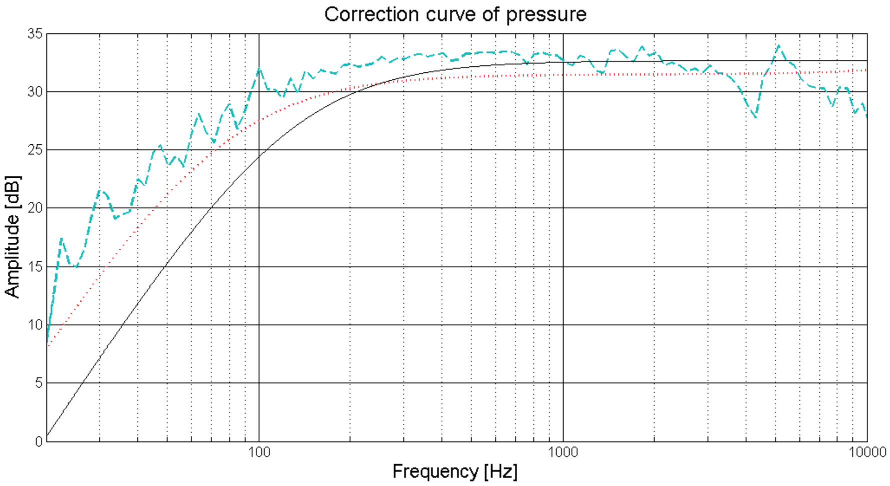

Fig. 2.15 Fitting of the pressure model, with one single sweep, amplitude.

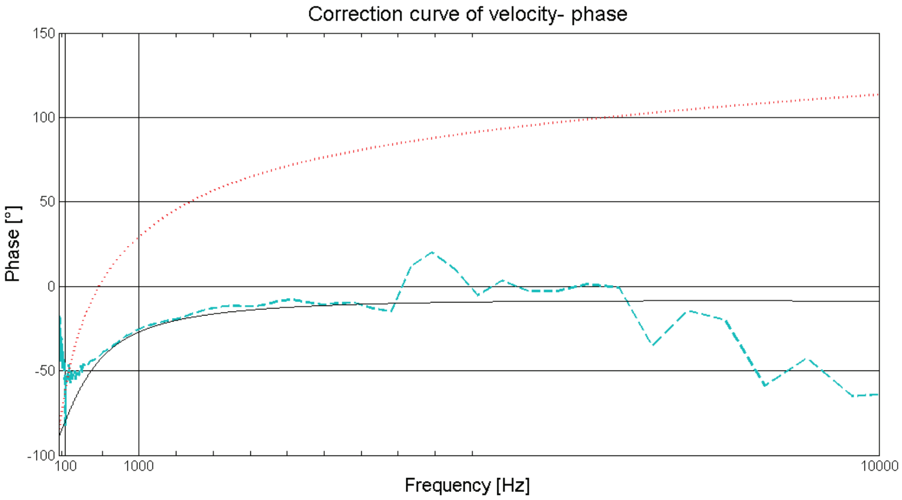

Fig. 2.16 Fitting of the pressure model, with one single sweep, phase.

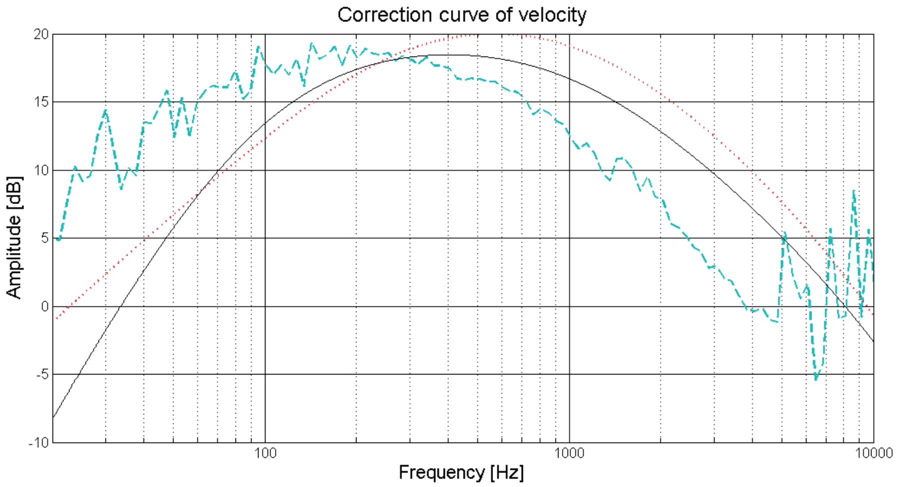

Fig. 2.17 Fitting of the velocity model, with one single sweep.

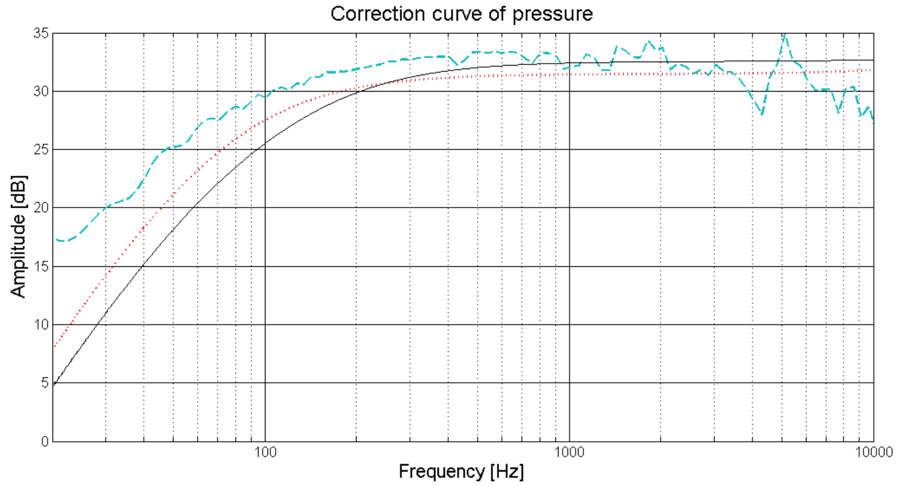

Fig. 2.18 Fitting of the pressure model, with three sweeps, amplitude.

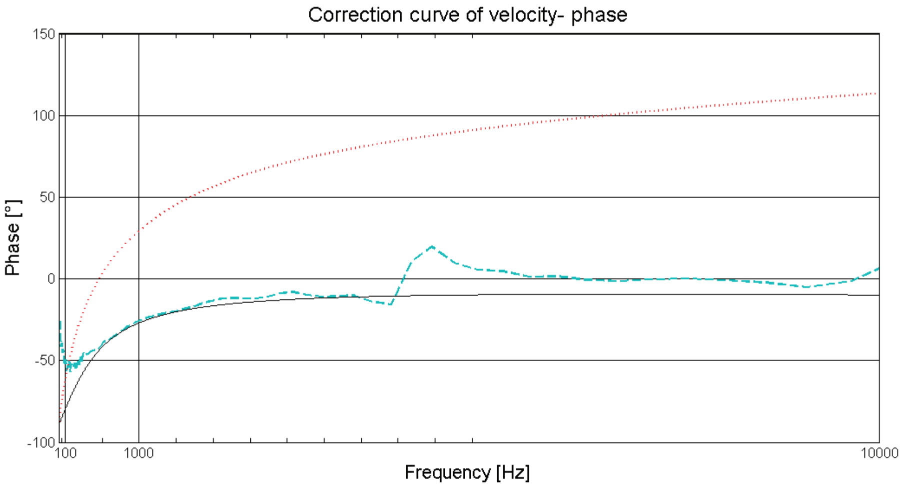

Fig. 2.19 Fitting of the pressure model, with three sweeps, phase.

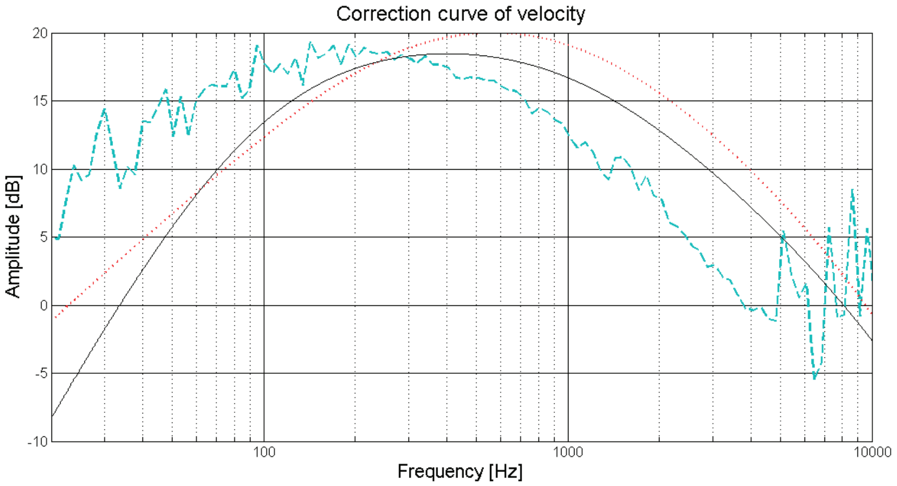

Fig. 2.20 Fitting of the velocity model, with three sweeps.

Chapter 3

The SIHT probe prototypes

The present chapter illustrates the prototypes realised during the SIHT project. The first section is dedicated to the pressure-velocity sensor and its geometry; the second one introduces the tests held at the laboratory of Ferrara to study its acoustic properties and to design an improved version of the prototype, which is described in section 3.3. The last prototype is based on a carbon fibre horn and is introduced in section 3.4.

3.1 The SIHT pressure-velocity sensor

The specific acoustic impedance is defined as the ratio between the sound pressure, p, and the acoustic particle velocity, $\mathbf{v}$, at a given point. Its measurement is important to characterise the local behaviour of any acoustic system, like wind instruments, human hear and absorbing material. Different methods make possible an impedance measurement [21], [22], but the most direct way is to directly and simultaneously detect pressure and velocity in a point, by means of a p-v probe.

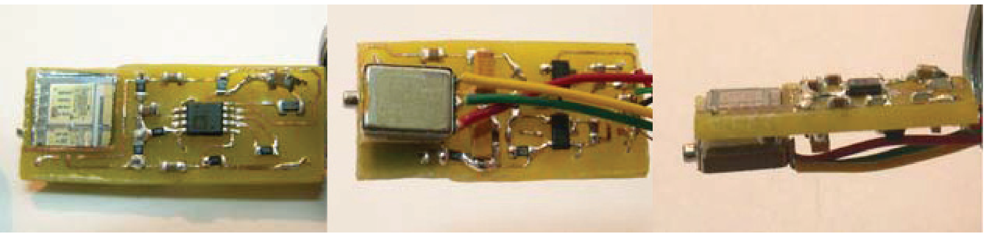

Fig. 3.1 Details of the SIHT n°1 CMOS-compatible microprobe. From left to right: velocimetric sensor, miniature Knowles microphone, the assembled p-v probe.

While the pressure is simply measured using a traditional microphone, the direct measurement of the particle velocity is more difficult because of the lack of compact sensors with a good resolution. The velocity is therefore usually derived by a pressure gradient measurement. The development of micromachining technologies have permitted the fabrication of thermal flow meters suitable for the measurement of acoustical particle velocity (APV). Within the SIHT project (Sogliano Industrial High Technology), a new pressure-velocity probe has been designed and fabricated assembling a commercial MEMS microphone, a micromachined acoustic particle velocity sensor (APV) and an electronic readout interface (Fig. 3.1). The velocity sensor is based on the variation of the heat exchange between two heaters (Fig. 3.5) caused by the flown of the air, and therefore its velocity. The heaters are two silicided n-polysilicon wires placed over suspended silicon dioxide membranes, as can be seen in figure 3.3. The wires are divided into smaller segments in order to facilitate fabrication and improve robustness, and their temperature coefficient of resistance (TCR) is used to convert the heater temperature oscillations caused by the acoustic flow into voltage variations.

The chip was designed with the BCD6s process of STMicroelectronics and included two orthogonal sensors (SX and SY, in figure 3.4). In order to thermally insulate the wires from the silicon substrate, a small amount of silicon has been removed from the front side of the chip during post-processing.

A more detailed description of the fabrication of the sensor can be found in [23]. Briefly, dielectric layers have been successively removed through a photolithographic procedure followed by a standard carbon tetrafluoride (CF_4) plasma RIE (Reactive Ion Etching). Then, the bare silicon is etched with a TMAH solution. Figure 3.5 shows the optical enlargement of the two wires, R_{W1} and R_{W2}, after the silicon removal.

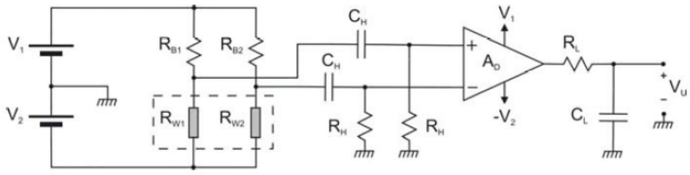

Fig. 3.2 Circuit used to bias the velocity sensor and filter and amplify the signal.

The electronic circuit of the velocimeter is showed in figure 3.2: the two sensing wires, indicated with R_{W1} and R_{W2}, form a Wheatstone bridge with two constant resistors, R_{B1} and R_{B2}. A differential high pass filter is determined by the capacitors (C_H) and by the resistors (R_H), in order to prevent DC voltages from saturating the amplifier as a consequence of bridge unbalances. While the roll-off frequency given by the $C_H R_H$ filters is around 10 Hz, the capacitor and the resistors form a low pass filter with a roll-off frequency of 30 KHz.

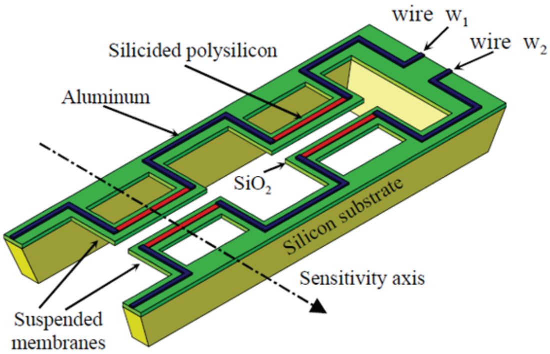

Fig. 3.3 Perspective view of part of the velocimeter.

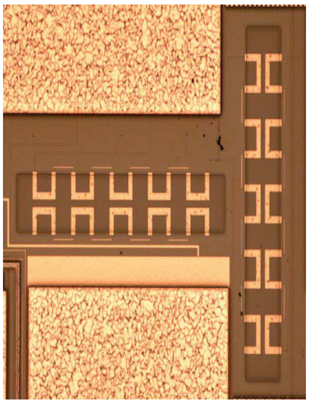

Fig. 3.4 Optical micrograph of the two orthogonal sensors prior to micromaching.

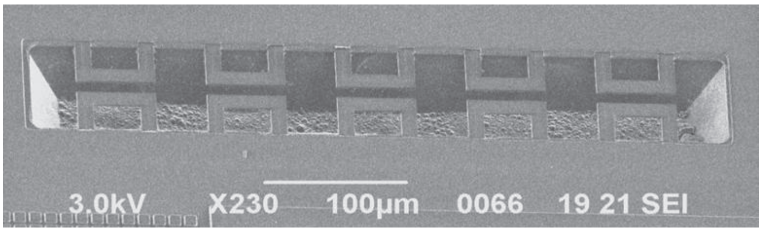

Fig. 3.5 SEM micrograph showing the five sections of the wires.

3.2 The SIHT prototype ♯ 0

The first prototype, here called "prototype ♯ 0", consists of a thermoresistant acousto-velocimetric sensor based on a CMOS-compatible technology, and has been developed by the CNR-IEIIT group of Pisa. The group of IDASC in Ferrara provided in studying the acoustic properties of this sensor [24], and this information has been used during the design and the development of the following version of the prototype (see section 3.3). For such purpose we used as a reference sensor the velocimeter included in the Microflown p-v match size and implemented the following procedure:

- preliminary tests to understand the behaviour of the electric components (i.e. amplifier, connections, stabiliser;
- comparison of the frequency responses of the prototype velocimeter with the reference one in a general environment;
- comparison of the two sensors in a controlled environment at different frequencies.

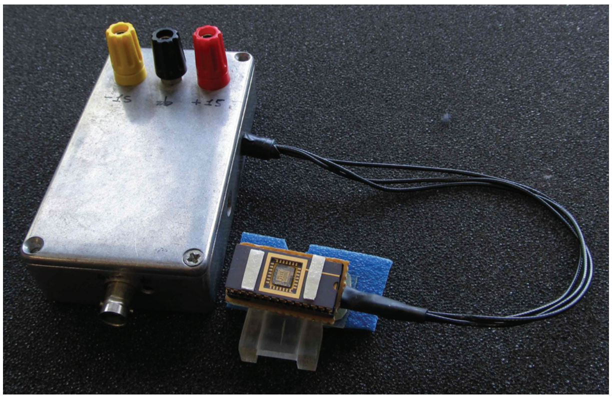

Fig. 3.6 Photo of the prototype ♯ 0 with its signal conditioner.

A first test consists in measuring the selfnoise of the prototype at different voltages. The sensor must be powered by a continuous-two poles voltage (15 ± 0.5 V). Despite the presence of a stabiliser, we can see from figure 3.8 how the decreasing of the voltage generates harmonic components due to the electrical power source.

After we set the ideal voltage at 15 V, the second phase consisted in comparing the frequency responses of the prototype velocimeter with the Microflown one. A first test has been conducted in a generic 3D environment, the laboratory of the IDASC at Ferrara University, a 100 m^3 room. The source is a sweep signal of initial frequency 20 Hz and final frequency 20 KHz generated by a Technics loudspeaker 1 m far from the sensors, placed nearly in the same position.

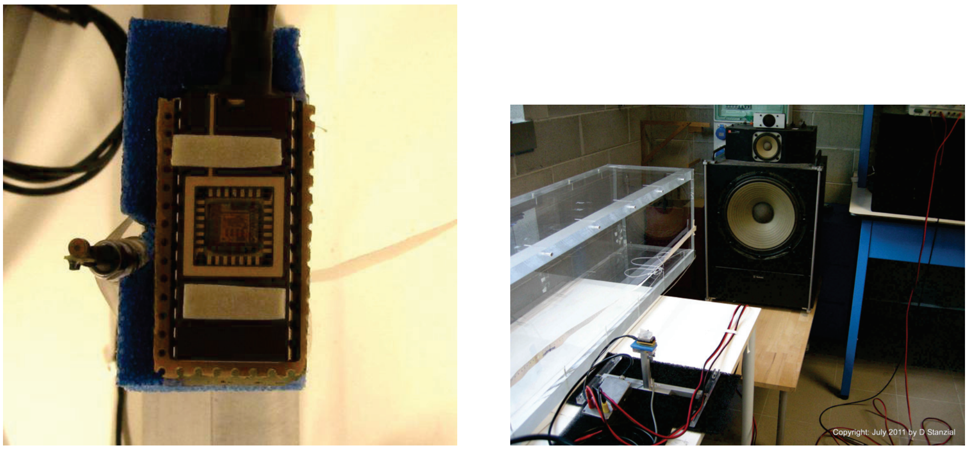

Fig. 3.7 Photo of the prototype ♯ 0 and measure environment.

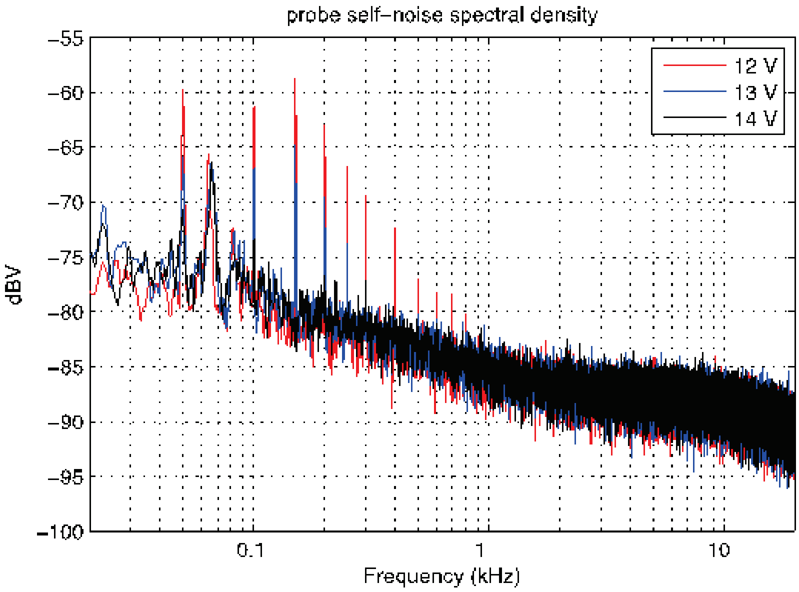

Fig. 3.8 Selfnoise of the SIHT prototype ♯ 0 relative to the frequency and voltage power supply.

The result of this test is showed in figure 3.9: the response curve is similar for the two sensors in the range of 80 to 2000 Hz, but above this limit the prototype doesn't work because of the high selfnoise.

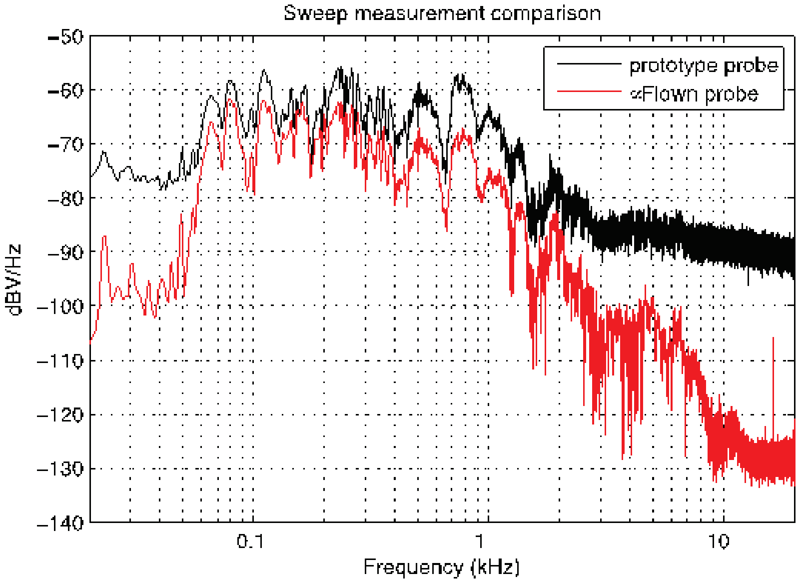

Fig. 3.9 Spectral densities of the prototype ♯ 0 and of the reference velocimeter.

The second comparison between the sensors has been conducted inside a well defined environment: a plexiglas waveguide of dimensions (0.28 x 0.28 x 4) m^3 (see figure 3.7 on the right). This time the source signal was limited to 4 KHz, because in the previous test we concluded that above that frequency the sensor is no longer sensitive. The test was conducted in two successive steps: in the first one we used as a source the mid-range loudspeaker (f<2KHz), while in the second one we used the tweeter (1.5 KHz<f<4 KHz).

The results are illustrated in figure 3.10: on the left the frequency response of the prototype, on the right the response of the Microflown velocimeter. The measures using the prototype confirm a high selfnoise, associated to a progressive loss of sensitivity with increasing frequencies.

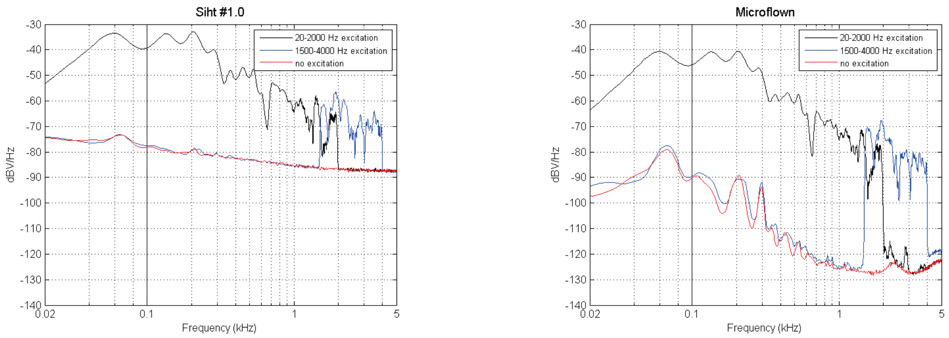

Fig. 3.10 Frequency response of the prototype ♯ 0 and of the reference velocimeter: low frequencies in black, high frequencies in blue and selfnoise in red.

3.3 The SIHT prototype ♯ 1: tympanometric p-v probe

The audiometric field has been the first application of the SIHT prototype (see section 5.1). The velocimeter has been mounted on a PCB together with a Knowles Electronics EK-23133-C36 microphone in order to build up a pressure-velocity probe. The new p-v probe has been inserted into a hollow cylinder which is used for the measurement of the acoustic immittance of the ear (Fig. 3.11). The inner diameter of such cylinder is 11 mm. The cylinder is a modified tympanometric probe, which originally hosted a miniaturised source and a tube linked to a pump, responsible for the static pressure variation [25].

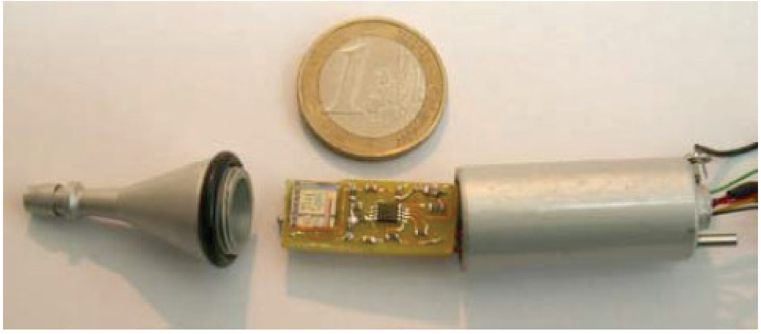

Fig. 3.11 Photo of the prototype ♯ 1.

A similar device has been realised by inserting a Microflown p-v match size probe inside a second cylinder (Fig. 3.12). This second device will be the used as the reference probe for the functional comparison of the SIHT tympanometric probe [24],[25].

Fig. 3.12 Photo of the prototype based on Microflown technology. On the right it's possible to see the in-ear phone which works as sound source.

3.3.1 Functional characterisation of a p-v tympanometric probe

Traditional tympanometry, used at present for diagnosis, limits its working range between 100 and 1200 Hz. So we concentrated our measures within this range.The particular shape of the probes required a comparison calibration, in order to cancel both the different geometries inside the cylinders and the intrinsic characteristics of the compared sensors.

Comparison test

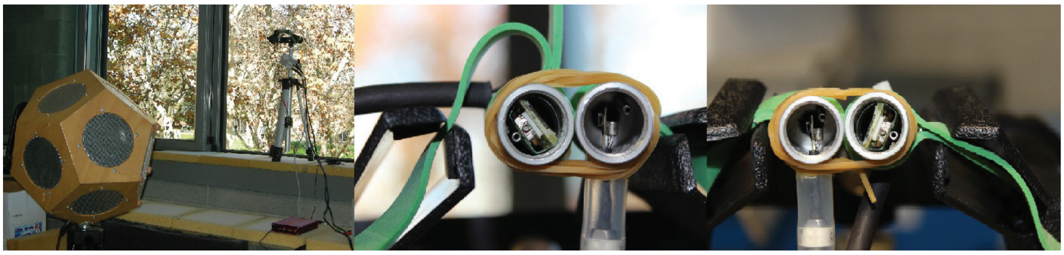

Fig. 3.13 The experimental set up for the functional comparison test. From left to right: the dodecahedral acoustic source and the tripod; the SIHT ♯1 prototype and the Microflown p-v probes; the same probes in reverse configuration.

A first test was made by comparing the Microflown and the SIHT probe. Figure 3.13 shows the experimental set up for the comparison test: it's been realised inside the laboratory of IDASC, in Ferrara, in a 100 m^3 room. It consists of a dodecahedral acoustic source and a tripod supporting the microprobes under test. The probes are located at the jamb of an open-window exposed to background noise so stressing the robustness of the collected experimental data, and exposed to a logaritmic sine sweep from 100 Hz to 1200 Hz. In order to prove the invariance of the test to the probe's position, two configurations have been tested:

the first one with the SIHT ♯ 1 probe on the left and the Microflown one on the right (fig. 3.13 in the center) and the other with a reverse orientation (fig. 3.13 on the right).

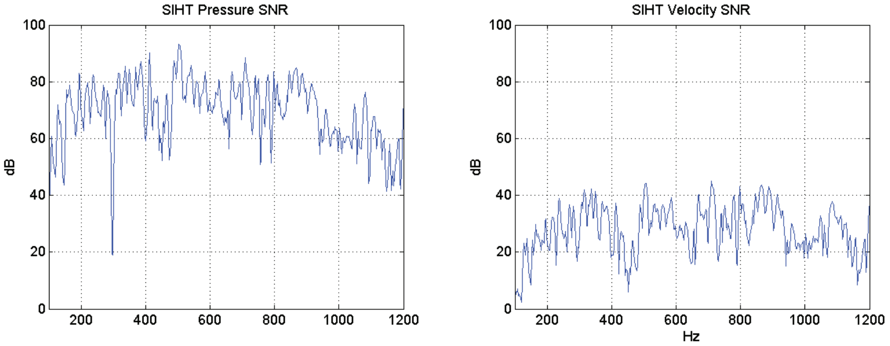

Fig. 3.14 Signal to noise ratio (SNR) of pressure (left) and velocity (right) measured with the SIHT ♯ 1 p-v probe.

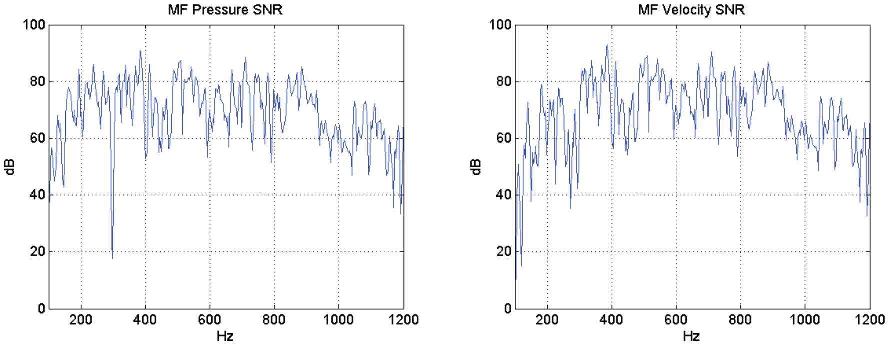

Fig. 3.15 Signal to noise ratio (SNR) of pressure (left) and velocity (right) measured with the Microflown ♯ 1 p-v probe .

Due to the importance of the admittance response in any p-v probe, a direct comparison of the signal to noise ratio for pressure and velocity of the two probes has been done. The comparison was limited to the range [10, 1200] Hz, in order to check the feasibility of the prototype as a functional device for specific acoustic admittance measurements. The results showed an invariance to the reversal test, and proved that, despite the low signal-to-noise ratio of the prototype v-sensor (SNR $\approx$ 20 dB), the correct calibration of the SIHT ♯ 1 p-v probe prototype in the range of interest of the functional device is anyway possible (see figures 3.14 and 3.15). The comparison between the admittances measured with the SIHT and Microflown probe shows the feasibility of applying a calibration process to the prototype probe in the range 100-1200 Hz.

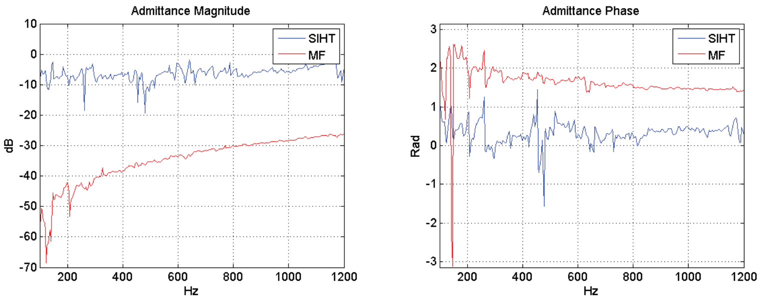

Fig. 3.16 Admittance amplitude (left) and phase (right) obtained from measures with the prototype probe (blue) and the Microflown one (red).

Calibration of the tympanometric probes using a 0.2 cm^3 volume

We considered three different standard volumes used nowadays for the calibration of the traditional impedance probes: the volumes are respectively of 0.2, 2 and 4 cm^3 (Fig. 3.17), and the relative impedances have been measured earlier with the reference probe. The three volumes present a discontinuity in the impedance value at a frequency which directly depends on the volume: we can see in figure 3.19 that this behaviour corresponds to 500-850 Hz for the 4 cm^3 volume, to 700-1000 Hz for the 2 cm^3 and to 1800-2000 Hz for the 0.2 cm^3 volume. So we chose to complete the calibration with the last one volume, because it doesn't have any resonance within the range of interest.

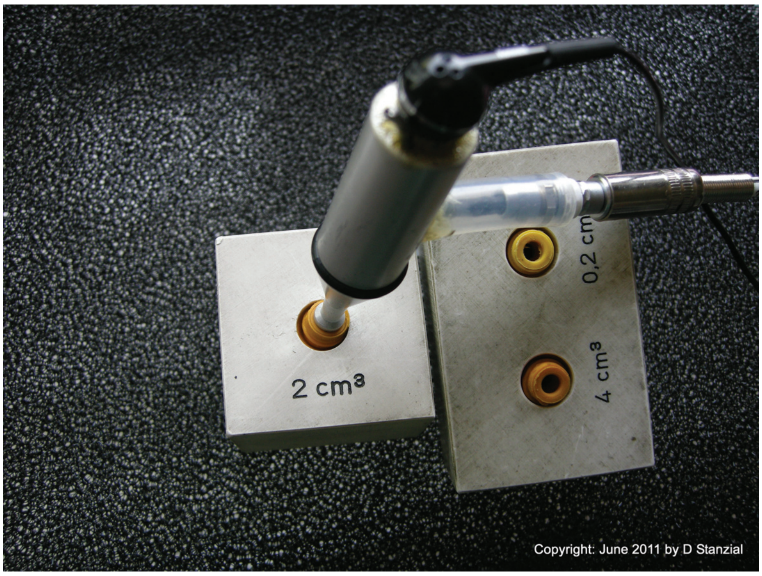

Copyright: June 2011 by D Stanzial

Fig. 3.17 Volumes for the calibration of the tympanometric probes, here used for the calibration of the prototype.

The first results of the comparison calibration using the 0.2 cm^3 volume are resumed in figure 3.18: the pressure is on the left and the velocity is on the right. Blue lines refers to the reference probe, while the red ones refers to the prototype under calibration. The wide frequency range highlights the presence of a resonance frequency between 1.5 and 2 KHz; such characteristic doesn't represent a problem, being outside the functional range for tympanometry (as we said before, between 100 and 1200 Hz).

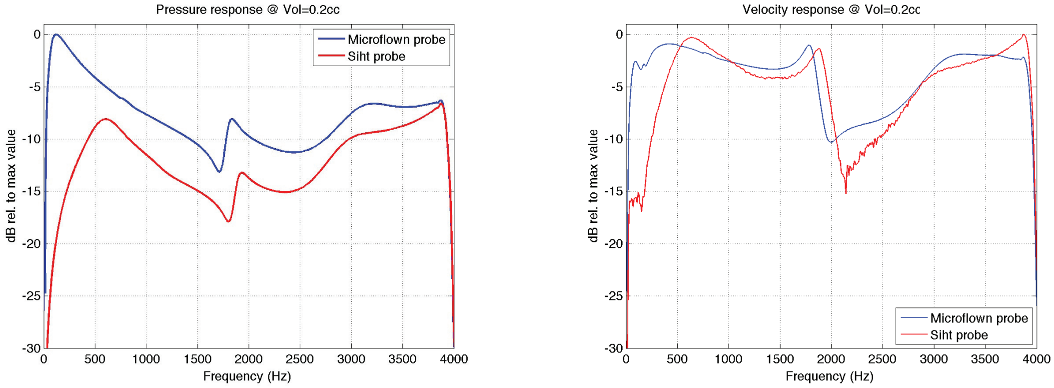

Fig. 3.18 Pressure and velocity responses of the tympanometric probes with the 0.2 cm^3 volume.

Figures 3.19 and 3.20 illustrate the comparison of the specific admittance $Y(\omega) = \mathscr{F}(v)/\mathscr{F}(p)$ between the two probes: the amplitude on the left and the phase on the right. The difference between the values depends on the unit of measure: on one side the dB level of the reference probe is expressed with respect to the value $z_0 \sim 400$ Pa/ms^{-1}, while the curve obtained with the SIHT prototype is simply obtained as the logarithm of the ratio of the velocity (Volts) to pressure (measured by the Knowles microphone). The same comparison with the same units is shown in figure 3.21, where the velocity signal of the prototype has been multiplied by a factor $1/z_0$ with the consequence of an intersection at 800 Hz.

The phase of the admittance in figure 3.20, on the right, is included in the range [200°-240°]: such difference can be reduced through the calibration of the probe.

A fully detailed explanation of the calibration procedure can be found in section 2.3 or in [19]. We remind that the correction curve $\Gamma(\omega)$ for calibrating any p-v probe can be calculated as the ratio of the reference admittance and the rough admittance measured with the probe under test. Plots in figure 3.22 compare results obtained with the prototype (in red) and the reference one (in blue), dashed lines represent data obtained with the calinrated probe. The test was made using the 2 cm^3 volume, and shows good results up to 700 Hz: above this limits the curves can't be compared.

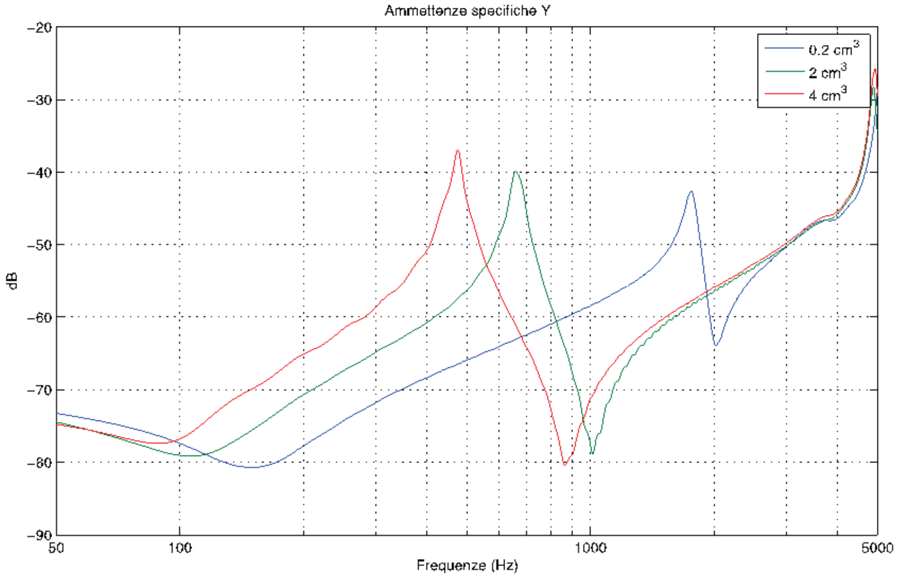

Fig. 3.19 Specific admittance measured with the tympanometric probe inside the three different volumes.

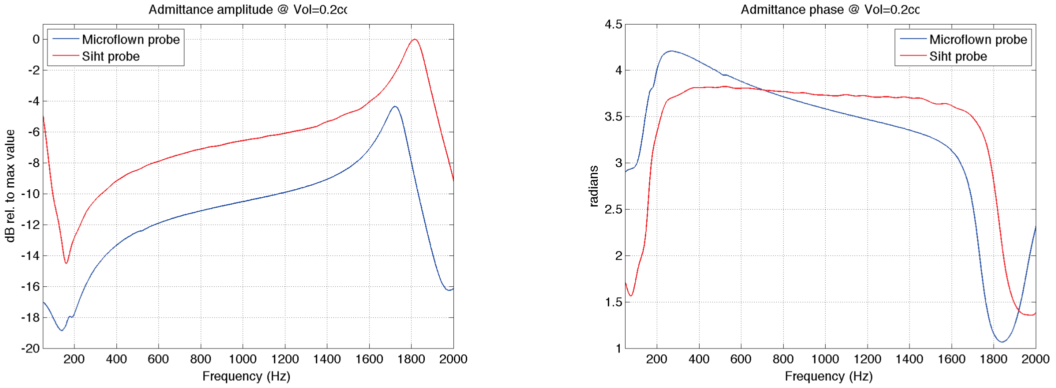

Fig. 3.20 Specific admittance (amplitude and phase) measured with the reference probe (blue) and with the tympanometric prototype (red) in a 0.2 cm^3 volume.

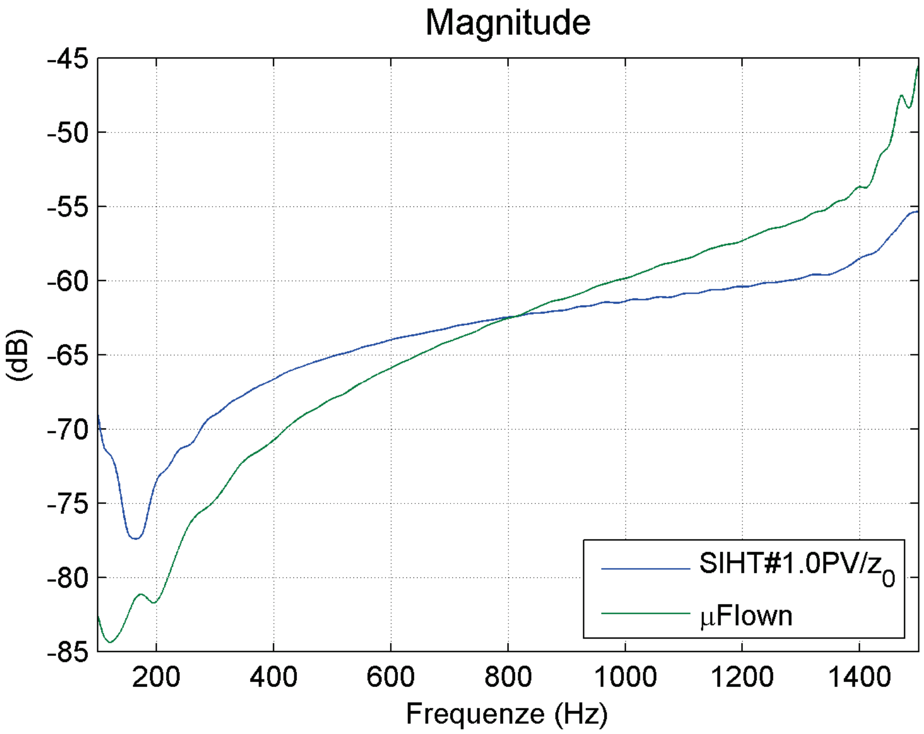

Fig. 3.21 Amplitude of the admittance measured with the two probes.

This behaviour can be explained by the different geometry of the probes (see Fig. 3.23, and in particular it depends on the big difference of the inner volumes.

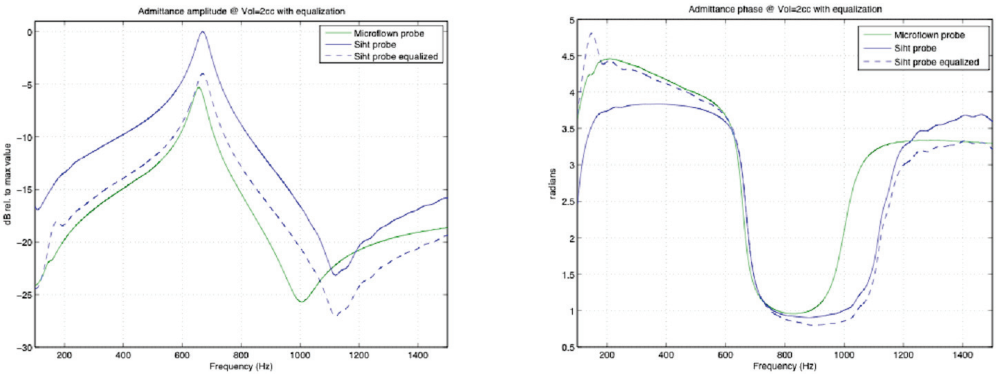

Fig. 3.22 Specific admittance measured with the prototype and its equalisation by applying the filters obtained by the comparison with the reference sensor.

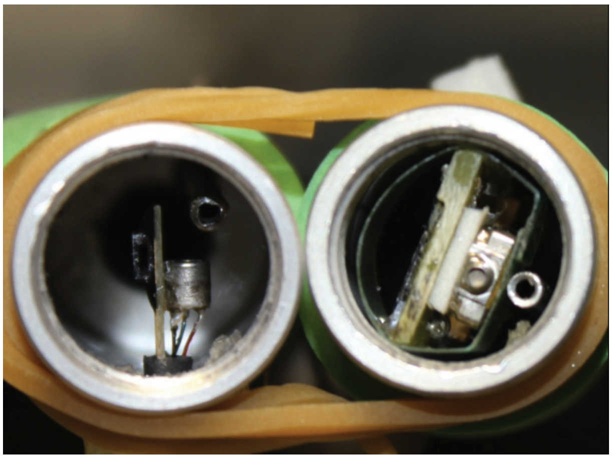

Fig. 3.23 The two tympanometric probes pulled alongside: on the left the reference tympanometric probe, including the Microflown p-v match size; on the right the CMOS prototype under test.

3.4 The SIHT prototype ♯ 2: horn-shaped p-v probe

Horns are useful devices which improve the performance of various acoustical systems. Nowadays they are used as impedance matching devices to facilitate the power transfer from a source to the receiver [26], but in the first half of the last century they were extensively used for sound reception amplifiers, both for civil and military purposes. In fact, these devices were not only used in telephony technology or for direct acoustic sensing, but they were fundamental in the detection of war planes before the invention of the RADAR (Fig. 3.24).

Fig. 3.24 Acoustic horns used for military purposes before the invention of the RADAR.

The horns were abandoned during the abrupt advances in electronics that resulted in higher sensitive microphones which didn't require additional amplification, but they have recently found a renewed interest after the development of velocimetric sensors [27]. In fact, thanks to their acoustic-fluid-dynamics properties, the particular boundary conditions of such devices give rise to a particle velocity amplification of the order of 20 dB just with horns measuring few centimetres in length.

While the fast progress in electronics and precision manufacturing resulted in highly sensitive microphone, on the other hand, the velocimetric sensors have not reached such degree of audio fidelity, then the amplification provided by the horns is fundamental. This fact has raised the interest on the study of the amplification effects both on pressure and velocity sensors so that also intensimetric measurements can take advantage on these devices, in particular under conditions when the particle velocity signal is very unbalanced compared to the pressure one.

In order to experimentally verify the effectiveness of such devices and in particular their amplification on the velocity signal, we have built and tested some conical horns made of carbon fibre. The following results show the effects of the application of the horns to a pressure-velocity Microflown match-size probe and the comparison of the laboratory test with the COMSOL-based numerical analysis.

On the basis of these results a horn-shaped p-v probe based on the SIHT low-cost sensor technology has been assembled and used for testing the comparison calibration procedure as detailed in chapter 4.

3.4.1 Theory of the horns: the Webster equation

Horn theory is described by Webster's equation, published in 1919 by Webster [28] and still used to analyse the operating principles of acoustic horns. The problem of sound propagation in horns is quite complicated, and is based on a series of assumptions and simplifications, and has not been completely solved analytically [29]. A third dimensional problem is simplified by Webster in a one-dimensional problem, assuming that the sound energy was uniformly distributed over a plane wave front perpendicular to the horn axis. The wave equation for three dimensions is described by:

$$\frac{\partial^2 \phi}{\partial t^2} - c^2 \left(\frac{\partial^2 \phi}{\partial x^2} + \frac{\partial^2 \phi}{\partial y^2} + \frac{\partial^2 \phi}{\partial z^2} \right) = 0 \tag{3.1}$$

which, in one dimension, becomes:

$$\frac{\partial^2\phi}{\partial x^2}+\frac{\partial lnS(x)}{\partial x}\frac{\partial\phi}{\partial x}-\frac{1}{c_0^2}\frac{\partial^2\phi}{\partial t^2}=0 \tag{3.2}$$

where x is the axial coordinate, ϕ is the velocity potential, c_0 is the speed of sound, and *S(x)* is the horn's cross-sectional area at position x.

Such equation can be used to understand the phenomena inside the horn, neglecting higher order effects; the assumptions which is based on are:

1. Infinitesimal amplitude: the sound pressure amplitude is negligible respect to the steady air pressure;
2. The medium is considered a uniform fluid;
3. Viscosity and friction are neglected;
4. No external forces (i.e. gravity) act on the medium;
5. The motion is assumed irrotational;
6. The walls of the horn are perfectly rigid and smooth;
7. The pressure is uniform along the wave front.

The solutions of the wave equations depends on the horn's geometry. For example, for a straight pipe, with S(x)=const:

$$\phi^{pipe}=Ae^{j(\omega t-kx)}+Be^{j(\omega t+kx)}, \tag{3.3}$$

for a conical horn, with S(x)∼x^2, we have:

$$\phi^{cone}=\frac{A}{x}e^{j(\omega t-kx)}+\frac{B}{x}e^{j(\omega t+kx)} \tag{3.4}$$

and for the exponential horn, where S(x)∼e^{mx}, with m the flaring rate, the solution is

$$\phi^{exp}=e^{(-mx)/2}[Ae^{j(\omega t-kx)}+Be^{j(\omega t+kx}] \tag{3.5}$$

where

constants A and B are determined by the boundary conditions;
ω is the circular frequency [Hz];
k is the wave number [m^{-1}];

t is time [s];

i is the imaginary unit.

The simplifications introduced in 3.2don't take into account neither the directional effects nor the inevitable diffractions that appear when the wavelengths of the incident sound become comparable to the geometric dimensions of the horns. That's the reason why our work has been extended with numerical simulations.

As clearly stated in [26] and [30], when the acoustic horn is used as a pressure amplifier, its size has to be large compared to the sound wavelength and the throat impedance needs to be as large as possible, so the ideal horn has a closed throat. On the contrary, the velocimetric horns must be open at the throat, because the amplification factor is proportional to K=R_2/R_1, being R_2 and R_2 the radius of the mouth and the throat respectively.

3.4.2 Effects of the geometry on the horns

Three independent geometrical parameters can influence a horn's performance: the length l, the throat radius R_1 and the mouth to throat ratio K=R_2/R_1. Such parameters are illustrated in figure 3.25.

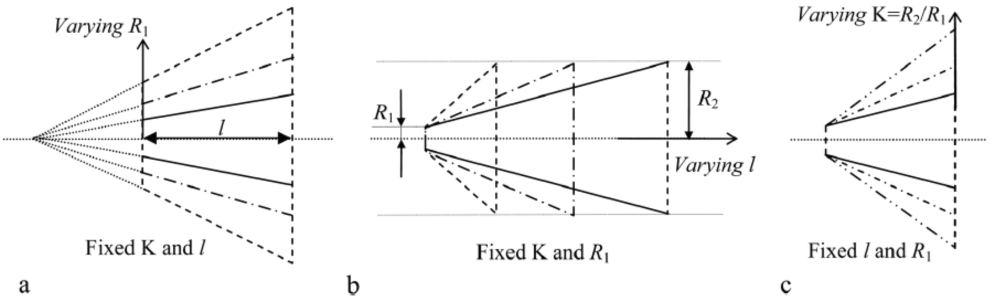

Fig. 3.25 Geometrical parameters of the horns: radius (left), length (center), ratio of the radii K (right) [26].

Figure 3.26 shows the amplification factors relative to the geometrical variations of every parameter. From this figure we can see that increasing the length of a conical horn, for fixed K ratios and a given throat radius, increases amplification. At a fixed length, amplification decreases with increasing throat diameter, because of the increased reflection inside the horn. Finally, we can say that the horn amplification is always greater for smaller throat radii and then increases with increasing mouth-to-throat radii ratios, K.

Figures 3.27 show the axial velocity amplification for different types of horns. The first plot illustrates a comparison between exponential, single conical and double conical horns:

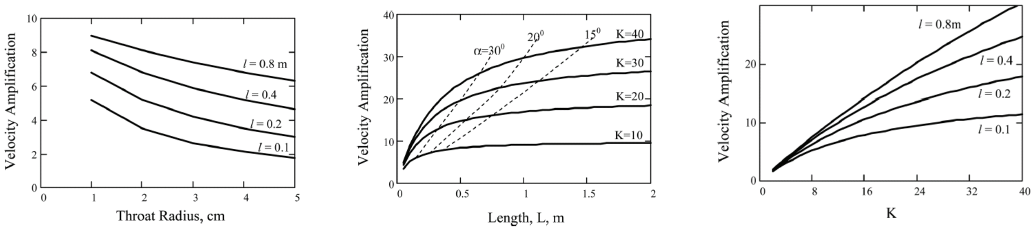

Fig. 3.26 Effects of varying the geometrical parameters on the amplification factor of the horns: radius (left), length (center), K (right) [26].

it's evident how the conical horn guarantees a greater amplification than the exponential one, moreover, the double conical horn has the greatest amplification factor.

The plot on the right shows highlights another advantage in the double conical horn: the symmetrical distribution of axial velocity, and a greater amplification outside the resonance frequency.

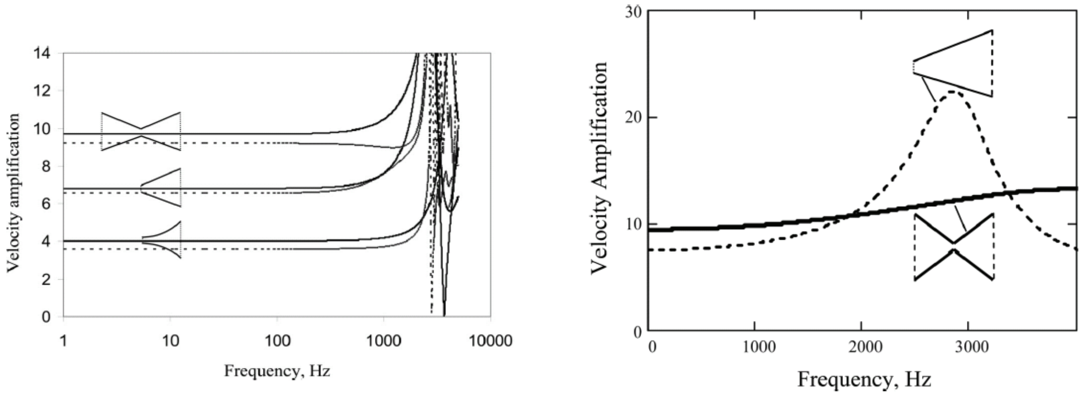

Fig. 3.27 Velocity amplification for different types of horns: on the left conical, exponential and double conical horns; on the right single and double conical horns [26].

3.4.3 Materials and methods

With these preconditions the Deltatech company in Sogliano al Rubicone (FC) collaborating with the CNR-IDASC research section of Ferrara, has built a carbon fibre conical horn 75 mm long, with a mouth radius of 30 mm and a throat radius of 6 mm 3.28. The results are presented in [31] and in [27]. In the future we have planned to improve the device by realising a double conical horn, which the authors in [26] and in [30] have demonstrated to be the best shape in terms of velocity amplification. While the cited authors studied the effects of the horns in water, we analysed the amplification effects in air.

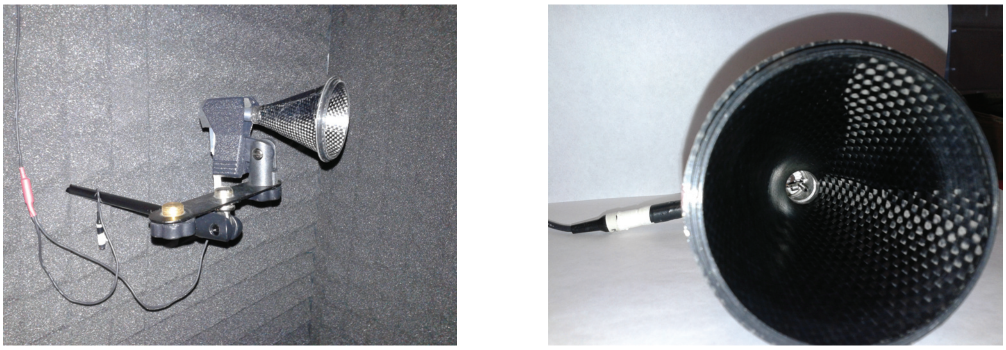

Fig. 3.28 Horn made of carbon fibre applied to the p-v Microflown probe.

As a consequence of the chosen dimensions, the first resonance frequency is 1825 Hz as given in:

$$f_{res}^{horn} = \frac{c}{2(l + 0.613R_1 + 0.613R_2)} \tag{3.6}$$

where:

l is the length of the horn [m];

R_1 is the radius of the throat [m];

R_2 is the radius of the mouth [m].

In order to verify the effect of the horn on the probe, we have compared the pressure and velocity signals measured with and without horn. A first set of tests has been arranged by measuring the pressure and velocity signals generated by pure tones emitted by the source, a Technics SB7000 loudspeakers system, while keeping the horn a m far from the speaker. In order to reduce the high measured variability, we have built a 1 m^3 noise-insulating chamber (Fig. 3.29) surrounding the probe and we have placed the source outside at a distance of 4 m. In this way the signal reaching the horn could be approximated to an homogeneous wavefront with little background noise. The measurement set up has allowed us to verify the amplification factor of the velocity signal and to establish the better position of the probe inside the horn, that is the one in which the sensor is nearest to the horn's mouth.

The test consisted in the emission of three different kinds of signals: pure tones at the central frequencies of the reference octave bands (31- 63- 125- 250- 500- 1000- 2000- 4000- 8000 Hz) and white noise filtered both in octave and third octave bands.

The following plots (figures 3.30 to 3.34) resume the obtained results relative to the amplification factor. In particular we have calculated the gain in dB of the probe+horn system compared to the probe without the conical horn.

Figure 3.30 shows the amplification factor of the pressure (blue, continuous line) and of the velocity (red, dotted line) signals for the pure tones stimulus, while figure 3.31 and 3.32

Fig. 3.29 Noise-insulating 1 m^3 chamber .

show the same measures but for white noise filtered in octave and third octave bands. The sounds were generated by the loudspeaker facing a window of the noise-insulating chamber.

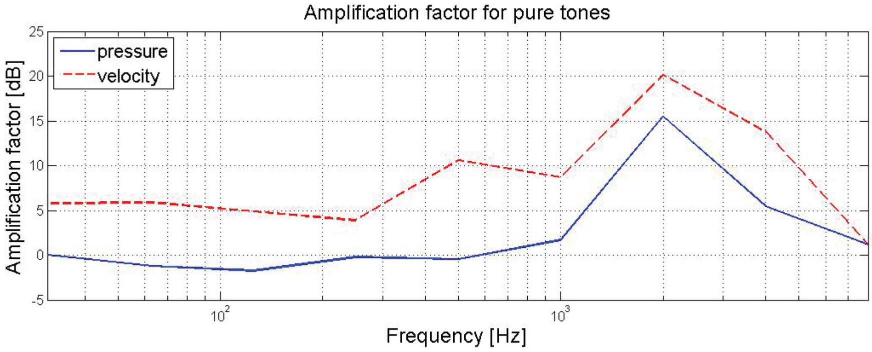

Fig. 3.30 Amplification factor for pure tones: pressure in blue, continuous line; velocity in red, dashed line.

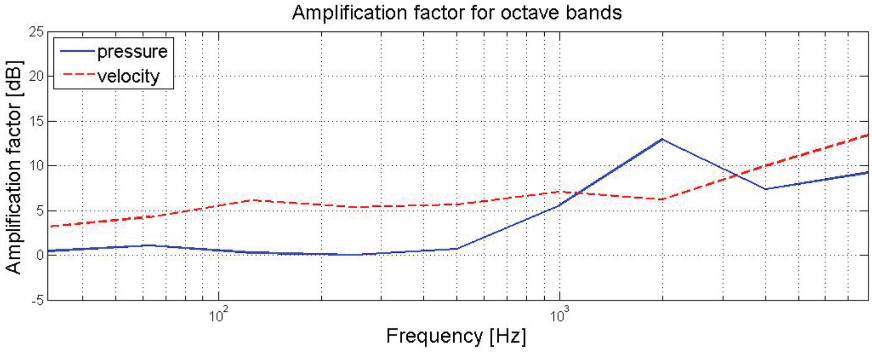

Fig. 3.31 Amplification factor for octave bands.

A preliminary analysis points out a peak in the amplification factor both for pressure and velocity, which presumably correspond to a resonance frequency in the pure tone

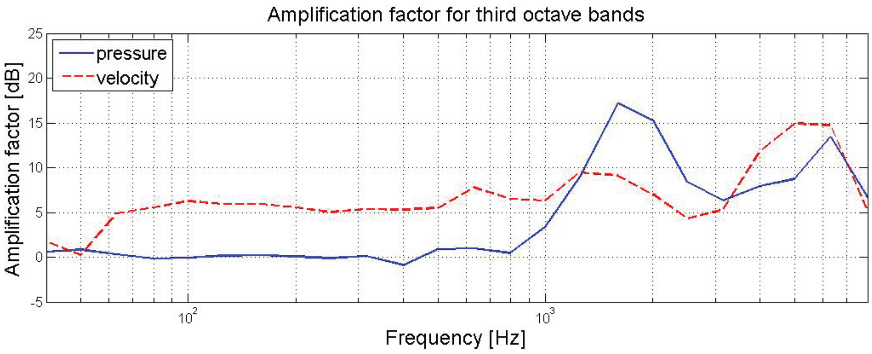

Fig. 3.32 Amplification factor for octave bands.

measurements. The same behaviour is confirmed by the measures with the filtered white noise for the pressure (Fig. 3.31), while the velocity presents a more stable gain in the 2 KHz region, followed by an increase at higher frequencies.

Figures 3.33 and 3.34 resume the results of the amplification factors for pressure and velocity respectively. The plots clearly illustrate how the pressure amplitude is not altered by the presence of the horn except in correspondance of the resonance frequency. This result confirms the theory of the authors in [26] according to which the throat affects the velocity but not the pressure.

In confirmation of this we can observe how velocity is amplified by more than 5 dB at al frequencies: the effect appears more evident when using pure tones, where the gain factor reaches a value of 20 dB (at 2 KHz).

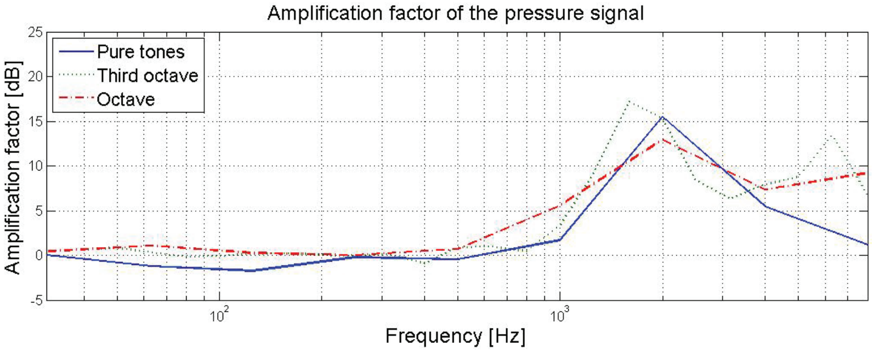

Fig. 3.33 Amplification factor of the pressure signal: pure tones in blue, continuous line; third octaves in green, dotted, line and octave in red, dash-dotted line.

In order to verify the experimental results and to study the effect of the geometry of the horn on the amplification factor, we computed a simulation using COMSOL 4.4 aeroacoustic model; in particular we used the linearised potential flow module in frequency domain, where the wave equation, expressed in the coordinate system moving with the fluid (air) at velocity

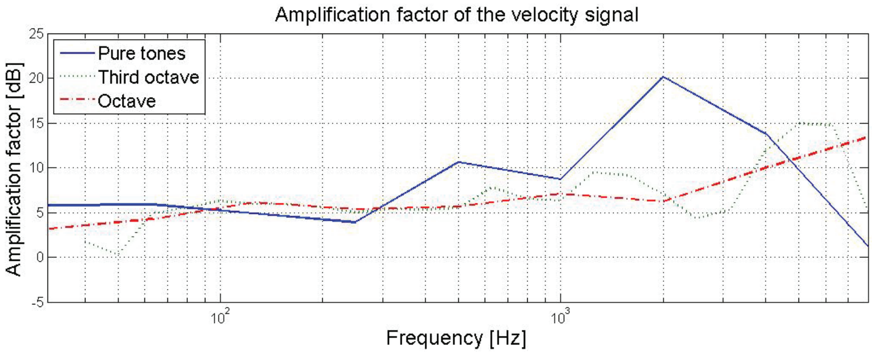

Fig. 3.34 Amplification factor of the velocity signal: pure tones in blue, continuous line; third octaves in green, dotted, line and octave in red, dash-dotted line.

v, is given in terms of the velocity potential ϕ as:

$$-\frac{\rho}{c_{mf}^2}(i\omega\phi+\mathbf{v}\cdot\nabla\phi)+\nabla\cdot\left(\rho\nabla\phi-\frac{\rho}{c_{mf}^2}(i\omega\phi+\mathbf{v}\cdot\nabla\phi)\mathbf{v}\right)=0 \tag{3.7}$$

with:

ρ the density of the air [kg/m^3];

c$_{mf}$ the velocity of the sound in the material (air) [m/s].

In order to simplify the simulation, we set the velocity **v**=0.

The fluid is assumed compressible, inviscid, perfectly isentropic and irrotational [32]. With these conditions, we can describe the pressure field p(**v**,t) and the velocity field v(**r**,t), in terms of the potential ϕ:

$$v(\mathbf{v},t)=\nabla\phi, \qquad p(\mathbf{r},t)=-\rho\frac{\partial\phi}{\partial t} \tag{3.8}$$

In order to simplify the model and to reduce the computation time, we adopted a two-dimensional axisymmetrical geometry, with all the surfaces assumed to be acoustically rigid, and with values of air density and speed of sound of 1.2 Kg/m^3 and 343 m/s.

The simulated sound field was a 94 dB SPL plane progressive wave incident at the horn's mouth. Figure 3.35 illustrates the results of the simulation. Here are reported the RMS values of the particle velocity for octave bands central frequencies: the amplification effect of the throat compared to the mouth is evident, so confirming the experimental results.

Table 3.1 and figure 3.36 resume the comparison between the amplification factors of velocity found through measurements and numerical simulation. It can be noticed that the resonance peak is shifted to higher frequencies in the simulation plot, but the overall amplification of the velocity signal is still confirmed. The systematic higher values found

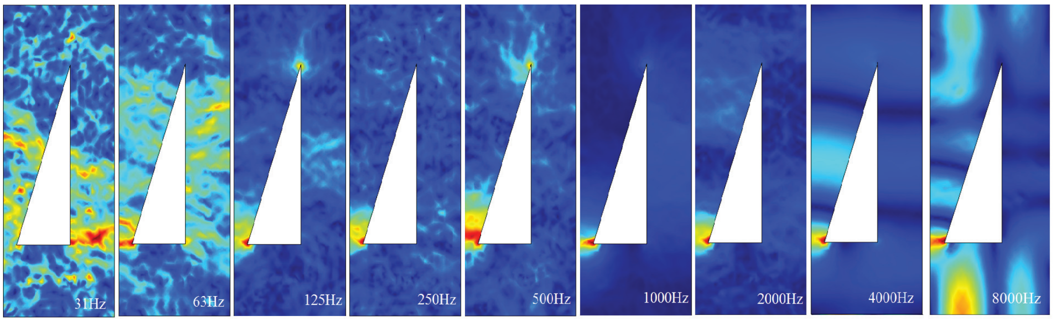

Fig. 3.35 COMSOL modeled particle velocity (RMS) within a horn with the same dimensions of the one used for the measures, scaling different for each frequency.

during the COMSOL simulation find an explanation in the different environmental conditions: a plane progressive wave field has been used during the simulation, an ideal condition which is unlikely to have been satisfied by the experimental set up.

Table 3.1 Experimental and simulated amplification factors

Frequency [Hz]	**Gv pure tones [dB]**	**Gv octave [dB]**	**Gv third octave [dB]**	**Gv COMSOL [dB]**
31	5.8	5.3	5.3	0.67
63	5.9	6	6.9	7.59
125	4.9	6.7	7.04	12.63
250	3.9	5.02	5.15	13.73
500	10.6	5.33	5.15	13.38
1000	8.7	6.11	6.15	18.22
2000	20.1	5.19	6.4	10.72
4000	13.8	7.15	8.9	8.65
8000	1.2	5.6	4.42	12.19

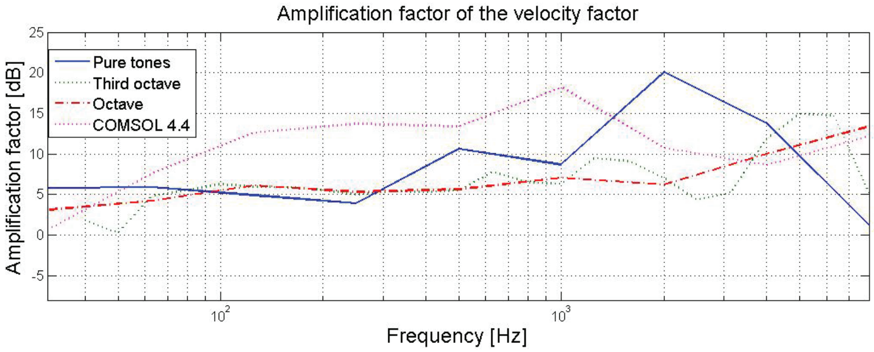

Fig. 3.36 Amplification factor of the velocity signal: pure tones in blue, continuous line; third octaves in green, dotted, line and octave in red, dash-dotted line. In dotted, pink line the simulation results.

Chapter 4

Comparison calibration of p-v probes prototypes

The methods of calibration of the p-v probes has some disadvantages, in fact they requires particular reference fields that can be reproduced using bulky devices: i.e. an anechoic room [16], a stationary wave tube or a piston in a sphere (see section 2.2 or [15]), or a progressive plane wave tube like in Larix (see section 2.3). It's evident the benefit to extend the method of calibration used for pressure microphones to the p-v probes, this is especially useful when a p-v probe is still in a prototypical stage.

It is clear that any comparison calibration procedure requires a pressure-velocity reference probe, pre-calibrated in one of the previous reference fields: this can be done by using a reference velocimeter, in our case the Microflown one. In this way the reference field is now substituted by a reference probe.

The theory of the comparison calibration is derived from the procedure described in chapter 2, where to the a-priori known impedance of the reference field (in the case of Larix ρc), we substitute the impedance measured with the pre-calibrated reference probe in a generic field where the calibration is made.

This chapter describes in detail the procedure for the comparison calibration of p-v probes.

4.1 Methodology and instrumentation

4.1.1 Calibration of the measurement system

In order to arrange a comparison calibration, first of all it's necessary to calibrate the measure system, starting from the sound card. For our measurements it's been used the MOTU 896HD

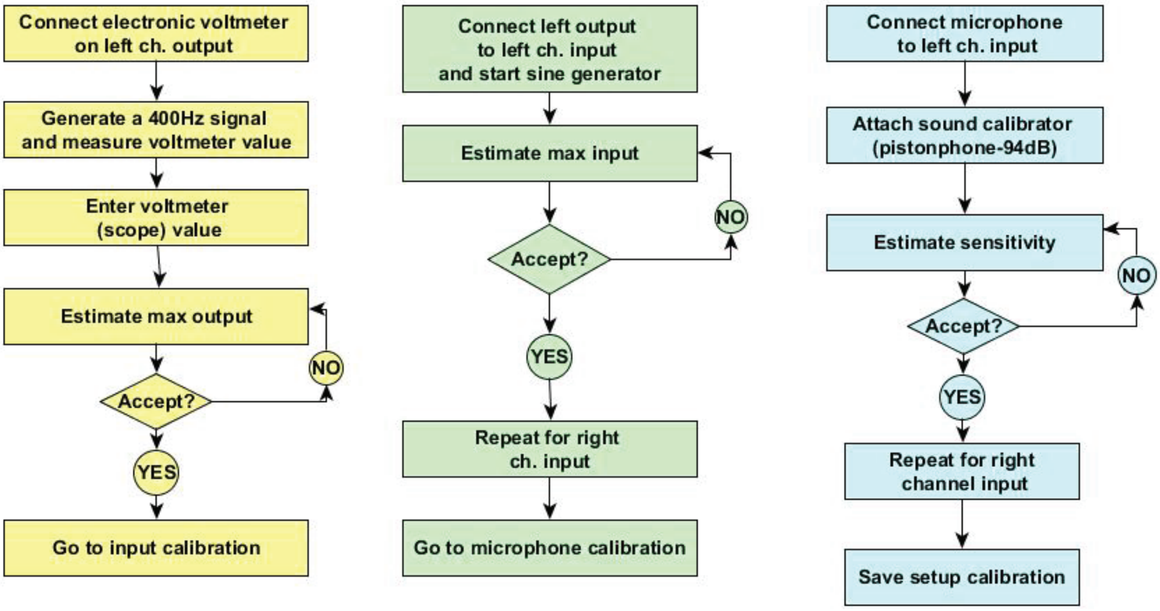

Fig. 4.1 Scheme for the calibration of the sound card following [11].

audio interface, directly connected to the laboratoty PC via FireWire, and the software ARTA. The reference microphone for this first step was a Bruel & Kjaer 1/8 inch microphone, and the measures were performed inside the laboratory in Ferrara.

As proposed in [11] the calibration of the sound card can be executed as shown in figure 4.1 and consists of three stages: the output calibration, the input calibration and the microphone calibration. In the output calibration, the electronic voltmeter is connected to the left line output channel and a 400 Hz signal is generated. The measured value in Volt has to be entered in the box, while the estimated value will be shown in the relative box. Once satisfied with the measurement, it's possible to accept the value and it will become the current value of the "LineOut Sensitivity", and it will be entered as a value for the next step, the input channel calibration. After connecting the left output to the left line input, we generate a 400 Hz sine and enter the value of signal generator voltage in the edit box, then the max input is estimated and if its value is satisfying, we accept it and such value will become the current value of the "LineIn sensitivity". This procedure has to be repeated for the right input channel. Finally, for the calibration of the microphone it's necessary to use an external generator, such as a pistonphone. This acoustical calibrator emits a sine tone of 1 KHz of 94 dB and is used to calibrate every channel of the sound card. After connecting the microphone preamplifier to the soundcard input we enter the preamplifier gain, attach the calibrator on the Bruel & Kjaer microphone and press "Estimate mic sensitivity". If the measured value is satisfying, we press the button "Accept".

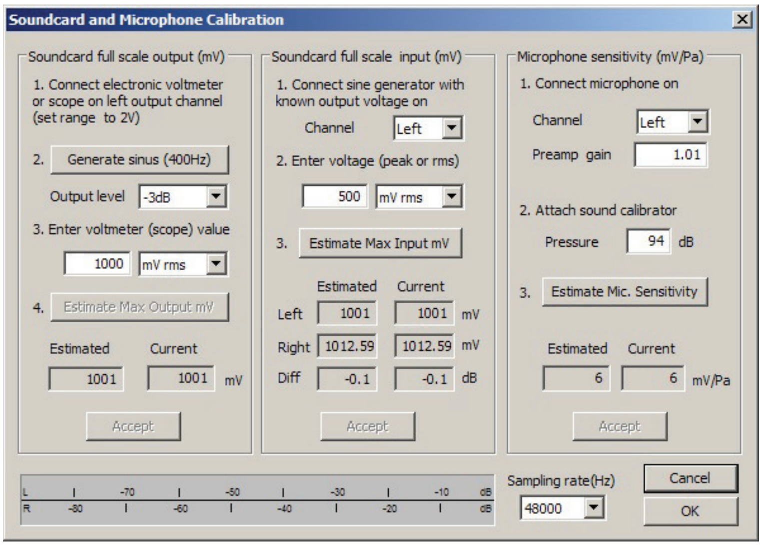

Soundcard full scale output (mV)

1. Connect electronic voltmeter or scope on left output channel (set range to 2V)

2. Generate sinus (400Hz)

Output level -3dB

3. Enter voltmeter (scope) value

1000 mV rms

4. Estimate Max Output mV

	Estimated	Current	
	1001	1001	mV

Soundcard full scale input (mV)

1. Connect sine generator with known output voltage on

Channel Left

2. Enter voltage (peak or rms)

500 mV rms

3. Estimate Max Input mV

	Estimated	Current	
Left	1001	1001	mV
Right	1012.59	1012.59	mV
Diff	-0.1	-0.1	dB

Microphone sensitivity (mV/Pa)

1. Connect microphone on

Channel Left

Preamp gain 1.01

2. Attach sound calibrator

Pressure 94 dB

3. Estimate Mic. Sensitivity

	Estimated	Current	
	6	6	mV/Pa

Sampling rate(Hz) 48000

Fig. 4.2 Window of the ARTA software to calibrate the sound card.

Once calibrated the sound card, it's necessary to calibrate the whole system, including the probes. This procedure is showed in figure 4.3 and is limited to 1 KHz: first the gain knobs of the sound card are put to zero, and the response to a 1 KHz signal is measured with the reference microphone. Then the same signal is measured with the probe to calibrate, and the gain is modified, by rotating the knobs, until the same value as the reference one is obtained.

4.1.2 Pre-calibration of the reference p-v probe (Microflown) inside Larix

After calibrating the system, it's necessary to calibrate the reference p-v probe (in our case a Microflown match-size probe) inside Larix, in order to use it for impedance measurement as described in section 4.1.3.

A first test consists in measuring the background noise of the complete measurement system, in order to verify and eventually correct any disturbances (fig. 4.5).

The next step is to insert the Bruel & Kjaer microphone in the last hole of the pipe (see Fig. 4.4), at 10.80 m from the source (a dual cone loudspeaker), and to measure the RMS of a sine signal of 1 KHz using a previously calibrated input channel (channel 7 in our case), whose result is in Fig. 4.6.

The measured RMS value becomes the target for the reference probe: after inserting it into the same hole, we measure the 1 KHz signal with the Microflown probe, and we modify the preamplification gain in the calibration set up in order to reach the same value measured with the reference microphone, both for pressure and for velocity channel (fig.

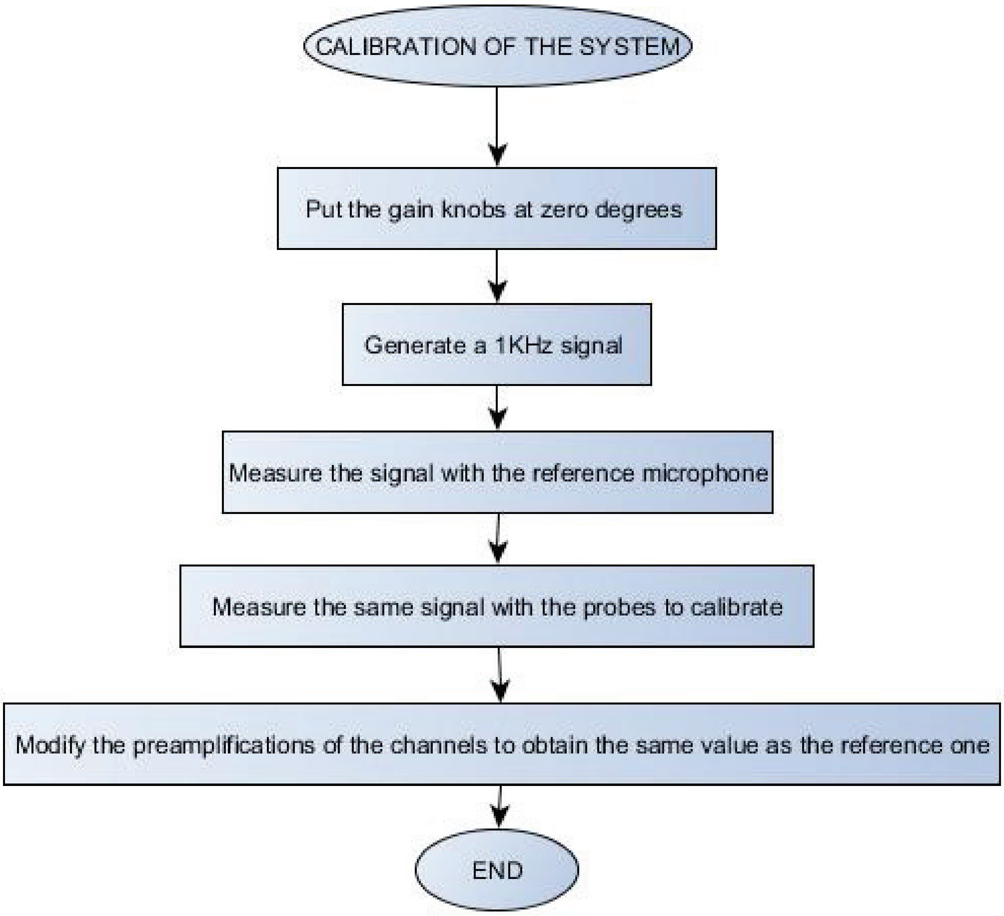

Fig. 4.3 Scheme for the calibration of the system, which consists in the MOTU sound card, the reference microphone and the probe to calibrate.

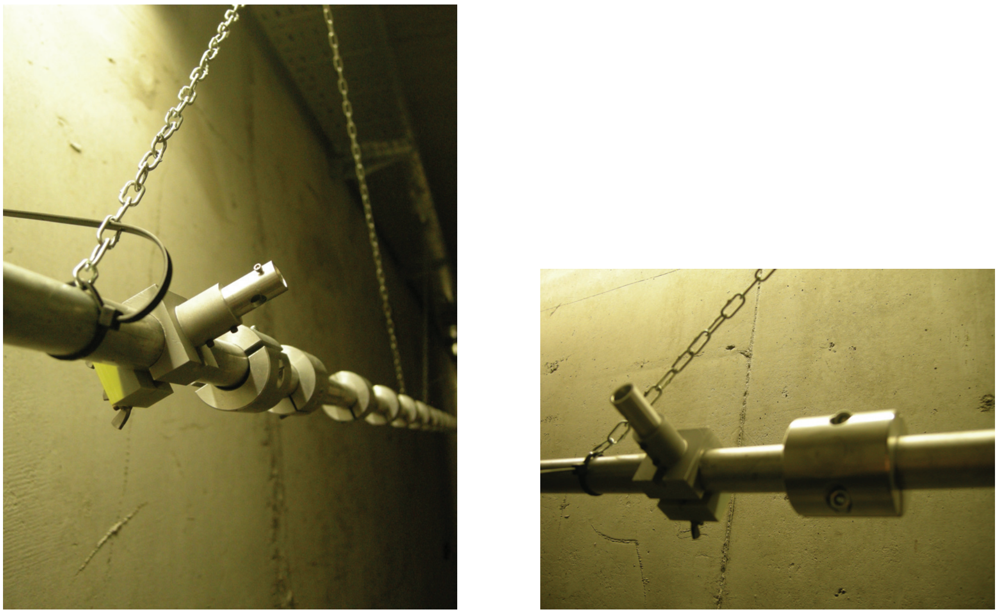

Fig. 4.4 The progressive plane wave tube inside Larix, which has been modified in order to insert the probe at different points through a series of holes: on the right the last hole, 10,8 m far from the source, used for the calibration.

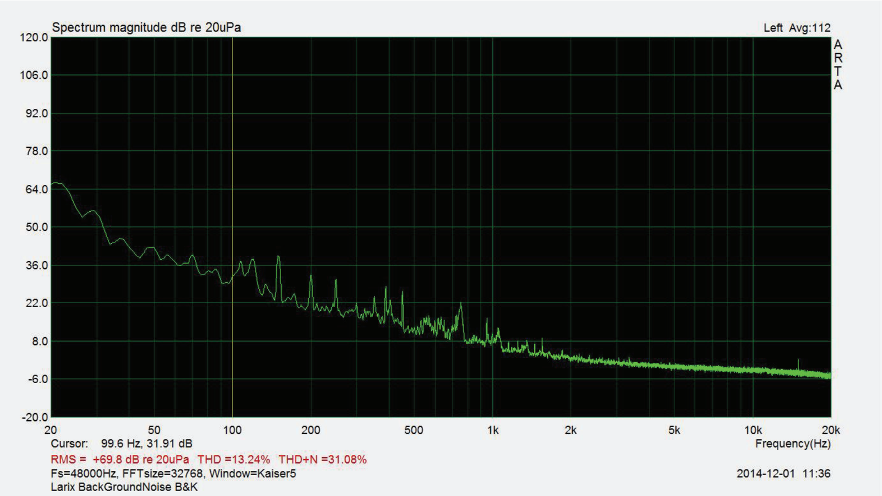

Fig. 4.5 Background noise measured inside larix tube with Bruel & Kjaer microphone.

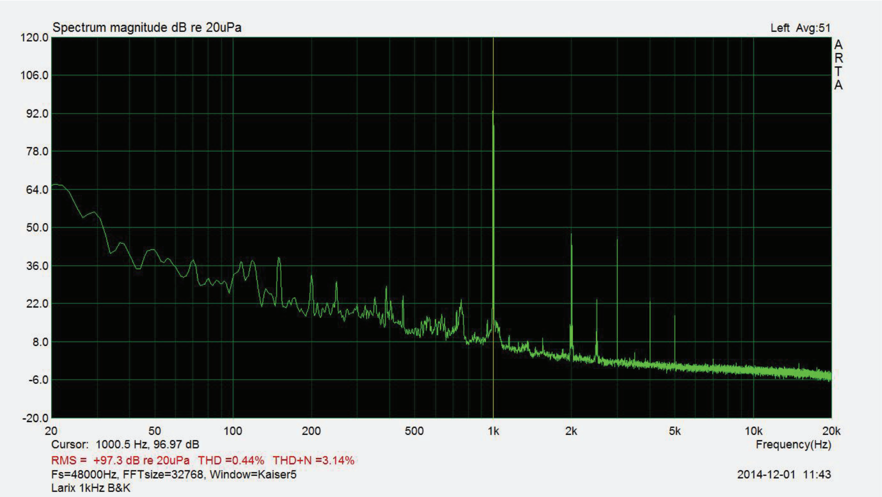

Fig. 4.6 1 KHz sine signal measured with Bruel& inside larix tube.

4.7). In particular figure 4.7b highlights the importance of insulating the probe from the tube, through insulating tape: the signal measured before this procedure (in yellow) shows an high background noise and many spikes.

The new values of preamplification are shown in figure 4.8.

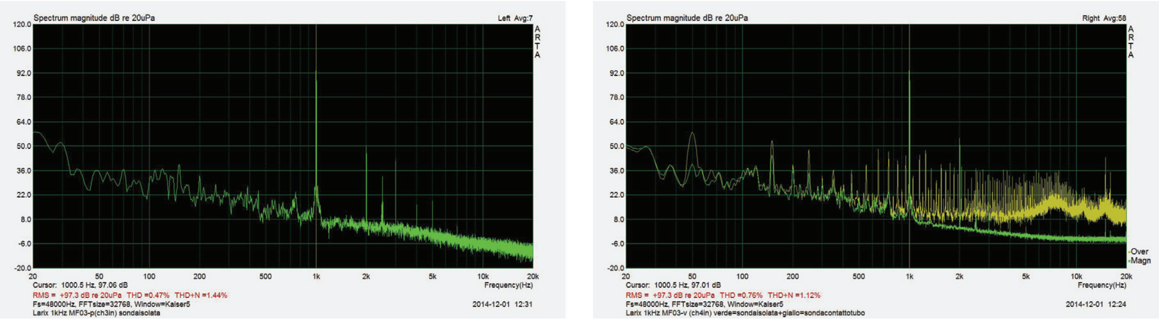

(a) Pressure channel.

(b) Velocity channel.

Fig. 4.7 Calibration of Microflown probe in Larix: on the left the pressure signal, on the right the velocity. In yellow the measures of the velocity channel with the probe not isolated from the tube

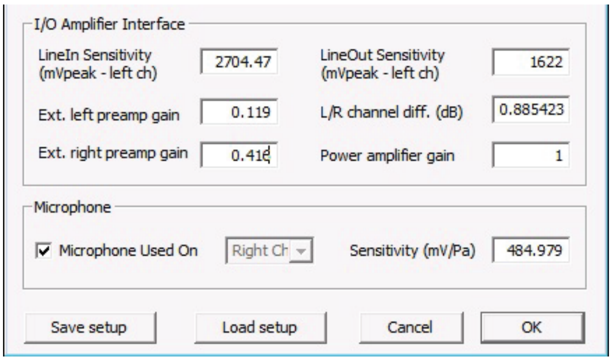

LineIn Sensitivity (mVpeak - left ch): 2704.47
LineOut Sensitivity (mVpeak - left ch): 1622
Ext. left preamp gain: 0.119
L/R channel diff. (dB): 0.885423
Ext. right preamp gain: 0.416
Power amplifier gain: 1
☑ Microphone Used On: Right Ch
Sensitivity (mV/Pa): 484.979

Fig. 4.8 The new values of preamplification found comparing the Microflown probe to the reference microphone at 1 KHz.

Now that the Microflown probe is calibrated at 1 KHz, it’s possible to measure the impedance $Z_0(\omega)$ as a function of frequency from 20 Hz to 10 KHz inside the tube. Such curve will be the wide band compensation to be used for any impedance measurement with the Microflown probe (see fig. 4.9).

In fact introducing the correction curve shown in figure 4.9 as a compensation to the ARTA software, the impedance measured in the Larix tube will be displayed as a flat curve approximating the zero value at each frequency. This is clearly a correct readout given that in the Larix tube a plane progressive wave field is generated having a known a-priori impedance equal to ρc for any frequency.

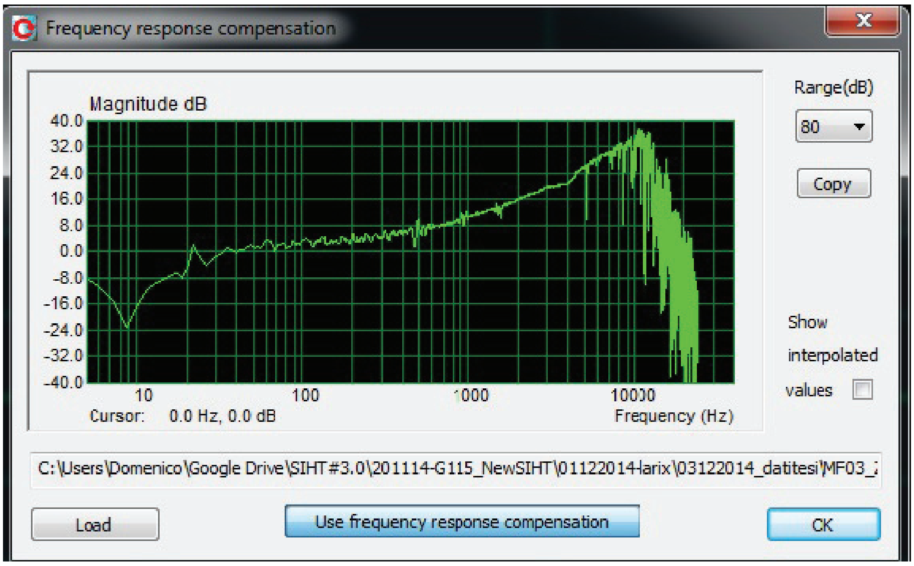

Cursor: 0.0 Hz, 0.0 dB

C:\Users\Domenico\Google Drive\SIHT#3.0\201114-G115_NewSIHT\01122014-larix\03122014_datitesi\MF03_

Fig. 4.9 Impedance measured inside Larix with the Microflown probe calibrated only at 1 KHz, but not at wide band.

4.1.3 Comparison calibration of SIHT in the laboratory

After the pre-calibration of the Microflown pressure-velocity probe inside the Larix tube, the further step consists in the proper comparison calibration: a new procedure devised to calibrate any p-v probe even at the protypical stage and in particular, in our case, the SIHT prototype ♯ 3. In fact because of the particular shape of the probe (see Fig. 3.11), the calibration inside the Larix tube is not feasible. The solution is to choose a probe similar to the prototype as a reference one; in this case we have put the Microflown p-v probe inside an horn of the same dimensions as the SIHT prototype (see Fig. 3.28).

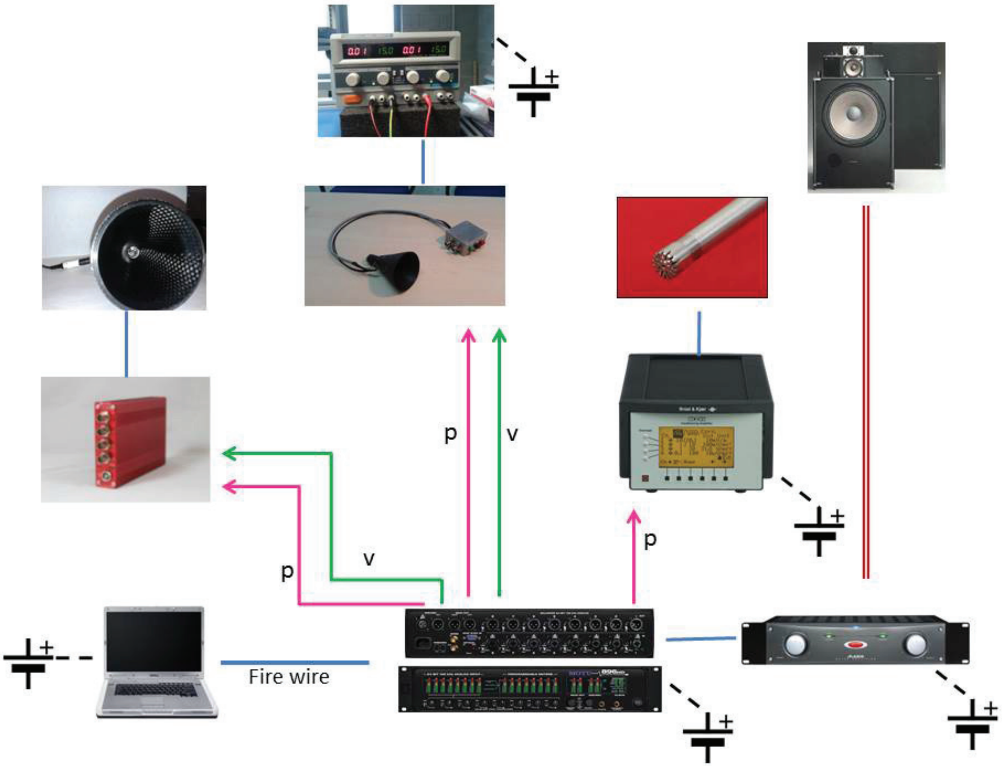

Fig. 4.10 Set up for the comparison calibration in the laboratory.

The scheme in figure 4.10 shows the laboratory setup: the electroacoustic measurement chain is based on a portable personal computer (PC) equipped with a MOTU I/O external board and a power amplifier for signals driving the loudspeaker (a Technics SB-7000). Three probes are connected to the MOTU sound card: the Bruel & Kjaer 1/8 inch microphone, the Microflown match size p-v probe inside the horn, and the SIHT prototype ♯ 3. As a precaution, in order to reduce the ambient noise, the loudspeaker is placed inside a 1 m^3 phono-insulating chamber, and the probes are mounted on a tripod facing the loudspeaker (see fig. 4.11). The first step is to measure a signal, in our case a 1 KHz sine, with the

Bruel & Kjaer microphone, and to set the preamplification factor of the channel relative to the pressure measured by Microflown inside the horn in order to measure exactly the same value. The same thing has to be done by measuring the signal through the SIHT pressure sensor. Thereafter the Microflown probe will become the reference one: we measure the spectrum magnitude (dB rel. to 20 μPa) of white noise in third octave bands and we adjust the preamplification factors both for pressure and velocity in order to measure respectively the same value at 1 KHz with the two probes. Finally, it's possible to measure the impedance with Microflown calibrated and compensated inside Larix: this is the target curve for SIHT impedance, so it will be necessary to create the compensation for the SIHT probe (the probe under calibration) both in magnitude and phase.

In order to have more precise results, it's better to put the probes in the same position and do the measurements in two consecutive moments.

Fig. 4.11 Tripod holding the probes for comparison calibration.

4.1.4 Results

The correction curve Γ is calculated as the difference from the impedance magnitude measured with the SIHT probe and the reference one, mounting the Microflown p-v probe (see Fig. 4.11), and all the measures are expressed in dB. Such difference may be easily calculated using for instance the Sigview software, and is shown in figure 4.12, or post-processed by a dedicated Matlab routine. The application of such curve to the next measurement using the

SIHT probe will supply calibrated measures with reference to the pre-calibrated Microflown prototype.

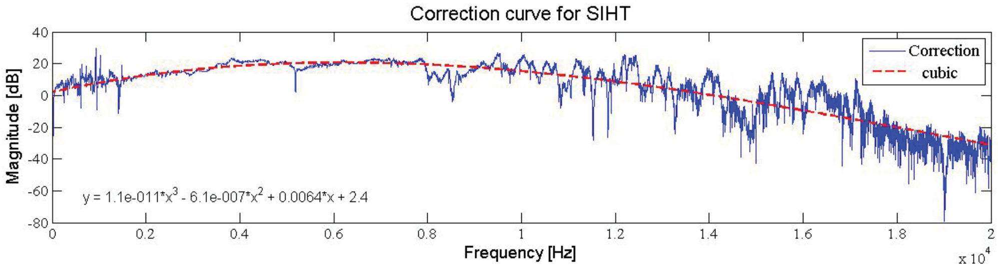

Fig. 4.12 Compensation curve obtained as the difference between the impedance of the SIHT probe and the Microflown reference prototype.

The correction of the phase of the SIHT probe consists in substituting the raw phase measured with the uncalibrated probe (Fig. 4.13) with the phase measured with the pre-calibrated Microflown probe (Fig. 4.14).

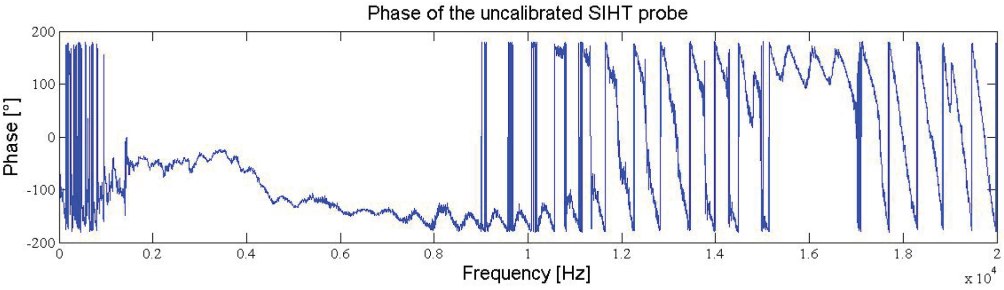

Fig. 4.13 Phase of the uncorrected SIHT probe.

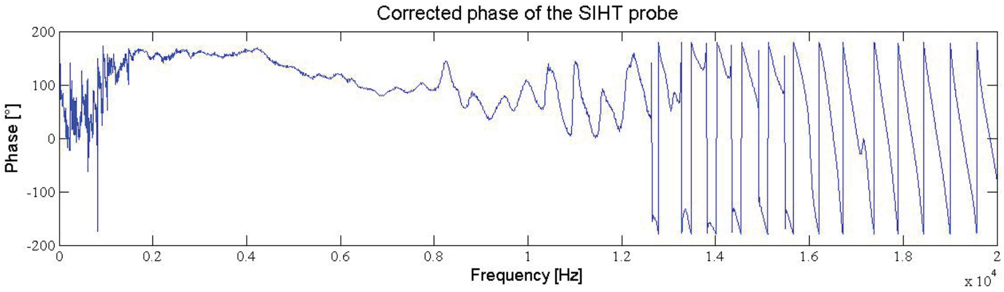

Fig. 4.14 Phase of the compensated SIHT probe.

Figure 4.15 shows the impedance of the reference probe (Microflown) compensated with the impedance measured inside tha Larix laboratory: in yellow the magnitude of the uncalibrated SIHT impedance, in green the compensated Microflown curve, in white the phase and in red the coherence. In particular this last curve gives a linearity check between the pressure and velocity signals, having characterised the reference field as a progressive plane wave [19].

The coherence is defined as:

$$\gamma(\omega) = \sqrt{\frac{|S_{PV}(\omega)|^2}{S_{PP}(\omega)S_{VV}(\omega)}} \tag{4.1}$$

where $S_{PV}(\omega)$is the cross-spectrum of pressure and velocity signals and $S_{PP}(\omega)$, $S_{VV}(\omega)$ are the respective autospectra. The more this function is similar to 1, the greater linearity between pressure and velocity is present.

In this case we can appreciate a good linearity in the Microflown probe compensated.

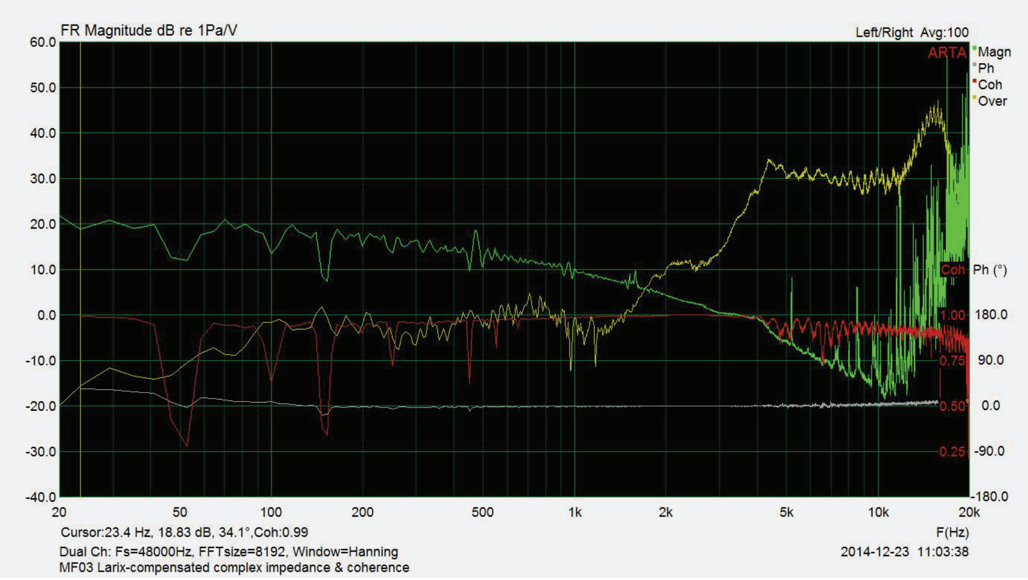

Fig. 4.15 Larix compensated impedance of the reference probe (Microflown): in green the compensated magnitude, in white the phase and in red the coherence. In yellow the uncalibrated magnitude of the SIHT probe.

Figure 4.16 represents the raw impedance and the coherence measured with the SIHT prototype inside the laboratory. This figure has to be compared to the next one, Fig. 4.17, which resumes the compensated impedance of SIHT (magnitude in green and phase in white), compared with the Microflown reference probe. The difference between the magnitudes is shown in light yellow: the values near to zero highlight the perfect compensation of the SIHT impedance, so revealing the effectiveness of the comparison calibration method.

Figures from 4.18 to 4.21 show the results of the comparison calibration of the SIHT prototype with respect to the probe mounting the Microflown and taken as reference one. In this case the measures have been taken inside the Laboratory, with the caution of placing

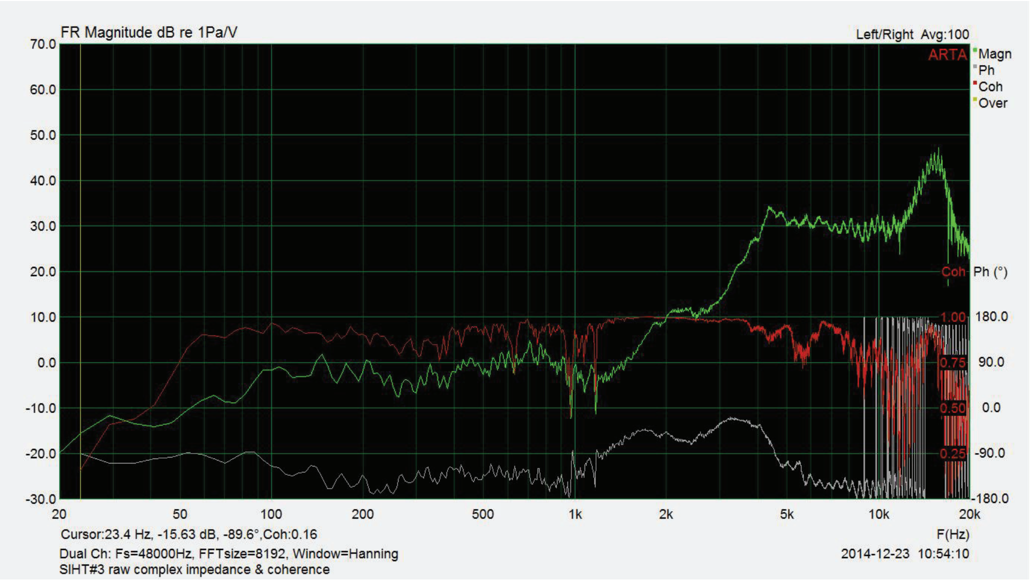

Fig. 4.16 Impedance (magnitude in green, phase in white) and coherence in red of the SIHT prototype calculated from raw data inside the laboratory.

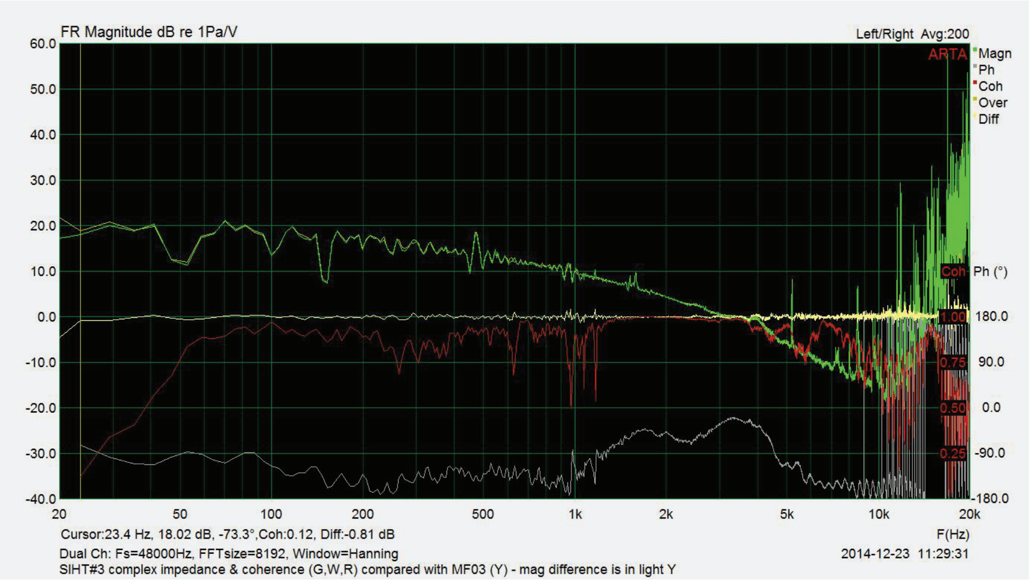

Fig. 4.17 SIHT ♯ 3 compensated impedance (magnitude in green and phase in white) compared with the Microflown reference probe (yellow). The difference between magnitudes is in light yellow.

the probes exactly at the same point during the two successive measures. The first plot is calculated following equation 2.45 as the ratio between the admittance measured with the SIHT probe and the one measured with Microflown. The data have been smoothed using the Sigview software, and then they are post-processed using Matlab. We selected the values relative to the centre of the octave bands and finally the fitting of the curve has been calculated. By applying the Γ curve to the impedance measured with the SIHT probe, it's possible to derive the calibrated values. The phase of the Γ shows constant values up to 1 KHz, so highlighting a good behaviour of the probe within such values.

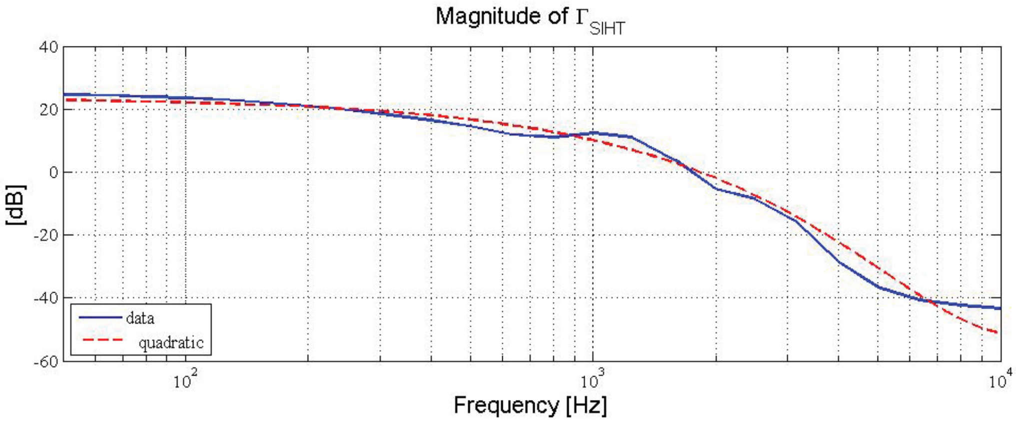

Fig. 4.18 Magnitude of Γ of the SIHT prototype (blue, continuous line) and quadratic fitting (red, dashed line).

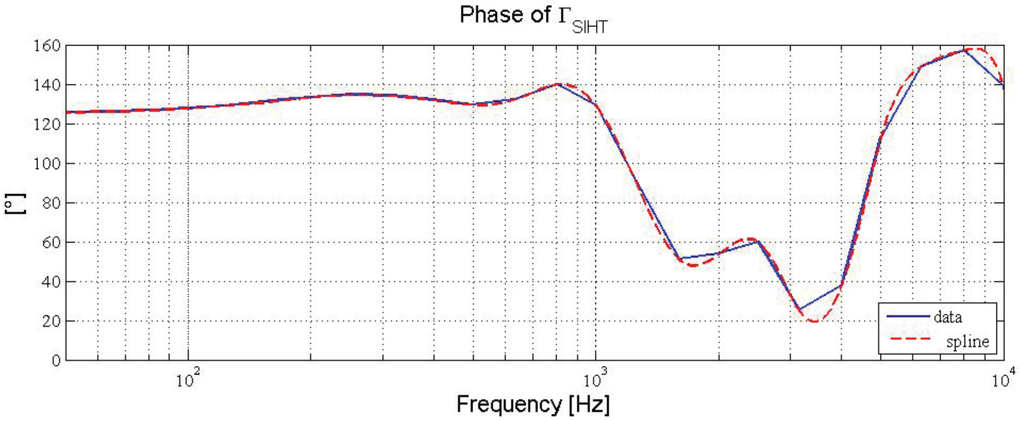

Fig. 4.19 Phase of Γ of the SIHT prototype (blue, continuous line) and spline fitting (red, dashed line).

The sensitivity of the pressure channel S_p (Fig. 4.20), calculated as the ratio between the pressure measured with the probe under test and the pressure measured with the reference probe, confirms the goodness of the SIHT probe in particular for frequencies lower than 1

KHz. The last figure shows the sensitivity of the velocity channel calculated as in equation 2.48, and the relative fitting corresponding to a 5^{th} degree polynomial.

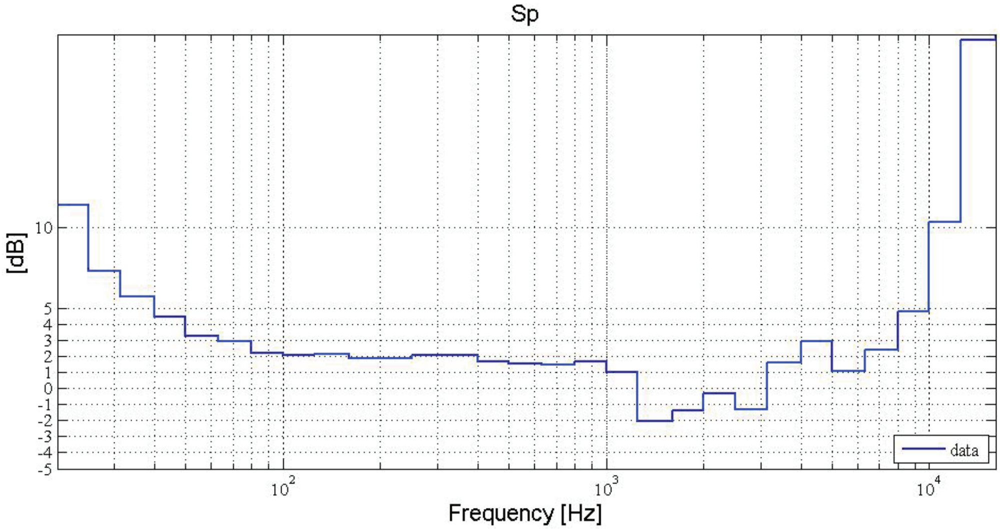

Fig. 4.20 Sensitivity of the pressure channel (blue, continuous line).

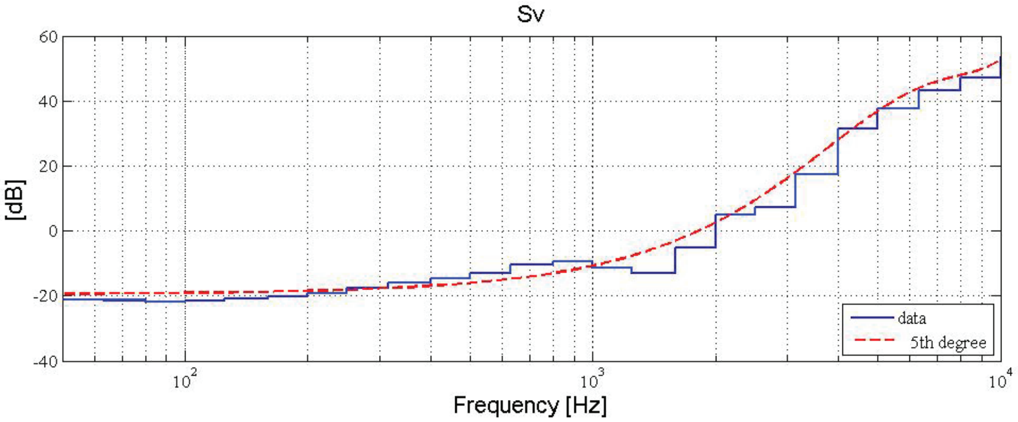

Fig. 4.21 Sensitivity of the velocity channel (blue, continuous line) and 5^{th} degree fitting (red, dashed line).

Chapter 5

Case studies

This chapter resumes some of the case-studies realised with the prototypes mounting the Microflown p-v probe, with the aim of arranging possible applications of the SIHT prototype.

5.1 Tympanometry

One of the first applications of the SIHT probe is in the audiometric field. Tympanometry is a technique which has been used in audiometry since 1970, and contributes, in battery with other tests, in finding the presence of pathologies in the middle ear and in the tympanic membrane, by measuring the acoutic admittance of the external ear [33],[34].

Collected data are resumed as plots, called tympanograms, that show the acoustic admittance as a function of the variation of static pressure ΔP between the medium and the external ear. Such pressure difference is obtained by sealing and pumping the air volume inside the ear canal, in a range of [-600, +400] daPa and with a stimulus of 226 Hz. Figure 5.1 shows a standard tympanometric probe sealed to the ear canal through a rubber tip.

The obtained values of admittance are measured in mmho on a pre-calibrated scale over a 2 cc rigid volume filled with air in standard pressure conditions. The measure of the admittance is so reduced to an equivalent volume measure starting from the hypothesis of the validity of compliance: as a consequence of such a condition the tympanogram could also be expressed in terms of cc values of equivalent acoustic volume instead of mmho's.

It is known from literature [33] that a differential in pressure of +200 daPa is sufficient to stretch and move the tympanic membrane to the medium ear and then the admittance is 0. In these conditions in fact the only energy absorbance depends on the compliance of the air included in the external ear duct. That's why the admittance in audiometry is always referred to the level measured at ΔP = +200 daPa. From the admittance is possible to obtain

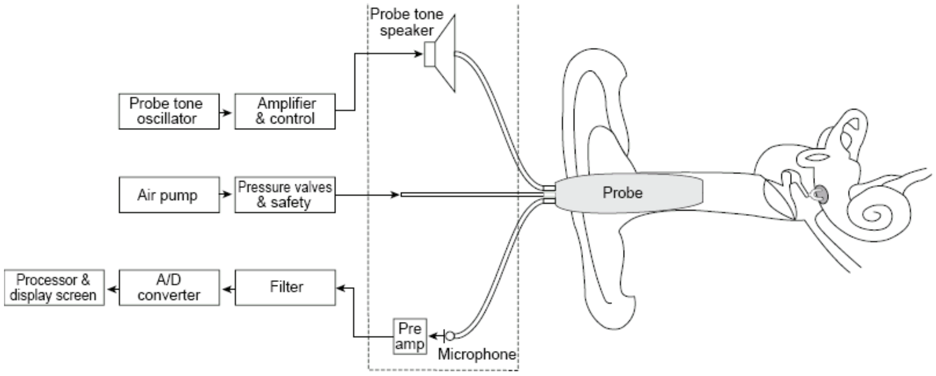

Fig. 5.1 Scheme of a standard tympanometric probe. On the top the miniature speaker that generates the 226 Hz stimulus, on the bottom the pressure microphone that registers the response and in the center the air pump to change the pressure in the external ear canal.

the values of the effective air volume of the ear duct: normal values are included between 0.3 and 0.9 cc for children and between 1.3 and 1.5 cc for adults.

The traditional tympanometric test can be completed by measuring the admittance with other single frequency stimuli at 678, 800 and 1000 Hz (a technique called "multi-tone" tympanometry). Such measures can be useful to detect eventual absorbances in the middle ear, but to this day the results are still difficult to interpret, therefore there's a diffused interest in new techniques which use wide band measurements instead of single tones [35].

The recent development of p-v probes has represented the possibility to improve the audiometric tests by directly measuring the immittance of the ear [36], [37]. Such probes represent a new approach in measuring the characteristic of the ear and are the key to discover a new horizon in energetic audiometry, but the first step is to identify the relationship between the results obtained with the two techniques, the traditional and the impedentiometric one.

A first set of audiometric tests with a p-v probe has been made directly using a Microflown p-v match size probe facing the ear of the volunteer (Fig. 5.2): the results are well described in [3] and in [38]. The ideal model of p-v fields inside the ear canal can be described by considering the velocity **v**(x,y,z,t) depending on just one direction, because of the canal ear structure. This consideration simplifies the measures: only 2 signals (p,v) have to be measured in order to perform aural immittance measurements.

The frequency dependent specific acoustic immittance of sound inside the ear canal is obtained by:

$$Y(x,\omega) := \frac{F(v)}{F(p)} = G(\omega) + iB(\omega) = |Y(\omega)|e^{i\Delta\omega(\omega)} \tag{5.1}$$

where |Y| is the magnitude of the admittance, depending on both the acoustic conductance G and the susceptance B, and Δ is the phase lag of the pressure signal with respect to the velocity.

The author in [35] has introduced a new quantity, called Energy Absorbance, expressed as:

$$EA = 1 - \frac{1-\eta}{1+\eta} \tag{5.2}$$

where η is the energy conductance, that is the real part of the energy current immittance $\overline{\sigma}$:

$$\overline{\sigma} = \eta + i\mu \tag{5.3}$$

Equations 5.1, 5.2 and 5.3 all represent directly measurable quantities with a calibrated p-v probe.

One of the results during the first test is shown in figure 5.3: the plot represents the energy absorbance in 1/12 octave bands in the range [20- 9000 Hz] (left scale) and its overall value for a normal ear (right scale).

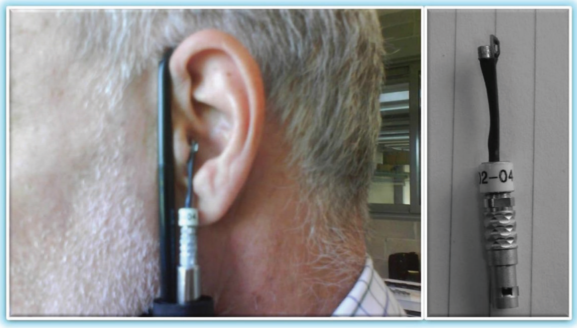

Fig. 5.2 Set up of the first tympanometric test with a p-v commercial microprobe.

Such a method has some disadvantages: the probes used for the tests are very delicate and easy to break and the external stimulus generates a bad SNR. In order to solve these problems, we have realised a first prototype of p-v tympanometric probe starting from a standard one, extensively described in section 3.3.

The Microflown p-v sensor has been inserted in a standard probe; a common in-ear headphone has been used as stimulus at the rear of the probe, while its front was terminated with a rubber tip in order to easily plug the probe into the ear canal entrance (Fig. 5.7). Data acquisition and analysis were carried out by a National Instruments I/O interface (NI USB-4431) and a laptop running Matlab routines. We used the tympanometric prototype

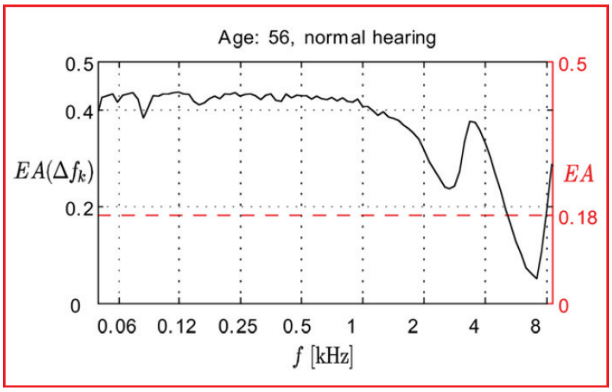

Fig. 5.3 1/12 octave band distribution of energy absorbance [3].

to directly record the pressure and velocity responses to a wide frequency range stimulus, a swept sine of initial frequency of 20 Hz and final frequency of 8000 Hz. The p-v responses are then convoluted with the inverse stimulus so obtaining the pressure and velocity impulse responses, from which other quantities such as the immittance (eq. 5.1), energy absorbance (eq. 5.2) and immittance (eq. 5.3) are derived.

In order to have comparable measures it's necessary to establish a baseline, like in standard tympanometry. This task has been accomplished by measuring the acoustic admittance with the prototype plugged up. The next measures will be evaluated with respect to such value, using the expression:

$$L_{|Y|} = 20log\frac{|Y(\omega)|}{|Y(\omega)|_{plugged}}dB \tag{5.4}$$

with $|Y(\omega)|_{Plugged}$ the reference admittance.

Figures 5.4 and 5.5 show the graph of $|Y(\omega)|_{Plugged}$ and of $|Y(\omega|$ measured in a 2 cc rigid volume, where to the 226 Hz frequency corresponds a value of -6.7 dB.

The comparison of the two tympanometric tests have been done during a unique set of measures on a population of 13 volunteers, aged between 20 and 30 years old, with normal hearing capacity, that first have undergone a traditional test with an Amplaid model 728 Tympanometer (see figure 5.6), and secondly to the wide band tympanometry using the p-v prototype (figure 5.7). Such research has been conducted in collaboration with Sant'Anna Hospital in Ferrara thanks to the help of Silvano Prosser MD.

The obtained results are reported in figure 5.8. It's evident how the 26 plots (13 for right ears, and 13 for left ears), converge in correspondence of the frequency of 226 Hz, also used for single tone traditional tympanometry. Table 5.1 resumes the comparison of $L_{|Y|}$ obtained with p-v tympanometry, with the equivalent volume EV and peak compensated static acoustic

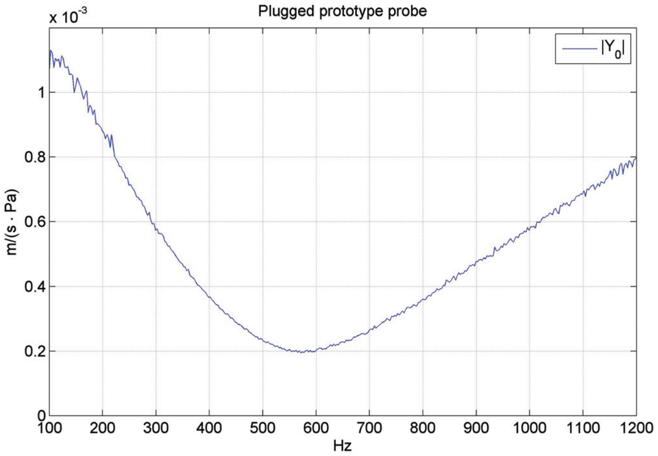

Fig. 5.4 Specific admittance measured when the probe is plugged up [37].

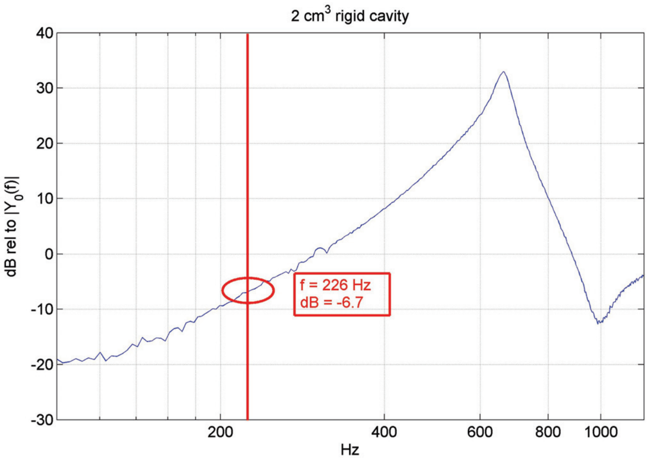

Fig. 5.5 Admittance of a 2 cc volume.

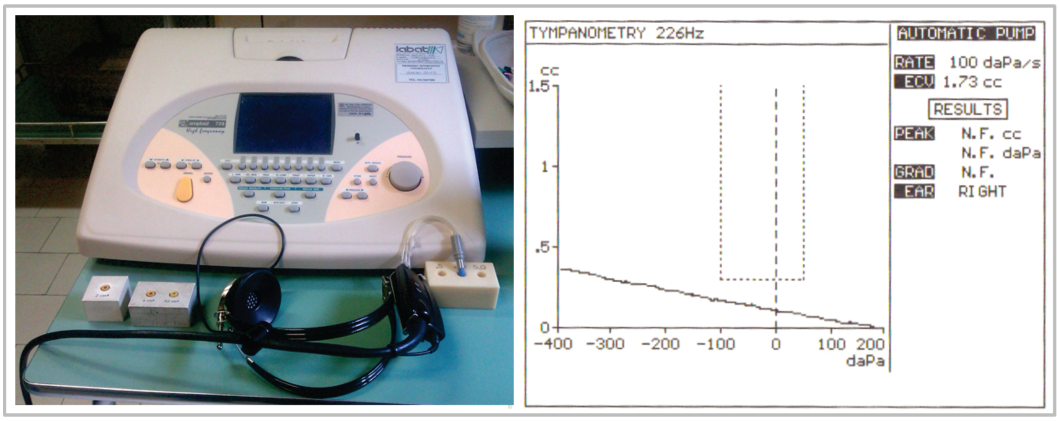
TYMPANOMETRY 226Hz

AUTOMATIC PUMP
RATE 100 daPa/s
ECV 1.73 cc

RESULTS
PEAK N.F. cc
N.F. daPa
GRAD N.F.
EAR RIGHT

Fig. 5.6 Photo of a standard clinic tympanometer and an example of "type B" tympanogram measured on a 2 cc cavity.

Fig. 5.7 The prototype probe for p-v tympanometry is fitted inside the ear canal at normal pressure conditions.

admittance Y_{peak} measured with the traditional one. Such values are also resumed in figures 5.9 and 5.10: the regression shows a good agreement between the results of the two tests.

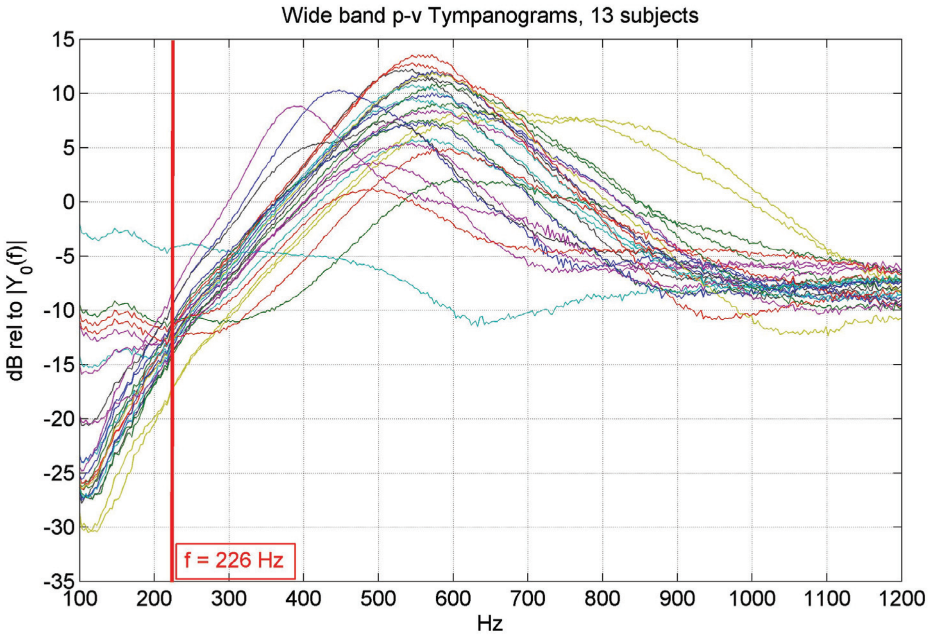

Fig. 5.8 Specific admittance measured with the p-v tympanometric prototype. The plot shows the results of the tests on 13 subjects for a total of 26 tympanograms.

Table 5.1 Measured immittance levels $L_{|Y|}$ obtained with p-v tympanometric probe, peak condensated static acoustic admittance Y_{peak} and equivalent volume EV measured with the standard system.

	1	**2**	**3**	**4**	**5**	**6**	**7**	**8**	**9**	**10**	**11**	**12**	**13**
Ly (dB)	-13.2	-13.8	-14.0	-9.4	-11.9	-11.3	-12.8	-12.5	-12.2	-4.2	-17.0	-8.2	-12.7
Y_{peak}(cc)	0.61	1.02	0.62	0.47	1.04	1.04	/	1.00	2.86	2.07	0.23	0.26	0.76
EC (cc)	1.00	1.08	0.71	0.63	1.16	1.09	/	0.85	0.75	0.62	0.36	0.39	1.13
14	**15**	**16**	**17**	**18**	**19**	**20**	**21**	**22**	**23**	**24**	**25**	**26**	**Mean**
-12.7	-12.7	-12.4	-9.3	-10.9	-11.6	-13.7	-11.9	-11.3	-11.3	-13	-13.6	-17.1	-12±2.5
0.70	1.23	1.70	1.09	0.86	0.82	0.76	0.72	0.66	0.89	0.73	1.09	1.051	1.1±0.7
0.94	1.23	1.70	1.09	0.86	0.82	0.76	0.72	0.66	0.89	0.73	1.09	1.051	0.9±0.3

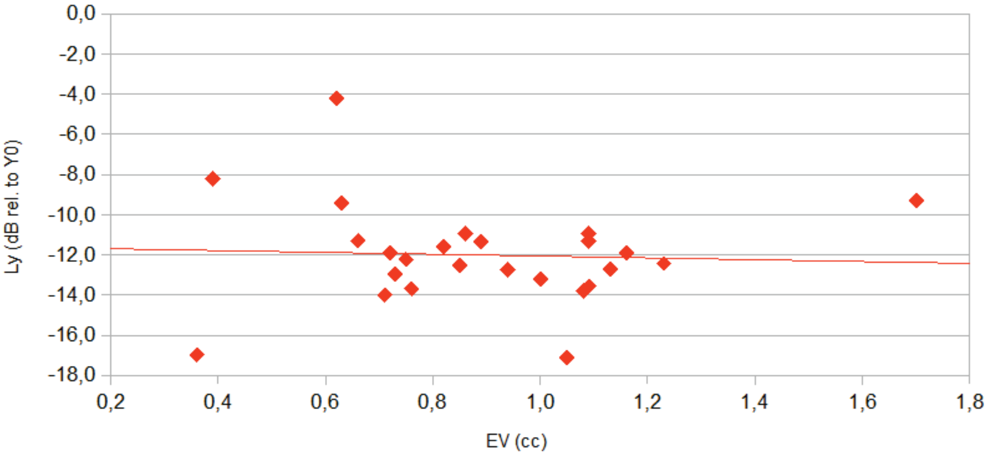

Fig. 5.9 Summary of the results of the specific admittance collected from the 13 volunteers vs the equivalent volumes in cc measured with a traditional tympanometer.

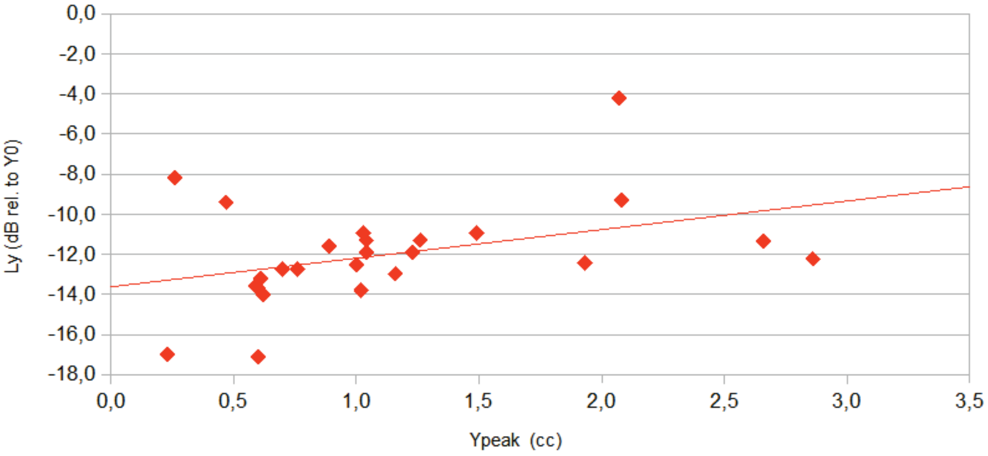

Fig. 5.10 Summary of the results of the specific admittance collected from the 13 volunteers vs the peak compensated static acoustic admittance.

A clarification is now necessary: the two procedures, because of the different measuring principles, produces two distinct physical quantities: on one hand the admittance Y of standard tympanometry is the ratio between the volume velocity and the acoustic pressure, while the specific admittance Y$_s$ measured with our new method is the ratio between the air particle velocity and the pressure. That is:

$$Y = \frac{V}{p} = \frac{Sv}{p} \qquad \left[\frac{cm^5}{dyne \cdot s} =: mmho\right] \tag{5.5}$$

and

$$Y_s = \frac{v}{p} \qquad \left[\frac{m}{Pa \cdot s}\right] \tag{5.6}$$

So the two expressions are comparable except for a factor proportional to a surface, that is the effective area of acoustic energy absorbance.

Table 5.2 resumes the data obtained with the two procedures, while in table 5.3 we see the derived results of equivalent area of absorbance and the diameter of the duct-tympanum system.

Table 5.2 Admittance and specific admittance measures of the patients

	Right ear		**Left ear**	
	Y (ΔP = 0 daPa)	**Y$_s$**	**Y (ΔP = 0 daPa)**	**Y$_s$**
S-01	1.60e+00	1.74e-04	1.89e+00	1.90e-04
S-02	1.08e+00	1.58e-04	8.83e-01	2.26e-04
S-03	2.03e+00	2.02e-04	1.89e+00	2.09e-04
S-04	n.d.	1.82e-04	1.46e+00	2.02e-04
S-05	2.82e+00	1.94e-04	1.90e+00	2.15e-04
S-06	4.98e-01	1.12e-04	6.30e-01	1.10e-04
S-07	1.76e+00	1.83e-04	1.46e+00	1.63e-04
S-08	2.93e+00	2.69e-04	3.46e+00	1.96e-04
S-09	2.10e+00	2.16e-04	1.65e+00	3.21e-04
S-10	1.38e+00	1.88e-04	1.12e+00	3.32e-04
S-11	1.15e+01	4.90e-04	1.21e+00	7.12e-05
S-12	3.32e+00	3.09e-04	1.82e+00	2.08e-04
S-13	4.16e-01	1.83e-04	1.56e+00	5.93e-04

The application of the p-v prototype to audiological tests represents an important contribution to the understanding of the ear. The advantages are the possibility of a new wide range tympanometry that doesn’t require the pressure differential inside the ear duct, so making the tests less invasive, especially for the younger patients. Another advantage lies in the possibility of directly measuring pressure and velocity of the ear with a single measure: in

Table 5.3 Equivalent area and diameter

	Right ear		**Left ear**	
	S [cm^2]	**D [cm]**	**S [cm^2]**	**D [cm]**
S-01	9.19e-01	1.18e+00	9.97e-01	1.13e+00
S-02	6.86e-01	9.35e-01	3.91e-01	7.06e-01
S-03	1.00e+00	1.13e+00	9.03e-01	1.07e+00
S-04	n.d.	n.d.	7.25e-01	9.61e-01
S-05	1.45e+00	1.36e+00	8.85e-01	1.06e+00
S-06	4.43e-01	7.52e-01	5.70e-01	8.52e-01
S-07	9.59e-01	1.11e+00	8.94e-01	1.07e+00
S-08	1.09e+00	1.18e+00	1.76e+00	1.50e+00
S-09	9.73e-01	1.11e+00	5.14e-01	8.09e-01
S-10	7.33e-01	9.66e-01	3.36e-01	6.54e-01
S-11	2.35e+00	1.73e+00	1.70e+00	1.47e+00
S-12	1.07e+00	1.17e+00	8.75e-01	1.06e+00
S-13	2.27e-01	5.38e-01	2.62e-01	5.78e-01

this way new physical quantities can be obtained, such as the energetic absorbance and the immittance.

5.2 Monitoring of the filling of pharmaceutical capsules

Another important application of the tympanometric prototype regards the condition monitoring in pharmaceutical industry and has been presented in [39]. In particular we studied the filling of hard gelatine capsule, trying to detect their content through acoustic measurements.

The weighting method of capsules is quite a big issue for pharmaceutical industries, because it's not possible to directly measure each single capsule. The capsules are filled by a packing machine with a specified amount of drug: the capacity of the machine is of 5-10 pieces per second, therefore the amount of medicine inside each capsule may deviate from target specification. An error in drug dosing could be toxic or dangerous. At present it's not possible to control the weight of each capsule, but some of them are sampled from a batch of production and then mechanically weighed. However, it would be necessary to weigh each single capsule in order to eliminate over or under dosages.

In literature just few alternative methods of weighing are proposed: a method based on the travelling time of the capsule within a vertical tube for a given pressure difference between the ends is proposed in [40], but it's still under research.

The p-v micro-probe descripted in section 3.3 was mounted on a rack of a capsule filling machine made by IMA Pharma (Fig. 5.11), and used to measure the p-v impulse responses of each capsule under test. We had 15 different objects, varying both in quantity and aggregates of the contained drug (powder, pellets, microtablets). Dosages and kind of filling inside the different capsules are given in table 5.4.

Fig. 5.11 Experimental set up: the tympanometric prototype on the left, a particular of the rack of a capsule filling machine on the right.

The results here reported are a mean of many impulse response measurements. The use of a p-v probe guarantees the collection of different sound energetics quantities, but the most representative are the specific and energetic admittance $|Y(\omega)|$ and σ, with particular reference to its peak frequency, here called f_{peak}, and the magnitude of the energetic parameter

Table 5.4 Capsule number, dosing and kind of aggregate

Capsule	**Dosing (mg)**	**Aggregate**
1	2.3	Micro-dosage
2	5.3	-
3	10.5	-
4	14.4	-
5	20.2	-
6	25.5	-
7	124.2	Macro-dosage
8	176.3	-
9	227.5	-
10	177.4	Pellets
11	228.2	-
12	281.4	-
13	62.3	Micro-tablets
14	113.4	-
15	165.4	-

called *normalised admittance* σ. We recall such quantities previously defined:

$$Y(\omega) = \frac{\mathscr{F}(v)}{\mathscr{F}(p)} \tag{5.7}$$

$$|\sigma| = \frac{1}{2} z_0 \sqrt{\langle p^2 \rangle \langle v^2 \rangle} \langle p^2 \rangle + z_0^2 \langle v^2 \rangle \tag{5.8}$$

The specific admittance Y(ω) has been measured through the sine-sweep technique. Figures 5.12 to 5.15 show the magnitude |Y(ω)| for capsules filled with the different kinds of aggregates. It can be noticed that the peak frequencies (f_{peak}) of admittance become more distinguishable when passing from micro-dosage powders (a few mg, Fig. 5.12) to micro-tablets (about 50 mg, Fig. 5.15).

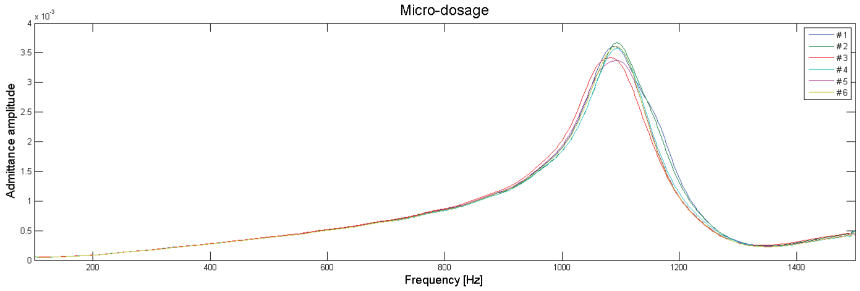

Fig. 5.12 |Y(ω)| calculated for micro-dosage.

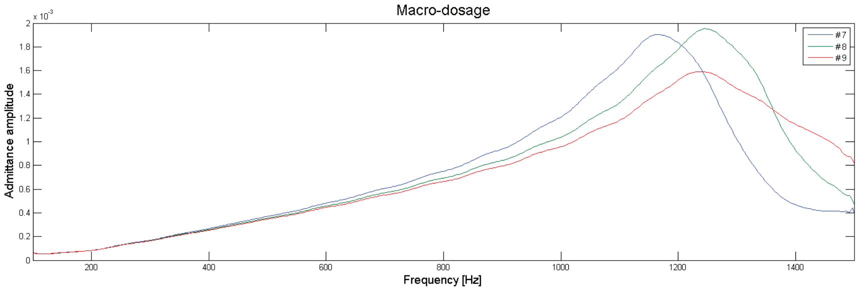

Fig. 5.13 |Y(ω)| calculated for macro-dosage.

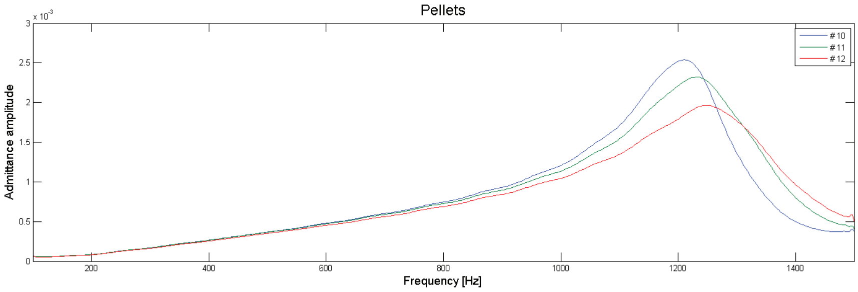

Fig. 5.14 |Y(ω)| calculated for pellets.

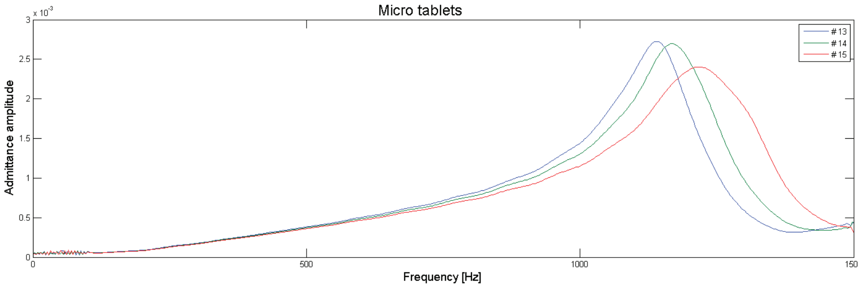

Fig. 5.15 |Y(ω)| calculated for tablets.

The trend of f_{peak} is resumed in the upper plots from figures 5.16 to 5.19, while the bottom plots show the stationary values of the energetic admittance magnitude. The trend clearly confirmed a correspondence between increments of f_{peak} and decrements of $|\sigma|$ as a function of dosage.

The tests revealed that the acoustic approach is still not useful for detecting lower dosages, but it could be optimised for pellets and micro-tablets dosages.

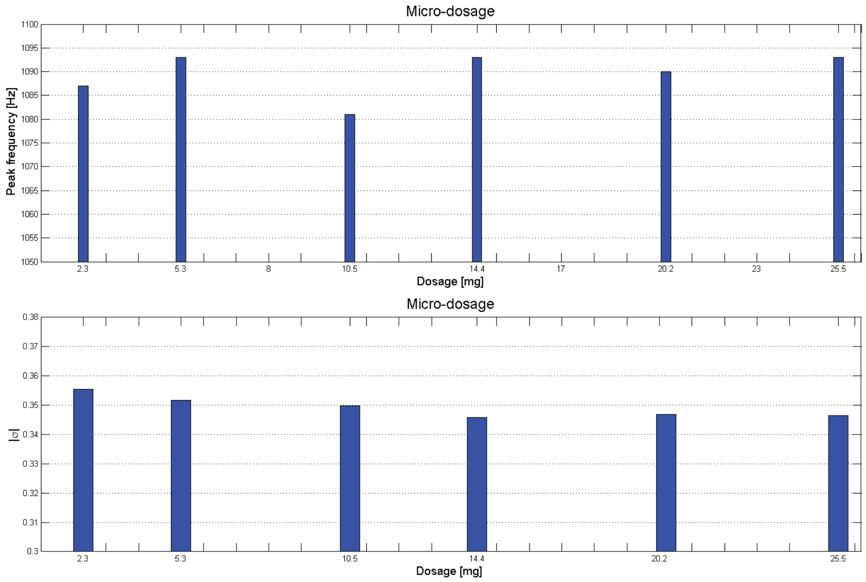

Fig. 5.16 Peak frequency of $|Y(\omega)|$ (top) and values of $|\sigma|$ for the micro dosage differences (bottom).

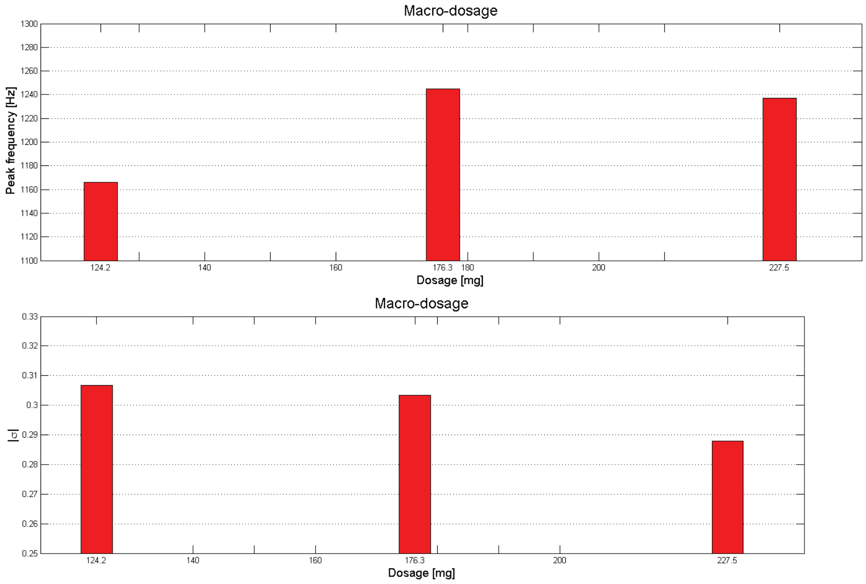

Fig. 5.17 Peak frequency of $|Y(\omega)|$ (top) and values of $|\sigma|$ for the macro dosage differences (bottom).

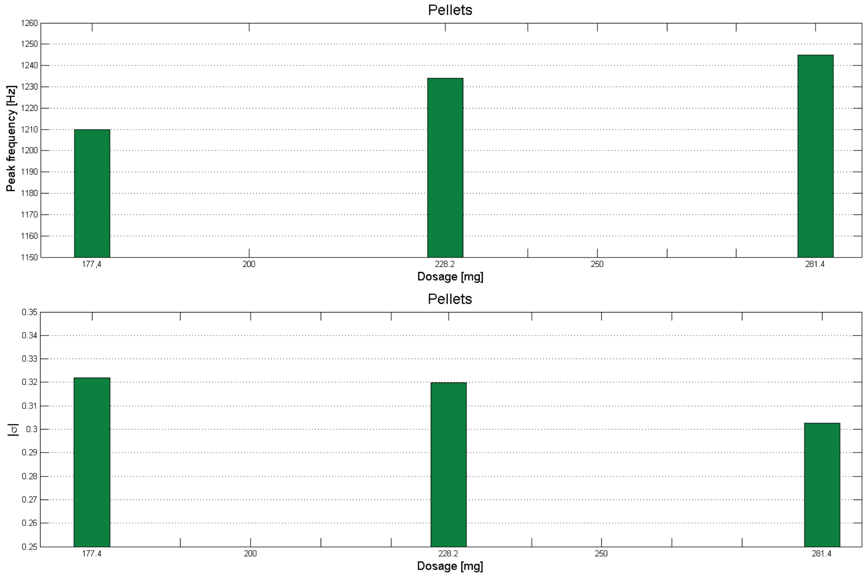

Fig. 5.18 Peak frequency of $|Y(\omega)|$ (top) and values of $|\sigma|$ for the pellets differences (bottom).

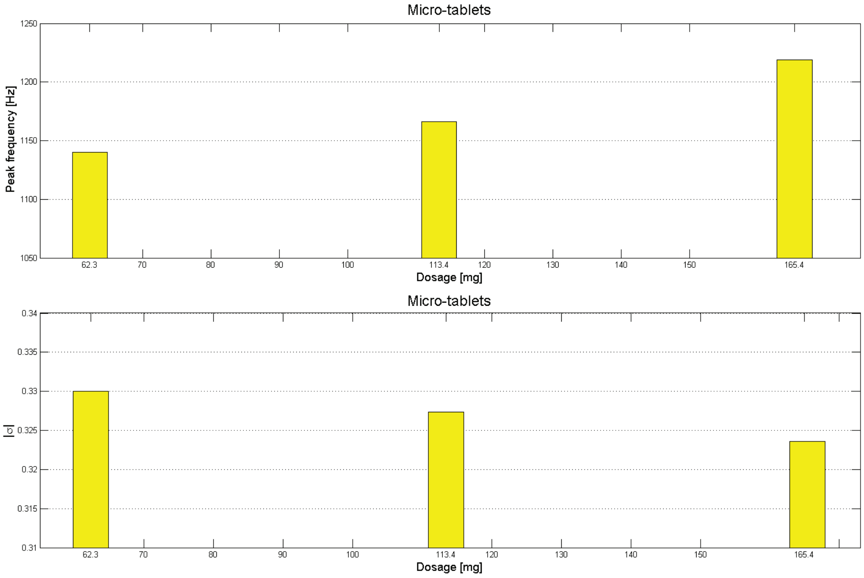
Micro-tablets

Micro-tablets

Fig. 5.19 Peak frequency of $|Y(\omega)|$ (top) and values of $|\sigma|$ for the micro-tablets differences.

5.3 Railway noise project

An additional useful application of the tympanometric prototypes regards the rail work security. We used the SIHT prototype and the prototype mounting the Microflown p-v probe during a set of measures to evaluate the noise generated by approaching high speed trains. Our aim is to understand if it's possible, through acoustic measures along the railways, to detect the arrival of the train with a sufficient forewarning. The objective is to detect the train through acoustic measures at least at a distance of 3-5 Km. One of the proposed methods for local detection of running trains is based on the operation of the sonar, by placing the transmitter on the train and the receiver on the railways [41]. We decided to use the p-v probes to directly the transmitted noise of the train along the railways [42].

The experimental set up consisted in:

- laptop for the acquisition and the analysis (Dell Inspiron);
- mechanical amplifier of the signal (stethoscope) and attachment system (plastic plate and magnets). See figure 5.20;
- SIHT tympanometric prototype and relative power supply;
- Microflown p-v match size probe inside the second tympanometer and relative signal conditioner;
- two plastic tubes, initially 5.25 m long and then reduced to 1.50 m;

- National Instrument acquisition device (USB-4431).

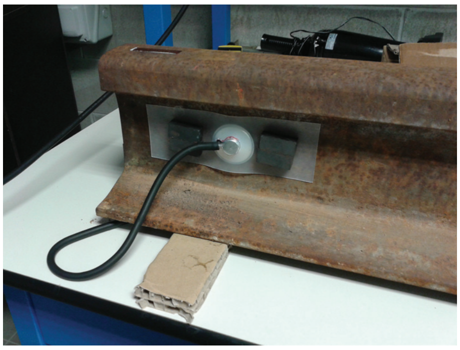

Fig. 5.20 Stethoscope used for the railway project: the object has been attached to the railway through some magnets.

Both the prototypes have been placed inside a box (Fig. 5.21) filled with phono absorbing material, from which come out the tubes that connect the probes to the stethoscope. We chose not to directly apply the probes to the railway because of the strong stress and electric discharge during the transit of the train that could damage the devices.

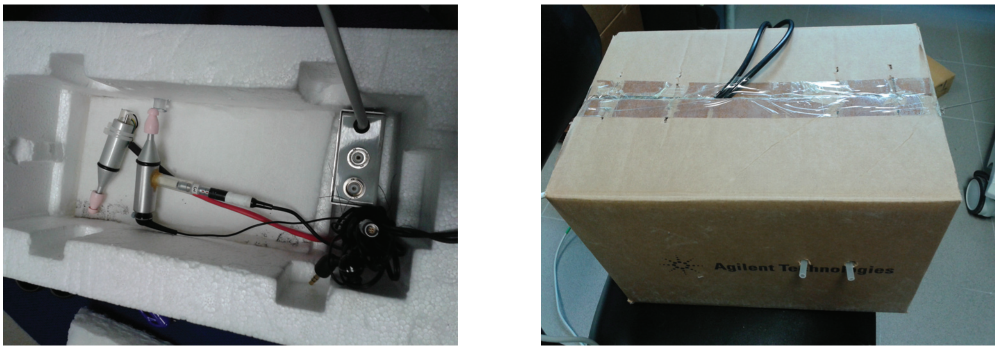

Fig. 5.21 Box in which we have put the two tympanometric probes: the SIHT one and the one mounting a Microflown p-v probe.

The data acquisition was done using the Sigview software, that is able to simultaneously register the pressure and velocity signals of the two probes, for a total of four tracks. We attached the stethoscopes on the external edge of the railway: in particular the measures were done on the odd railway (on the left side respect to the travelling direction).

A first set of measures was done using two tubes 5.25 m long to connect the probes to the stethoscope, but then we decided to reduce the length to 1.50 m, so improving the Signal-to-Noise ratio (Fig. 5.22).

An extract of one of the measures is shown in figure 5.23: the system results sensible to different sources of noise, such as background noise, the transit of an aeroplane (red frame) or the transit of a train along a different railway from the one under test (blue frame).

Fig. 5.22 Experimental set ups: on the left the first disposition, with long plastic tubes, and the stethoscopes placed on the odd railway; on the right the reduced tubes.

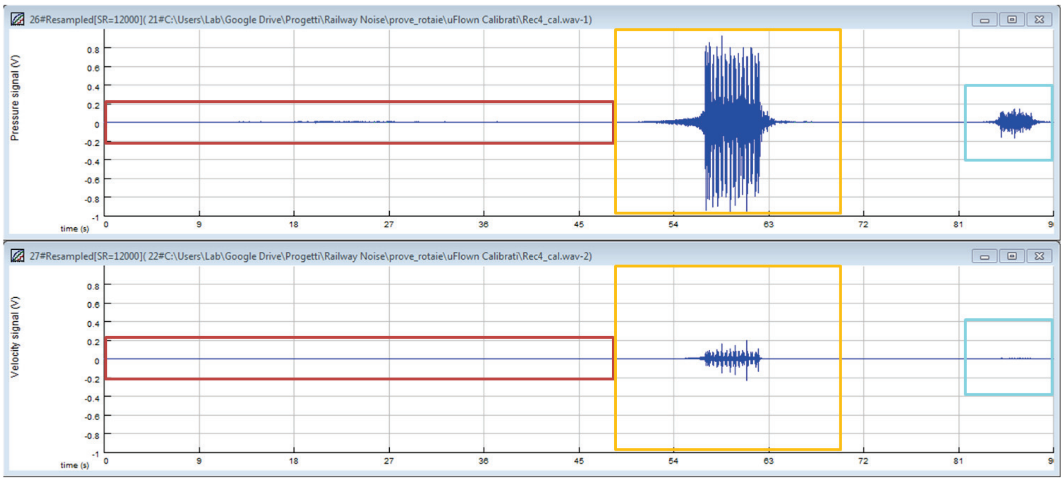

Fig. 5.23 Fourth measure, pressure (top) and velocity (bottom). We registered three events: the transit of an aeroplane, in the red frame; of a high speed train, in the yellow frame, and a high speed train along the railway not under test, blue frame.

From a spectral analysis of the time histories it’s not possible to identify a precursor that announces the transit of the train except for few seconds before the event. Ten seconds before, we can observe frequency components well distributed between 1.5 and 2 KHz, that decrease very rapidly, in 2-3 s, after the transit. Figures from 5.24 to 5.27 resume the pressure and velocity spectra up to 3 KHz during the pass of the train at various moments; to be more precise:

- **9.5 s before the transit (Fig. 5.24)**: represents the last moment in which it’s not possible to detect the train. The spectra only show low frequencies background noise;
- **8.5 s (Fig. 5.25)**: both the probes detect a peak in the frequency bands of [800-1200] Hz and [1500-1900] Hz;
- **5.0 s (Fig. 5.26)**: the train is 320 m far from the measurement point and the components found in the previous moment are higher than the background noise;
- **0.0 s (Fig. 5.27)**: during the pass of the train the registered signal is of wide band and covers the whole spectrum.

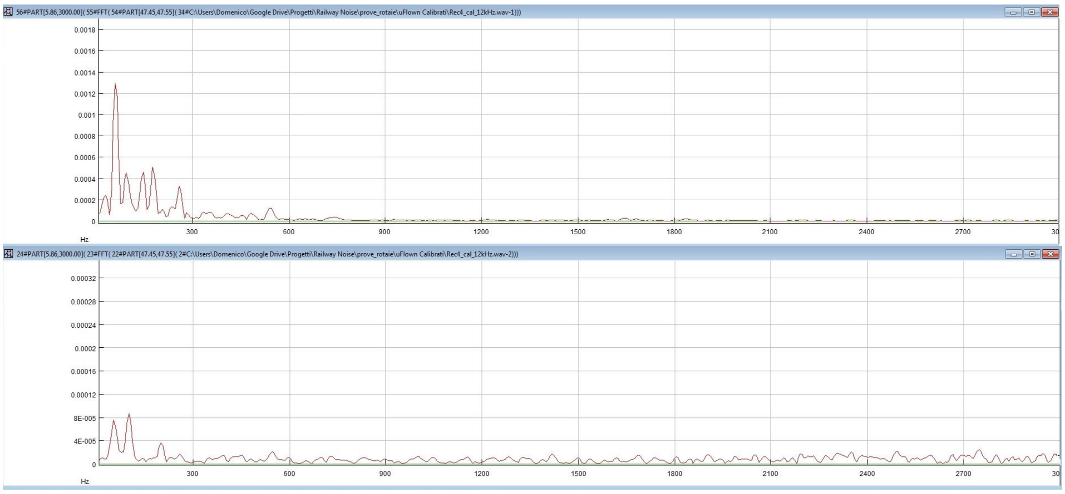

Fig. 5.24 Spectra of pressure (top) and velocity (bottom) 9.5 s before the arrival of the train. For the Fourier transformation we used a window of $\Delta t = 0.1$ s.

In order to confirm the results showed in the previous figures, it’s necessary to compare the effective events with other measurements in which other signals are detected. A big amount of measures would be necessary to this aim, but in this section two examples are shown (figures 5.28 and 5.29). On one side the spectrum of the aeroplane is very different from the one relative to the high speed train, on the other side the other event (train along the

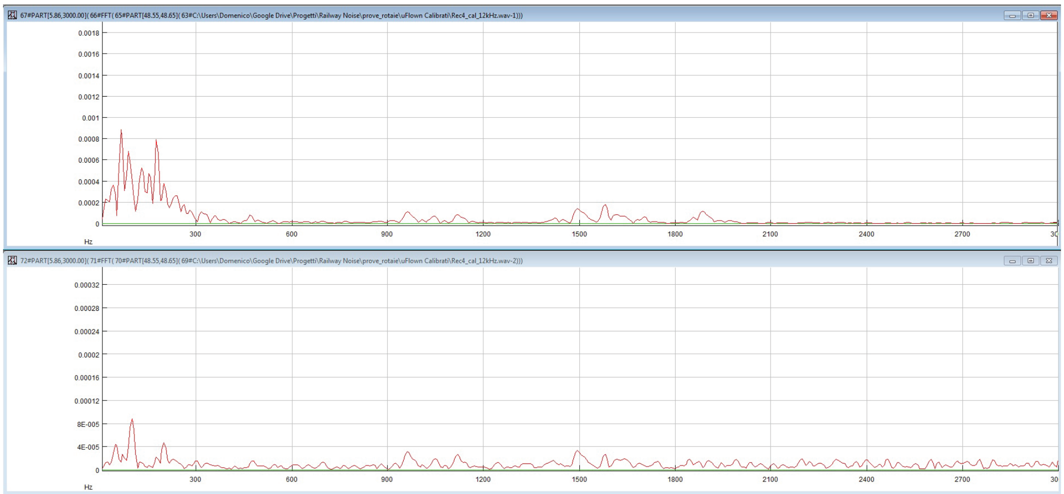

Fig. 5.25 Spectra of pressure (top) and velocity (bottom) 8.5 s before the arrival of the train. For the Fourier transformation we used a window of Δt = 0.1 s.

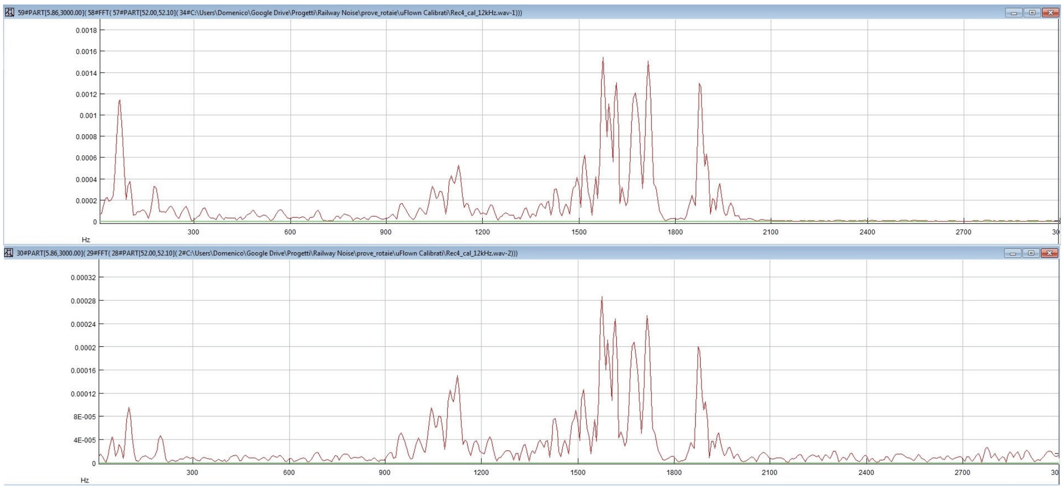

Fig. 5.26 Spectra of pressure (top) and velocity (bottom) 5 s before the arrival of the train. For the Fourier transformation we used a window of Δt = 0.1 s.

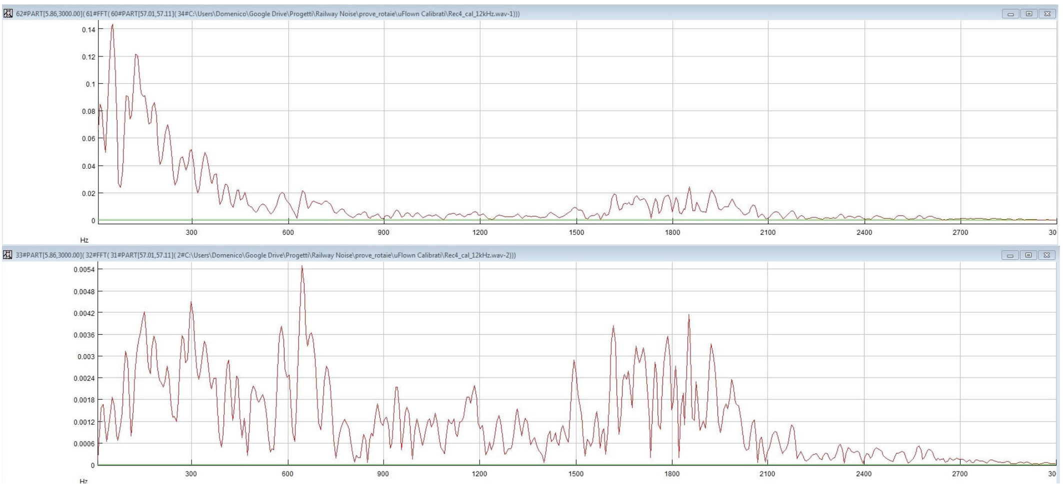

Fig. 5.27 Spectra of pressure (top) and velocity (bottom) during the arrival of the train. For the Fourier transformation we used a window of Δt = 0.1 s.

railway not under test) has the same frequency components at 1500 Hz and 1800 Hz, but lower intensities. Therefore it will be necessary to establish a precise factor that identify the transit of the train along the right railway: to do that we will need more set of measures.

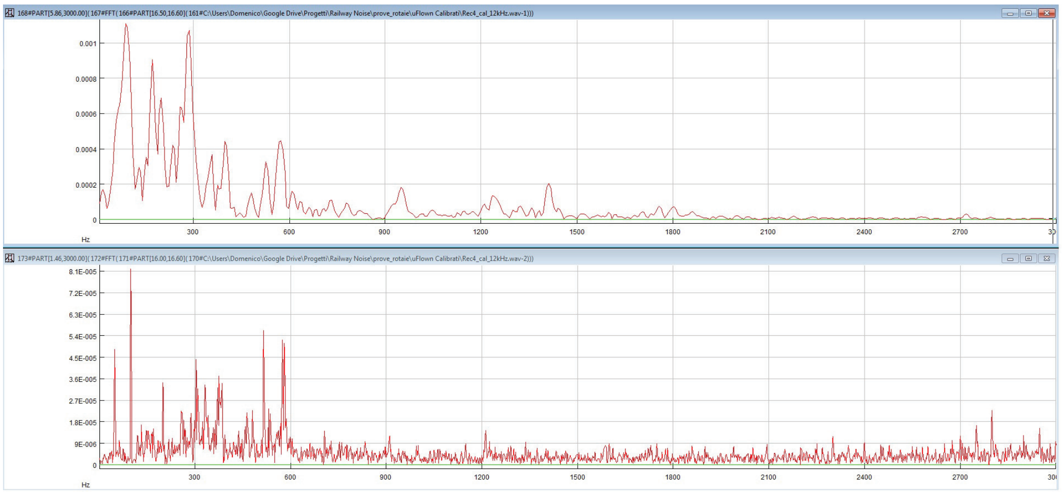

Fig. 5.28 Spectra of pressure (top) and velocity (bottom) during the transit of an aeroplane. For the Fourier transformation we used a window of Δt = 0.1 s.

The results have shown that it's necessary to improve the system in order to increase the advance warning: at the moment it's of ten seconds, but the required time is at least of 30 seconds. Some possible improvements in the system are a better acoustic insulation of the tubes (to increase the Signal to Noise ratio) and to enlarge the surface of contact between the stethoscope and the railway. Finally, exploring the low frequency bands, in particular the infrasounds, would contribute to significantly improve the detection of the trains.

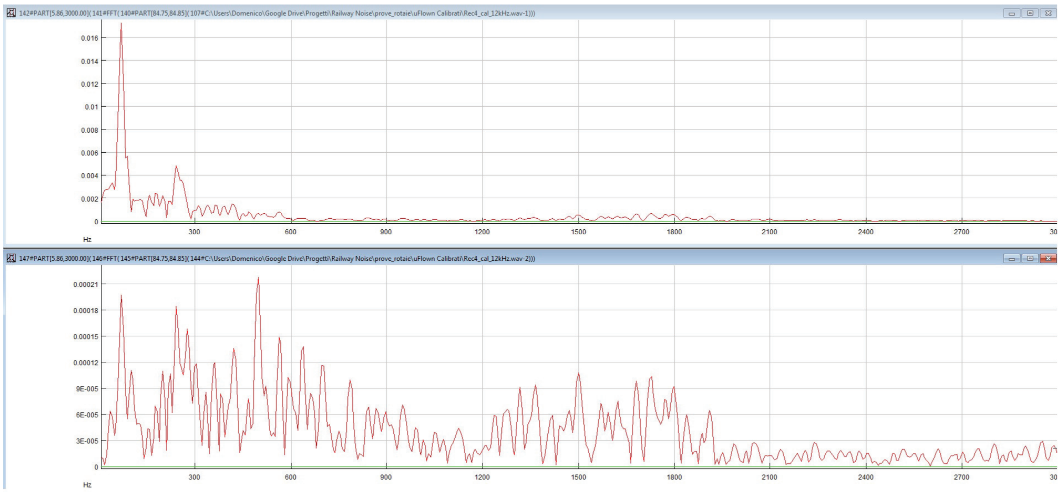

Fig. 5.29 Spectra of pressure (top) and velocity (bottom) during the transit of an aeroplane. For the Fourier transformation we used a window of $\Delta t = 0.1$ s.

5.4 Condition monitoring of washing machines

One of the first applications of the acoustic horns described in section 3.4 is the condition monitoring of household appliances. Here below a set of acoustic measures realised in one of the main Italian appliances industries: in particular our aim was to detect, through pressure-velocity measurements, eventual damages in a washing machine [43].

Being the data confidential and still under evaluation, I will limit myself to a qualitative discussion of the first results, and the plots here presented will lack of the vertical axes.

The measures were made using the Microflown p-v match size probe inserted in the carbon fibre horn and put close to the back of the washing machine under test (Fig. 5.30). The acquisition and the successive analysis was held using the sofwtware *Spectraplus*, after calibrating the data.

Three different washing machines were analysed, each one with various kind of damages:

- 1200 rpm machine: functioning, rotor issue and motor damaged;
- 1400 rpm machine: functioning and rotor issue;
- 1600 rpm machine: functioning, motor and belt damaged.

5.4.1 1200 rpm machine

Figures from 5.31 to 5.33 resume the impedance measured for three different conditions:functioning machine, motor damaged and rotor issue. The second plot shows values of impedance 10 dB

Fig. 5.30 The acoustic horn hosting the Microflown p-v match size probe, placed in the back of the washing machine.

higher than the functioning case, but an unchanged curve shape. On the contrary the motor damaged generates an increase in the impedance up to 1000 Hz, in particular in the range of [150-300] Hz and [600-1000] Hz.

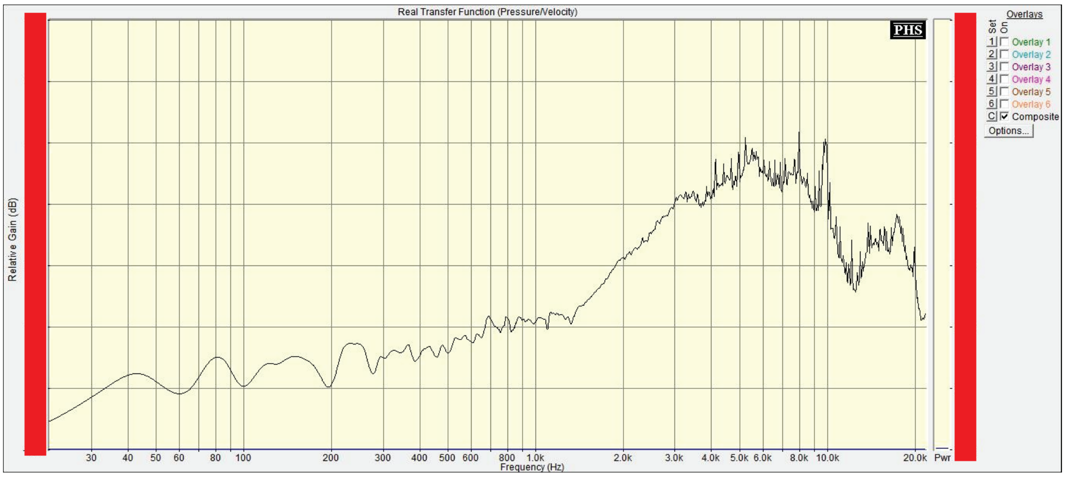

Fig. 5.31 Impedance of the functioning 1200 rpm washing machine. *The data are confidential, so the vertical scale has been omitted.*

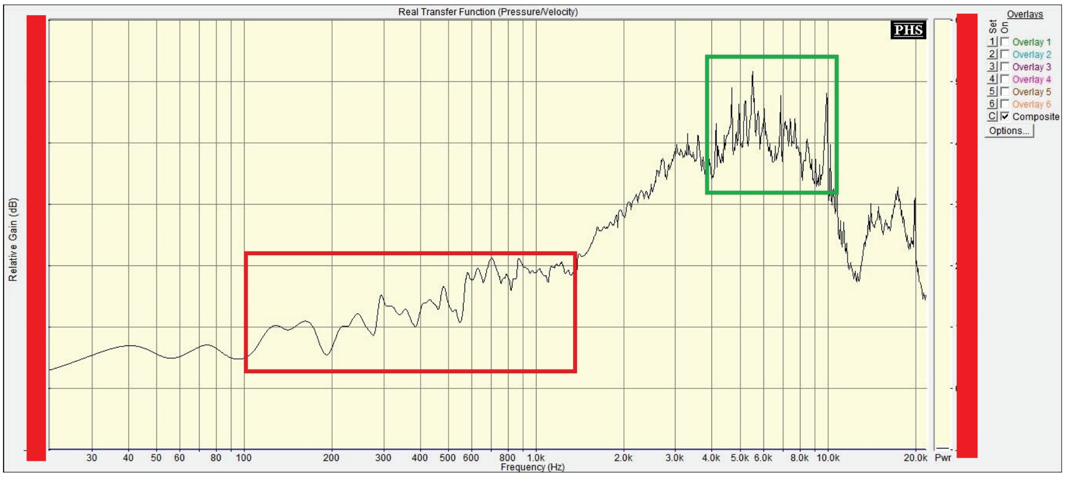

Fig. 5.32 Impedance of the 1200 rpm washing machine with motor damaged. *The data are confidential, so the vertical scale has been omitted.*

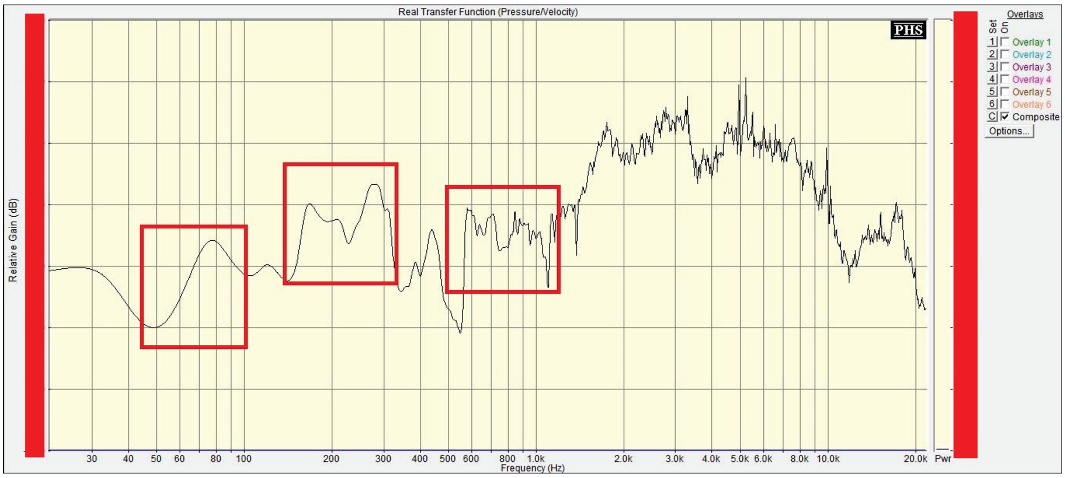

Fig. 5.33 Impedance of the 1200 rpm washing machine with rotor issue. *The data are confidential, so the vertical scale has been omitted.*

5.4.2 1400 rpm machine

The main results of tests on the 1400 rpm washing machine are resumed in figures 5.34 and 5.35. The first one shows the impedance of the functioning washing machine, while in figure 5.35 we can appreciate the comparison between the impedance of the rotor issue (in black) and the same measurement with the 1200 rpm machine with rotor issue on the background. It's relevant how the trend of the impedance remains unvaried in the second case. Being the impedance the ratio between pressure and velocity, we conclude that the introduction of an external disturbance such as another washing machine in function is registered only as an increment in pressure, thus revealing the importance of a pressure-velocity measure.

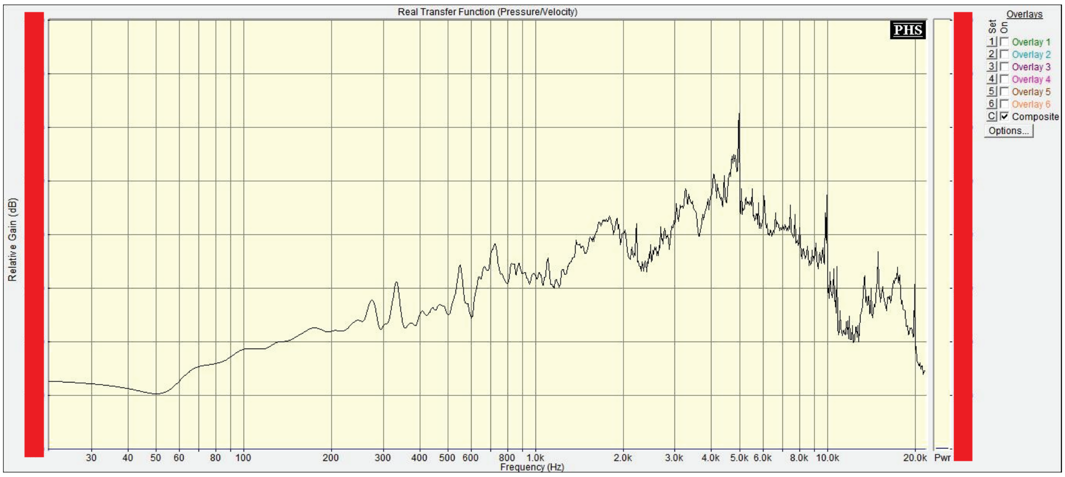

Fig. 5.34 Impedance of the functioning 1400 rpm washing machine. *The data are confidential, so the vertical scale has been omitted.*

5.4.3 1600 rpm machine

Figures from 5.36 to 5.39 show the impedance measured with the 1600 rpm washing machine with different kind of damages. The first one regards a functioning machine, then on the same machine a damaged motor has been mounted: the resulting impedance is illustrated in figure 5.37. The frames highlights the bands of greatest interest: the impedance has 10 dB higher values than in the normal condition, but in particular an increased signal of pressure (and hence of impedance) is localised around 300-500 Hz.

Figure 5.38 represents the measured impedance of a 1600 rpm machine with damaged motor and belt (to simulate the belt damage, a piece of gum has been attached to it). In order to better understand the effect of the belt damage, it's useful to consider figure 5.39 that draws the difference between the machine with only damaged motor and the one with

Fig. 5.35 Impedance of the 1400 rpm washing machine with rotor issue (black) and with the 1200 rpm machine working on the background (green). *The data are confidential, so the vertical scale has been omitted.*

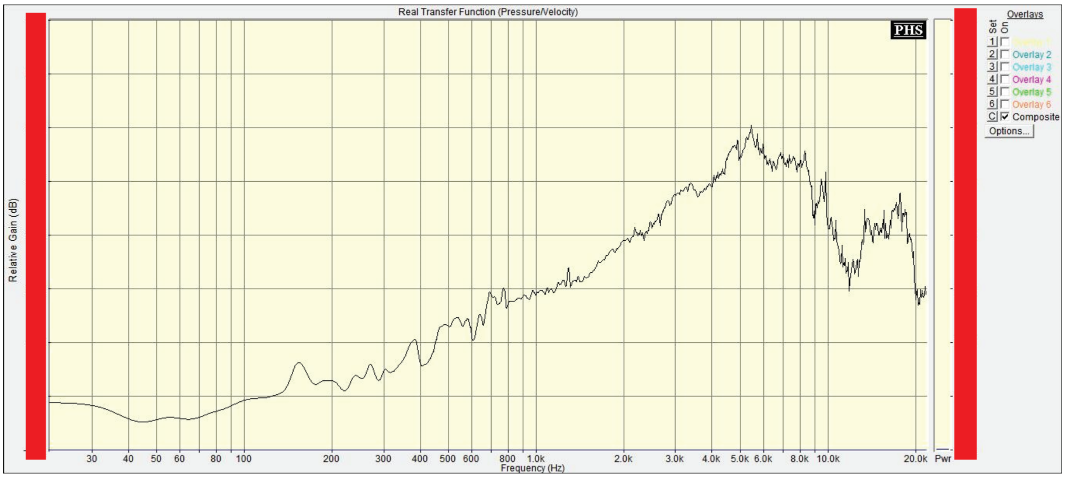

Fig. 5.36 Impedance of the functioning 1600 rpm washing machine. *The data are confidential, so the vertical scale has been omitted.*

Fig. 5.37 Impedance of the 1600 rpm washing machine with damaged motor. *The data are confidential, so the vertical scale has been omitted.*

both damaged motor and belt. The green frame indicates the band frequency in wich the difference is more evident, that is at middle frequencies (between 600 and 1000 Hz).

Fig. 5.38 Impedance of the 1600 rpm washing machine with damaged motor and belt. *The data are confidential, so the vertical scale has been omitted.*

The present section has resumed the results of a first set of measures on washing machines along the assembly line. We chose to analyse the impedance because such a quantity gives information on eventual damages much more than the single pressure or velocity signal.

Fig. 5.39 Difference of impedance between the 1600 rpm washing machine with damaged motor and belt and the one with only damaged motor. *The data are confidential, so the vertical scale has been omitted.*

Conclusions

The topic of this work is the realisation, the characterisation and the calibration of a new kind of low-cost pressure-velocity probe. Such device has been realised under the general coordination of the Institute CNR-IDASC at Ferrara within the SIHT (Sogliano Industrial High Technology) project, in collaboration with CNR-IEIIT in Pisa and Deltatech Industry (Sogliano al Rubicone). The development of a new intensimetric probe including an acoustic velocimetric micro-sensor represents a key to the understanding of Acoustical Energetics, and gives the possibility to measure the pressure and the velocity of the air particle at the same time. This aspect represents an innovation in the study of Energetics, because it allows to directly measure different quantities with just one set of measures.

After a theoretical introduction on the Acoustical Energetics, and the description of the main energetic quantities supported by numerical simulations, this thesis gives a review of the p-v micro-sensors, and illustrates a new method of calibration developed at Ferrara Laboratory. In fact the particular geometry of the realised prototype, which has been inserted in a tympanometric probe, has required the conception of a new method of calibration, the pressure-velocity comparison calibration, that is based on the measurements of a reference pre-calibrated probe (in our case mounting a Microflown p-v match size). The complexity and the innovation of this procedure are described in chapter 4, where the good stability of the measures and the simplicity of the post-processing are stressed.

This work has demonstrated the great reliability of the SIHT prototypes, and also their versatility. Last chapter is in fact dedicated to some case studies which demonstrate the various applications of such probes: first of all the audiometric field, where a probe of this kind is used for the first time, and the interpretation of the results is still at the beginning. Another important application regards the condition monitoring, which has brought good results in the study of the damages in the washing machines.

The prototypes here described are a first generation of a new sensor that will be improved and perfected in the future, thanks to the characterisation we have done in the laboratory of Ferrara. The aim of the project in fact is to expand the production of such devices to few dozen of samples, and in this way the research on characterisation and calibration has been fundamental.

Appendix A

Appendix

The next appendices resume some of the algorithms realised during the research presented in this thesis. The first one is dedicated to the simulation of Energetics Acoustics quantities using Maple (see section 1.4).

The second one presents the three algorithms realised in Matlab for the calibration of the Microflown p-v probe and the fitting of the relative correction curve (see section 2.4).

Simulation of a 1-D quasi stationary wave using Maple

Simulation of a 1-D quasi-stationary sound wave field
by M.Buiat, D.Stanzial @Fe, 31 Jul 2014.

Monochromatic wave

Definition of the procedure to calculate the stationary mean

Description:
calculate the stationary time average *z* of a function defined as a global expression *stain* for each passed argument *out*

```
sta :=proc(out)
local T, z;
global stain;
z := limit(1/(2*T)*(int(stain, t=-T..+T)), T= ∞);
end;
```

$$\mathbf{proc}(out)\ \mathbf{local}\ T, z;\ \mathbf{global}\ stain;\ z := limit(1/2 * int(stain, t = -T..T)/T, T = \infty)\ \mathbf{end\ proc} \tag{1}$$

Definition of the potential field

```
assume(A :: realcons, c :: realcons, k :: realcons, ω :: realcons, R :: realcons, ϑ :: realcons, ρ
      :: realcons);           #restriction of the parameters domain
assume(Ab :: realcons, kb :: realcons, ωb :: realcons, Rb :: realcons, ϑb :: realcons);
assume(Ac :: realcons, kc :: realcons, ωc :: realcons, Rc :: realcons, ϑc :: realcons);
K := (x, t) →Re(A·c·(exp(I·(k·x − ω·t)) + R·exp(I·(k·x + ω·t + ϑ))));
                                        #definition of the potential
ϕ := (x, t) → evalc(K(x, t));
ϕ(x, t);
```

$$(x, t) \rightarrow \Re\left(A\, c\left(\mathrm{e}^{\mathrm{I}(kx - \omega t)} + R\, \mathrm{e}^{\mathrm{I}(kx + \omega t + \vartheta)}\right)\right)$$

$$(x, t) \rightarrow evalc(K(x, t))$$

$$A{\sim}\, c{\sim} \left(\cos(k{\sim}\, x - \omega{\sim}\, t) + R{\sim} \cos(k{\sim}\, x + \omega{\sim}\, t + \vartheta{\sim})\right) \tag{2}$$

$$\tag{3}$$

```
Kb := (x, tb) →Re(Ab·c·(exp(I·(kb·x − ωb·tb))-Rb·exp(I·(kb·x + ωb·tb + ϑb))));
```

$$pot := (x, tb) \rightarrow evalc(Kb(x, tb));$$
$$pot(x, tb);$$

$$(x, tb) \rightarrow \Re\left(Ab\, c\, \left(\mathrm{e}^{\mathrm{I}\,(kb\,x - \omega b\,tb)} - Rb\, \mathrm{e}^{\mathrm{I}\,(kb\,x + \omega b\,tb + \vartheta b)}\right)\right)$$
$$(x, tb) \rightarrow evalc(Kb(x, tb))$$
$$-Ab{\sim}\, c{\sim}\, \left(-\cos(kb{\sim}\, x - \omega b{\sim}\, tb) + Rb{\sim} \cos(kb{\sim}\, x + \omega b{\sim}\, tb + \vartheta b{\sim})\right)$$

$$Kc := (x, t) \rightarrow \mathrm{Re}\left(Ab \cdot c \cdot \left(\exp(I \cdot (kb \cdot x - \omega b \cdot t)) - Rb \cdot \exp(I \cdot (kb \cdot x + \omega c \cdot t + \vartheta b))\right)\right);$$

$$potc := (x, t) \rightarrow evalc(Kc(x, t));$$
$$potc(x, t);$$

$$(x, t) \rightarrow \Re\left(Ab\, c\, \left(\mathrm{e}^{\mathrm{I}\,(kb\,x - \omega b\,t)} - Rb\, \mathrm{e}^{\mathrm{I}\,(kb\,x + \omega c\,t + \vartheta b)}\right)\right)$$
$$(x, t) \rightarrow evalc(Kc(x, t))$$
$$-Ab{\sim}\, c{\sim}\, \left(-\cos(kb{\sim}\, x - \omega b{\sim}\, t) + Rb{\sim} \cos(kb{\sim}\, x + \omega c\, t + \vartheta b{\sim})\right) \tag{5}$$

Derivation of the wave observables (pressure and velocity)

$$p := (x, t) \rightarrow -\rho \cdot \frac{\partial}{\partial t}\, \phi(x, t);$$
$$v := (x, t) \rightarrow \frac{\partial}{\partial x}\, \phi(x, t);$$

$$(x, t) \rightarrow -\rho \left(\frac{\partial}{\partial t}\, \phi(x, t)\right)$$
$$(x, t) \rightarrow \frac{\partial}{\partial x}\, \phi(x, t) \tag{6}$$

$$p(x, t);$$
$$-\rho{\sim}\, A{\sim}\, c{\sim}\, \left(\sin(k{\sim}\, x - \omega{\sim}\, t)\, \omega{\sim} - R{\sim} \sin(k{\sim}\, x + \omega{\sim}\, t + \vartheta{\sim})\, \omega{\sim}\right) \tag{7}$$

$$v(x, t);$$
$$A{\sim}\, c{\sim}\, \left(-\sin(k{\sim}\, x - \omega{\sim}\, t)\, k{\sim} - R{\sim} \sin(k{\sim}\, x + \omega{\sim}\, t + \vartheta{\sim})\, k{\sim}\right) \tag{8}$$

$$pb := (x, tb) \rightarrow -\rho \cdot \frac{\partial}{\partial x}\mathrm{pot}(x, tb);$$
$$vb := (x, tb) \rightarrow \frac{\partial}{\partial x}\, pot(x, tb);$$

$$(x, tb) \rightarrow -\rho \left(\frac{\partial}{\partial x}\, pot(x, tb)\right)$$
$$(x, tb) \rightarrow \frac{\partial}{\partial x}\, pot(x, tb) \tag{9}$$

$$pb(x, tb);$$
$$\rho{\sim}\, Ab{\sim}\, c{\sim}\, \left(\sin(kb{\sim}\, x - \omega b{\sim}\, tb)\, kb{\sim} - Rb{\sim} \sin(kb{\sim}\, x + \omega b{\sim}\, tb + \vartheta b{\sim})\, kb{\sim}\right) \tag{10}$$

$$vb(x, tb);$$
$$-Ab{\sim}\, c{\sim}\, \left(\sin(kb{\sim}\, x - \omega b{\sim}\, tb)\, kb{\sim} - Rb{\sim} \sin(kb{\sim}\, x + \omega b{\sim}\, tb + \vartheta b{\sim})\, kb{\sim}\right) \tag{11}$$

$$pc := (x,t) \rightarrow -\rho \cdot \frac{\partial}{\partial x}\mathrm{potc}(x,t);$$

$$vc := (x,t) \rightarrow \frac{\partial}{\partial x}\, potc(x,t);$$

$$(x,t) \rightarrow -\rho \left(\frac{\partial}{\partial x}\, potc(x,t) \right)$$

$$(x,t) \rightarrow \frac{\partial}{\partial x}\, potc(x,t) \tag{12}$$

$$pc(x,t);$$

$$\rho{\sim}\, Ab{\sim}\, c{\sim} \left(\sin\left(kb{\sim}\, x - \omega b{\sim}\, t\right) kb{\sim} - Rb{\sim} \sin\left(kb{\sim}\, x + \omega c\, t + \vartheta b{\sim}\right) kb{\sim} \right) \tag{13}$$

$$vc(x,t);$$

$$-Ab{\sim}\, c{\sim} \left(\sin\left(kb{\sim}\, x - \omega b{\sim}\, t\right) kb{\sim} - Rb{\sim} \sin\left(kb{\sim}\, x + \omega c\, t + \vartheta b{\sim}\right) kb{\sim} \right) \tag{14}$$

Definition of the istantaneous energetic fields

$$j := (x,t) \rightarrow p(x,t) \cdot v(x,t) :$$

$$wk := (x,t) \rightarrow \frac{1}{2} \cdot \rho \cdot v^2(x,t) :$$

#istantaneous kinetic energy

$$wp := (x,t) \rightarrow \frac{1}{2 \cdot \rho \cdot c^2} \cdot p^2(x,t) :$$

#istantaneous potential energy

$$w := (x,t) \rightarrow wk(x,t) + wp(x,t) :$$

#istantaneous total energy

$$j(x,t);$$

$$-\rho{\sim}\, A{\sim}^2\, c{\sim}^2 \left(\sin\left(k{\sim}\, x - \omega{\sim}\, t\right) \omega{\sim} - R{\sim} \sin\left(k{\sim}\, x + \omega{\sim}\, t + \vartheta{\sim}\right) \omega{\sim} \right) \left(-\sin\left(k{\sim}\, x - \omega{\sim}\, t\right) k{\sim} - R{\sim} \sin\left(k{\sim}\, x + \omega{\sim}\, t + \vartheta{\sim}\right) k{\sim} \right) \tag{15}$$

$$wk(x,t);$$

$$\frac{1}{2}\, \rho{\sim}\, A{\sim}^2\, c{\sim}^2 \left(-\sin\left(k{\sim}\, x - \omega{\sim}\, t\right) k{\sim} - R{\sim} \sin\left(k{\sim}\, x + \omega{\sim}\, t + \vartheta{\sim}\right) k{\sim} \right)^2 \tag{16}$$

$$wp(x,t);$$

$$\frac{1}{2}\, \rho{\sim}\, A{\sim}^2 \left(\sin\left(k{\sim}\, x - \omega{\sim}\, t\right) \omega{\sim} - R{\sim} \sin\left(k{\sim}\, x + \omega{\sim}\, t + \vartheta{\sim}\right) \omega{\sim} \right)^2 \tag{17}$$

$$w(x,t);$$

$$\frac{1}{2}\, \rho{\sim}\, A{\sim}^2\, c{\sim}^2 \left(-\sin\left(k{\sim}\, x - \omega{\sim}\, t\right) k{\sim} - R{\sim} \sin\left(k{\sim}\, x + \omega{\sim}\, t + \vartheta{\sim}\right) k{\sim} \right)^2 + \frac{1}{2}\, \rho{\sim}\, A{\sim}^2 \left(\sin\left(k{\sim}\, x - \omega{\sim}\, t\right) \omega{\sim} - R{\sim} \sin\left(k{\sim}\, x + \omega{\sim}\, t + \vartheta{\sim}\right) \omega{\sim} \right)^2 \tag{18}$$

Calcolo dei campi medi stazionari

$$stain := wk(x,t) : Wk := factor\left(algsubs\left(k \cdot c = \omega, combine(sta(out), trig)\right)\right);$$

#stationary kinetic energy

$$-\frac{1}{4}\, \rho{\sim}\, A{\sim}^2\, \omega{\sim}^2 \left(-1 + 2\, R{\sim} \cos\left(2\, k{\sim}\, x + \vartheta{\sim}\right) - R{\sim}^2 \right) \tag{19}$$

$stain := wp(x,t) : Wp := factor\big(algsubs\big(k\cdot c = \omega, combine(sta(out), trig)\big)\big);$

#stationary potential energy

$$\frac{1}{4}\,\rho{\sim}\,A{\sim}^{2}\,\omega{\sim}^{2}\,\left(1+2\,R{\sim}\cos(2\,k{\sim}\,x+\vartheta{\sim})+R{\sim}^{2}\right) \tag{20}$$

$W := factor(combine(Wk+Wp, trig));$

#stationary total energy

$$\frac{1}{2}\,\rho{\sim}\,A{\sim}^{2}\,\omega{\sim}^{2}\,\left(1+R{\sim}^{2}\right) \tag{21}$$

$L := factor(combine(Wk-Wp, trig));$

#Lagrangian

$$-\rho{\sim}\,A{\sim}^{2}\,\omega{\sim}^{2}\,R{\sim}\cos(2\,k{\sim}\,x+\vartheta{\sim}) \tag{22}$$

$\xrightarrow{\text{differentiate w.r.t. x}}$

$$2\,\rho{\sim}\,A{\sim}^{2}\,\omega{\sim}^{2}\,R{\sim}\sin(2\,k{\sim}\,x+\vartheta{\sim})\,k{\sim} \tag{23}$$

$prad := \dfrac{(2\cdot L-W)}{3};$

#radiation pressure

$$-\frac{2}{3}\,\rho{\sim}\,A{\sim}^{2}\,\omega{\sim}^{2}\,R{\sim}\cos(2\,k{\sim}\,x+\vartheta{\sim})-\frac{1}{6}\,\rho{\sim}\,A{\sim}^{2}\,\omega{\sim}^{2}\,\left(1+R{\sim}^{2}\right) \tag{24}$$

$stain := j(x,t) : J1 := simplify(factor(sta(out))) : J := algsubs\big(k\cdot c = \omega, J1\big);$

#radiant flux

$$-\frac{1}{2}\,\omega{\sim}^{2}\,\rho{\sim}\,A{\sim}^{2}\,\left(-1+R{\sim}^{2}\right)\,c{\sim} \tag{25}$$

$Jtot := 2\cdot c\cdot\sqrt{Wk\cdot Wp};$

#apparent flux

$$\frac{1}{2}\,c{\sim}\,A{\sim}^{2}\,\omega{\sim}^{2}\,\sqrt{-\rho{\sim}^{2}\,\left(-1+2\,R{\sim}\cos(2\,k{\sim}\,x+\vartheta{\sim})-R{\sim}^{2}\right)\left(1+2\,R{\sim}\cos(2\,k{\sim}\,x+\vartheta{\sim})+R{\sim}^{2}\right)} \tag{26}$$

Computation of the indicators and of the p-v phase

$\eta := \dfrac{J}{c\cdot W};$

#conductance

$$-\frac{-1+R{\sim}^{2}}{1+R{\sim}^{2}} \tag{27}$$

$\sigma := simplify\left(\dfrac{Jtot}{c\cdot W}, trig\right)$ assuming *nonnegative*;

#sound energy admittance

$$\frac{\sqrt{1+2\,R{\sim}^{2}-4\,R{\sim}^{2}\cos(2\,k{\sim}\,x+\vartheta{\sim})^{2}+R{\sim}^{4}}}{1+R{\sim}^{2}} \tag{28}$$

$$\xi := \frac{\eta}{\sigma};$$

#acoustic power factor

$$-\frac{-1+R\sim^2}{\sqrt{1+2\,R\sim^2-4\,R\sim^2\cos(2\,k\sim x+\vartheta\sim)^2+R\sim^4}} \tag{29}$$

$$\tau := \sigma\cdot\sqrt{\frac{1-\xi^2}{1-\eta^2}};$$

$$\frac{1}{1+R\sim^2}\left(\sqrt{1+2\,R\sim^2-4\,R\sim^2\cos(2\,k\sim x+\vartheta\sim)^2+R\sim^4}\;\sqrt{\frac{1-\frac{(-1+R\sim^2)^2}{1+2\,R\sim^2-4\,R\sim^2\cos(2\,k\sim x+\vartheta\sim)^2+R\sim^4}}{1-\frac{(-1+R\sim^2)^2}{(1+R\sim^2)^2}}}\right) \tag{30}$$

p-v phase

$$\phi := \operatorname{signum}(\sin(2\cdot k\cdot x+\vartheta))\cdot\arccos(\xi);$$

$$\operatorname{signum}(\sin(2\,k\sim x+\vartheta\sim))\left(\pi-\arccos\left(\frac{-1+R\sim^2}{\sqrt{1+2\,R\sim^2-4\,R\sim^2\cos(2\,k\sim x+\vartheta\sim)^2+R\sim^4}}\right)\right) \tag{31}$$

#reactive intensity

$$Q := \sqrt{Jtot^2-J^2};$$

$$\frac{1}{2}\left(-c\sim^2 A\sim^4\omega\sim^4\rho\sim^2\left(-1+2\,R\sim\cos(2\,k\sim x+\vartheta\sim)-R\sim^2\right)\left(1+2\,R\sim\cos(2\,k\sim x+\vartheta\sim)\right.\right.$$
$$\left.\left.+R\sim^2\right)-\omega\sim^4\rho\sim^2 A\sim^4\left(-1+R\sim^2\right)^2 c\sim^2\right)^{1/2} \tag{32}$$

$$\mu := \frac{Q}{c\cdot W};$$

#reactivity index

$$\frac{1}{c\sim\rho\sim A\sim^2\omega\sim^2\left(1+R\sim^2\right)}\left(-c\sim^2 A\sim^4\omega\sim^4\rho\sim^2\left(-1+2\,R\sim\cos(2\,k\sim x+\vartheta\sim)-R\sim^2\right)\left(1\right.\right.$$
$$\left.\left.+2\,R\sim\cos(2\,k\sim x+\vartheta\sim)+R\sim^2\right)-\omega\sim^4\rho\sim^2 A\sim^4\left(-1+R\sim^2\right)^2 c\sim^2\right)^{1/2} \tag{33}$$

Sintropic quantities

$a := (x, t) \rightarrow \frac{\textbf{(25)}}{\textbf{(20)}} \cdot \textbf{(17)}:$

$a(x, t);$

$$-\frac{\rho{\sim}\, A{\sim}^{2}\, (-1 + R{\sim}^{2})\, c{\sim}\, \left(\sin(k{\sim}\, x - \omega{\sim}\, t)\, \omega{\sim} - R{\sim} \sin(k{\sim}\, x + \omega{\sim}\, t + \vartheta{\sim})\, \omega{\sim}\right)^{2}}{1 + 2\, R{\sim} \cos(2\, k{\sim}\, x + \vartheta{\sim}) + R{\sim}^{2}} \qquad \textbf{(34)}$$

$r := (x, t) \rightarrow \textbf{(15)} - \textbf{(34)}:$

$r(x, t);$

$$-\rho{\sim}\, A{\sim}^{2}\, c{\sim}^{2} \left(\sin(k{\sim}\, x - \omega{\sim}\, t)\, \omega{\sim} - R{\sim} \sin(k{\sim}\, x + \omega{\sim}\, t + \vartheta{\sim})\, \omega{\sim}\right) \left(-\sin(k{\sim}\, x - \omega{\sim}\, t)\, k{\sim} - R{\sim} \sin(k{\sim}\, x + \omega{\sim}\, t + \vartheta{\sim})\, k{\sim}\right) + \frac{\rho{\sim}\, A{\sim}^{2}\, (-1 + R{\sim}^{2})\, c{\sim}\, \left(\sin(k{\sim}\, x - \omega{\sim}\, t)\, \omega{\sim} - R{\sim} \sin(k{\sim}\, x + \omega{\sim}\, t + \vartheta{\sim})\, \omega{\sim}\right)^{2}}{1 + 2\, R{\sim} \cos(2\, k{\sim}\, x + \vartheta{\sim}) + R{\sim}^{2}} \qquad \textbf{(35)}$$

Initialisation of the parameters

$\mathrm{Hz} := 100.;\ \mathrm{T} := \frac{1}{Hz};\ \mathrm{c} := 400.;\ \omega := \mathrm{evalf}(2\,\pi) \cdot Hz;\ k := \frac{\omega}{c};\ \lambda := \frac{c}{Hz};\ \rho := 1.204;\ A := 1.0046 \cdot 10^{-6};$

$\vartheta := \frac{\mathrm{evalf}(\pi)}{3};$

$$\begin{gathered} 100. \\ 0.01000000000 \\ 400. \\ 628.3185308 \\ 1.570796327 \\ 4.000000000 \\ 1.204 \\ 0.000001004600000 \\ 1.047197551 \end{gathered} \qquad \textbf{(36)}$$

Appendix B

Matlab algorithms for the calibration and fitting of the correction curve

B.1 Normalisation and union of the sweeps in the three bands

```matlab
%Algorithm to read the three wave files corresponding to the three bands
%and to create a single wave file.
refLev=40;

[yL,Fs]=wavread('ir_111_20-1200Hz.wav');
[yM,Fs]=wavread('ir_111_900-2200Hz.wav');
[yH,Fs]=wavread('ir_111_2000-15000Hz.wav');


pL=cumsum(flipud(yL).^2);
pM=cumsum(flipud(yM).^2);
pH=cumsum(flipud(yH).^2);
n(1)=find(flipud(10*log10(pL(:,1)/max(pL(:,1))))>-refLev,1,'last');
n(2)=find(flipud(10*log10(pL(:,2)/max(pL(:,2))))>-refLev,1,'last');
n(3)=find(flipud(10*log10(pM(:,1)/max(pM(:,1))))>-refLev,1,'last');
n(4)=find(flipud(10*log10(pM(:,2)/max(pM(:,2))))>-refLev,1,'last');
n(5)=find(flipud(10*log10(pH(:,1)/max(pH(:,1))))>-refLev,1,'last');
n(6)=find(flipud(10*log10(pH(:,2)/max(pH(:,2))))>-refLev,1,'last');


L=max(n);
```

```matlab
NFFT=2^nextpow2(L);

f = Fs/2*linspace(0,1,NFFT/2); %common frequency vector

f1=950; f2=2100;
u1=find(f<=f1);
u2=find((f>f1)&(f<=f2));
u3=find(f>f2);

YL=fft(yL(1:L,:),NFFT);
YM=fft(yM(1:L,:),NFFT);
YH=fft(yH(1:L,:),NFFT);

c1(1)=abs(YL(u1(end),1))./abs(YM(u2(1)-1,1));
c1(2)=abs(YL(u1(end),2))./abs(YM(u2(1)-1,2));
c2(1)=abs(YM(u2(end),1))./abs(YH(u3(1)-1,1));
c2(2)=abs(YM(u2(end),2))./abs(YH(u3(1)-1,2));
%
YT(:,1)=[YL(u1,1);c1(1)*YM(u2,1);c1(1)*c2(1)*[YH(u3,1);YH(u3(end)+1,1)];c1(1)*c2(1)*conj(flipud(YH(u3,1)));c1(1)*conj(flipud(YM(u2,1)));conj(flipud(YL(u1(2:end),1)))];
YT(:,2)=[YL(u1,2);c1(2)*YM(u2,2);c1(2)*c2(2)*[YH(u3,2);YH(u3(end)+1,2)];c1(2)*c2(2)*conj(flipud(YH(u3,2)));c1(2)*conj(flipud(YM(u2,2)));conj(flipud(YL(u1(2:end),2)))];

yt=real(ifft(YT,NFFT));

figure
plot(yt)
norm=1./max(abs(yt))
ynorm=[norm(1).*yt(:,1) norm(2).*yt(:,2)];
wavwrite(ynorm,48000,'ir-larix')
figure
loglog(f,abs(YT(1:NFFT/2,:)))
figure
plot(f,angle(YT(1:NFFT/2,:)))


Rcorr=abs(YT(:,1))-abs(YT(:,2));
Thetacorr=angle(YT(:,1))-angle(YT(:,2));

Ycorr=Rcorr.*exp(i*Thetacorr);

figure
```

```
plot(f,Rcorr(1:NFFT/2))
figure
plot(f,Thetacorr(1:NFFT/2))
```

B.2 Calibration and normalisation of the larix measurements

```
% %CALCULATION OF THE CORRECTION CURVE FOR PROGRESSIVE PLANE WAVE
    REFERENCE FIELDS

%close all

%Reading and normalisation of the wav files: 1-sweep bruel 2-ir bruel 3-
    ir
%probe under calibration
[ytnorm1,Fs,nbit,opts1]=wavread('sw_bruel_1.wav');
yt1=str2num(opts1.info.maxr)*ytnorm1(:,1);

[ytnorm2,Fs,nbit,opts2]=wavread('ir_bruel_1.wav');
yt2=str2num(opts2.info.maxr)*ytnorm2(:,1);

[ytnorm3,Fs,nbit,opts3]=wavread('ir-larix_3sw.wav');


yt3(:,1)=1.3839*ytnorm3(:,1);
yt3(:,2)=0.8449*ytnorm3(:,2);


[yt1kHz,Fs,nbit,calopts]=wavread('piston_BeK_1.wav'); %read the signal
    from pistonphone @1KHz

L1=max(length(yt1));
L2=max(length(yt2));
L3=max(length(yt3));
L4=max(length(yt1kHz));

L=max([L1,L2,L3,L4]);

NFFT=2^nextpow2(L);

f = Fs/2*linspace(0,1,NFFT/2); %common frequency vector
```

```matlab

Yf1=fft(yt1(1:L1,1),NFFT); %fft sweep Bruel
Yf2=fft(yt2(1:L2,1),NFFT); %fft  ir Bruel
Yf3=fft(yt3(1:L3,:),NFFT); %fft ir probe to calibrate
Yf1kHz=fft(yt1kHz(1:L4,1),NFFT); %fft of the signal from pistonphone @1KHz

x1kHz=find((f>999.9)&(f<1000.1))
calnorm=max(abs(Yf1kHz(x1kHz)))

% SOLVE FOR 94 dB
pref=2*10^-5
r = 1.0024 %convert symbolic to numeric and get cal r=1.0024

cal=r/calnorm;    %linear value corresponding to 94dB

Ycal1=cal*abs(Yf1); %common readout over 94dB B&K
Ycal2=cal*abs(Yf2);
Ycal3=cal*abs(Yf3);
C1kHz=cal*abs(Yf1kHz);


%Comparison Calibration to B&K sweep

x1norm=max(Ycal1(x1kHz))
x2norm=max(Ycal2(x1kHz))
x3normp=max(Ycal3(x1kHz,1))
x3normv=max(Ycal3(x1kHz,2))
xnorm3p=x1norm/x3normp
xnorm3v=x1norm/x3normv
xnorm2=x1norm/x2norm
Ycal3renorm=[xnorm3p*Ycal3(:,1) xnorm3v*Ycal3(:,2)];
Ycal2renorm=xnorm2*Ycal2;

         YG2=10*log10(abs(Ycal2renorm(1:NFFT/2,:))/pref);
         YG3=10*log10(abs(Ycal3renorm(1:NFFT/2,:))/pref);

         figure
         semilogx(f,YG2,'r',f,YG3,'g')

% Return to the time history

YpvirMf=[Ycal3renorm(:,1).*exp(1i*angle(Yf3(:,1))) Ycal3renorm(:,2).*exp(1i*angle(Yf3(:,2)))] ;
```

```
YpirBK=Ycal2.*exp(1i*angle(Yf2));
YpswrBK=Ycal1.*exp(1i*angle(Yf1));
YT3=[YpvirMf;conj(flipud(YpvirMf))];
YT2=[YpirBK;conj(flipud(YpirBK))];
YT1=[YpswrBK;conj(flipud(YpswrBK))];

yth3=real(ifft(YT3,NFFT));
yth2=real(ifft(YT2,NFFT));
yth1=real(ifft(YT1,NFFT));

yth3n=1./max(abs(yth3));
yth2n=1/max(abs(yth2));
yth1n=1/max(abs(yth1));

refLev=40;

y3th_=[yth3n(1)*yth3(:,1) yth3n(2)*yth3(:,2)];
y2th_=[yth2n*yth2 y3th_(:,1)];
y1th=yth1n*yth1;

%cut after 40dB p-irs decay
refLev=40;
y3th__=cumsum(flipud(y3th_(:,1)).^2);
y2th__=cumsum(flipud(y2th_(:,1)).^2);

n(1)=find(flipud(10*log10(y3th__/max(y3th__)))>-refLev,1,'last');
n(2)=find(flipud(10*log10(y2th__/max(y2th__)))>-refLev,1,'last');
Lt=max(n);

y3th=y3th_(1:Lt,:);
y2th=y2th_(1:Lt,:);


wavwrite(y1th,48000,'sw_bruel_cal.wav')
wavwrite(y2th,48000,'ir_bruel_1_cal.wav')
wavwrite(y3th,48000,'ir-larix_pvcal.wav')


% Computation of Sp and Gamma

Sp=tfestimate(y2th(:,1),y2th(:,2),[],[],NFFT,48000);

[Gamma,FF]=tfestimate(y3th(:,2),y3th(:,1),[],[],NFFT,48000); %Gamma
    calculated with respect to Microflown
```

```

[Gamma2,FF2]=tfestimate(y3th(:,2),y2th(:,1),[],[],NFFT,48000);   % Gamma
    calculated with respect to Bruel

SpG=abs(Sp(1:NFFT/2));
GammaGMag=20*log10(abs(Gamma(1:NFFT/2)));
GammaGPhase=angle(Gamma(1:NFFT/2))*180/pi;

GammaGMag2=20*log10(abs(Gamma2(1:NFFT/2)));
GammaGPhase2=angle(Gamma2(1:NFFT/2))*180/pi;

GGM=filter(ones(1,100)/100,1,GammaGMag);
GGM2=filter(ones(1,100)/100,1,GammaGMag2);

GGP=filter(ones(1,100)/100,1,GammaGPhase);
GGP2=filter(ones(1,100)/100,1,GammaGPhase2);

SPGM=filter(ones(1,256)/256,1,SpG);



% Computation of Sv

Spmeno1=tfestimate(y2th(:,2),y2th(:,1),[],[],NFFT,48000);
Gammameno1=tfestimate(y3th(:,1),y3th(:,2),[],[],NFFT,48000);



    [mag_best curva]=fitting0411(f,f,SpG);
    curva1=curva';
    % Sv=abs(SpG)./abs(Gamma(1:262144));  %for sweep 3 and sw03cut

    Sv=abs(SpG)./abs(Gamma(1:524288));  %for sweep 1

    %Sv2=abs(SpG)./abs(Gamma2(1:262144));  %for sweep 3 and sw03cut
    Sv2=abs(SpG)./abs(Gamma2(1:524288));  %for sweep 1

    Sv_model=abs(curva1)./abs(Gamma(1:length(curva1)));
    z=zeros(141995,1);
    Sv_model_1=[Sv_model; z];


    [mag_bestv curva_v]=fitting_velocita(f,f,Sv); %%correction of v

```

```
    [mag_bestph curva_ph]=fitting_velocita_FASE(f,f,GammaGPhase); %
        correction of the v phase
```

B.3 Determination of the experimental calibration filter

```
%DETERMINATION OF THE EXPERIMENTAL CALIBRATION FILTER AND COMPARISON TO
    THE
%NORMAL ONE

function [mag_bestcoeff, curva] = fitting(X , f , G )
    % [mag_bestcoeff phi_bestcoeff] = fitting(X , f , G )
    % X: frequency vector on wich the filter is evaluated
    % f: frequency vector of the experimental curve
    % G: experimental curve

%% constants

fmin = 50;
fMax = 5000;


G1 = G;

%%%%%%%%%%% preparation of experimental data for fit %%%%%%%%%

% trasformation of data resolution: from fine band to twelfth-octave

% twelfth-octave frequencies vector
fc = 20;
a = 1;
while fc <=15000
    R12(a,1) = fc;
    fc = fc*2^(1/12);
    a = a+1;
end

clear fc a;

% data filtering: rectangular windows are here used
G12 = zeros(length(R12),1);
for a = 1:length(R12)
    % center frequency
```

```
    Fc = R12(a);
    % lower limit
    f1 = Fc/(2^(1/24));
    % upper limit
    f2 = Fc*(2^(1/24));
    G12(a) = mean(G1(f > f1 & f < f2));
end
% loglog(f,abs(G)/0.053,f,abs(G1)*z0,R12,abs(G12)*z0)

%% Selection of the interval
fGood   =   R12(R12>fmin & R12<fMax);
yGood   =   G12(R12>fmin & R12<fMax);

%% Fit
    %%%%% pressure corner frequencies of the loan probe

    mag_coeff(1) = 61.9;
    mag_coeff(2) = 52;
    mag_coeff(3) = 1;
    mag_coeff(4) = 100000;
%
        %%%%% pressure corner frequencies od the probe mF03
%     mag_coeff(1) = 37.4;
%     mag_coeff(2) = 32;
%     mag_coeff(3) = 44;
%     mag_coeff(4) = 16946;


%% Correction function using the Microflown parameters

% 3 CORNER FREQUENCIES
[~, mag_ystart] =   magfun(mag_coeff,X);

% Calculation of the parameters of the experimental curve
numiter = 500; % number of iterations for the fit
[mag_bestcoeff] =   fminsearch(@magfun,mag_coeff,optimset('MaxFunEvals',numiter),fGood,abs(yGood));

% Correction function with the found parameters
[~, mag_yfit]   =   magfun(mag_bestcoeff,X);

%% Creation of the pressure correction curve
a   =   length(X);

```

```
if  rem(a,2)    ==  0       % CASE 1: odd samples
    Magstart    = mag_ystart(1:a/2+1);
    Mag1        = mag_yfit(1:a/2+1);
    Mag         = [Mag1 ; flipud(Mag1)];
    Mag_start   = [Magstart ; flipud(Magstart)];

else                        % CASE 2: even samples
    Magstart    = mag_ystart(1:(a+1)/2);
    Mag1        = mag_yfit(1:(a+1)/2);
    Mag         = [Mag1 ; flipud(Mag1(2:end))];
    Mag_start   = [Magstart ; flipud(Magstart(2:end))];
end

%%Microflown filter
GStart = Mag_start;

%% Optimal filter
GModel = Mag;


modello250=20*log10(abs(GModel((X>249.9)&(X<250.1))))

mod250max=max(modello250)

    mf250=20*log10(abs(GStart((X>249.9)&(X<250.1))))
    mf250max=max(mf250)

diffmax=mf250max-mod250max


lin_mod250max=max(abs(GModel(250)))
lin_mf250max=max(abs(GStart(250)))

diff_lin=lin_mf250max-lin_mod250max

curva=20*log10(abs(GModel(X<11000)))+diffmax;
%% Plot curves

        f1 = gcf;
        set(f1,'Color',[1 1 1])
        semilogx(R12,20*log10(abs(G12))+diffmax, 'LineStyle','--','
           LineWidth',2,'Color',[0 0.749 0.749])

        hold on
```

```
semilogx(X(X<11000),20*log10(abs(GStart(X<11000))),'r','LineStyle',':', 'LineWidth',2)
semilogx(X(X<11000), 20*log10(abs(GModel(X<11000)))+diffmax,'k', 'LineWidth',1);

hold off

h1 = gca;
xlim([20 10000])
set(h1,'XTickLabel',{'10','100','1000','10000'},...
'XTick',[10 100 1000 1e+004],...
'XScale','log',...
'XMinorTick','on',...
'XMinorGrid','off',...
'MinorGridLineStyle',':',...
'GridLineStyle','-',...
'FontSize',12);
box('on');
grid('on');
%%%%%%%%%%%%%%% Create labels and title
title('Correction curve of pressure','FontSize',18)
xlabel('Frequency [Hz]','FontSize',16);
ylabel('Amplitude [dB]','FontSize',16);

%plot of the linear curves
figure
f1 = gcf;
set(f1,'Color',[1 1 1])
plot(R12,((G12)), 'LineStyle','--','LineWidth',2,'Color',[0 0.749 0.749])

hold on

    plot(X(X<11000),((GStart(X<11000))),'r','LineStyle',':', 'LineWidth',2)

    plot(X(X<11000),((GModel(X<11000)+diff_lin)),'k', 'LineWidth',1);

hold off
h1 = gca;
xlim([20 10000])
set(h1,'XTickLabel',{'10','100','1000','10000'},...
'XTick',[10 100 1000 1e+004],...
```

```
        'XScale','lin',...
        'XMinorTick','on',...
        'XMinorGrid','on',...
        'MinorGridLineStyle',':',...
        'GridLineStyle','-',...
        'FontSize',12);
        box('on');
        grid('on');
        %%%%%%%%%%%%%%% Create labels and title
        title('Correzione curva di pressione sperimentale lineari')
        xlabel('Frequency (Hz)','FontSize',12);
        ylabel('dB','FontSize',12);




%% Function: pressure model
function [out, Y_fun] = magfun(coeff,X,Y) % Amplitude function

        A    = coeff(1)
        fc1 = coeff(2)
        fc2 = coeff(3)
        fc3 = coeff(4)

    % 3 CORNER FREQUENCIES
    Y_fun    = A*(sqrt(1+(X.^2)./fc3^2))./ ...
                (sqrt(1+fc1^2./(X.^2)).* ...
                sqrt(1+fc2^2./(X.^2)));

    if nargin >= 3
        DIFF    = Y_fun - Y;
        SQ_DIFF = DIFF.^2;

        out = sum(SQ_DIFF);
    else
        out = ('funzione utilizzata solo per calcolare curva correzione');
    end
```

Bibliography

[1] P.M. Morse and K.U. Ingard. *Theoretical acoustics*. Princeton University Press, 1968.

[2] D. H. Towne. *Wave phenomena*. 1988.

[3] D. Stanzial, G. Sacchi, and G. Schiffrer. On the physical meaning of the power factor in acoustics. *J. Acoustic. Soc. Am.*, 131:269–280.

[4] D. Stanzial, D. Bonsi, and G. Schiffrer. Four-dimensional treatment of linear acoustic fields and radiation pressure. *Acta Acustica United with Acustica*, (89):213–224, 2003.

[5] F. Jacobsen. A note on instantaneous and time-averaged active and reactive sound intensity. *J. Sound Vib..*, (147):489–496, 1991.

[6] G. Schiffrer and D. Stanzial. Energetic properties of acoustic fields. *J. Acoust. Soc. Am.*, 6(96):3645–3653, 1991.

[7] M. Buiat, G. Sacchi, and D. Stanzial. Visualizzazione sinottica di grandezze energetiche in un'onda sonora piana quasi stazionaria. In *Proceedings of the 39° National Conference AIA*, 2012.

[8] A. Farina. Simultaneous measurement of impulse response and distortion with a swept-sine technique. In *Audio Engineering Society Convention 108*, Feb 2000.

[9] S. M*ü*ller and P. Massarani. Transfer-function measurement with sweeps. *J. Aes.*, pages 443–471, 2001.

[10] D. Bonsi. Risposta all'impulso nei sistemi acustici lineari: aspetti formali ed esempi di applicazione. *Rivista italiana di acustica*, (35):7–15, 2011.

[11] I. Mateljan. *ARTA: Program for Impulse Response Measurement and Real Time Analysis of Spectrum and Frequency Response*, 2014.

[12] G. Cengarle. Applicazione dell'intensimetria per la registrazione e riproduzione del suono: la "quadrifonia acustica". Master's thesis, 2005.

[13] A. Nobuharo. Computer-generated pulse signal applied for sound measurement. *J. Acoust Soc. Am.*, page 1484, 1981.

[14] S. Yôiti, A. Futoshi, K. Hack Yoon, and S. Toshio. An optimum computer-generated pulse signal suitable for the measurement of very long impulse responses. *J. Acoust Soc. Am.*, page 1119, 1995.

[15] H.-E. de Bree. *The Microflown E-book*. 2007.

[16] F. Jacobsen and V. Jaud. A note on the calibration of pressure-velocity sound intensity probes. *J. Acoust. Soc. Am.*, (120):830–837, 2006.

[17] T. Basten and H.-E. de Bree. Full bandwidth calibration procedure for acoustic probes containing a pressure and a particle velocity sensor. *J. Acoust. Soc. Am.*, (127):264–270, 2010.

[18] H.E. de Bree. *TheMicroflown*.

[19] D. Stanzial, G. Sacchi, and G. Schiffrer. Calibration of pressure-velocity probes using a progressive plane wave reference field and comparison with nominal filters. *J. Acoust. Soc. Am.*, (129):3745–3755, 2011.

[20] F. Fimiani, D. Bonsi, P. Bruschi, M. Buiat, M. Piotto, and D. Stanzial. Calibrazione per confronto delle sonde pressione-velocità (p-v): impostazione del problema. In *Proceedings of 41° National Conference AIA*, Pisa, Italia, June 2014.

[21] P. Dickens, J. Smith, and J. Wolfe. Improved precision in measurements of acoustic impedance spectra using resonance-free calibration loads and controlled error distribution. *J. Acoust. Soc. Am.*, 3(121):1471–1481, 2007.

[22] J.P. Dalmont. Acoustic impedance measurement, part i: a review. *J. of Sound and Vibration*, (243):427–439, 2001.

[23] P. Bruschi, F. Butti, and M. Piotto. Cmos compatible acoustic particle velocity sensors. *Sensors, IEEE*, pages 1405–1408, 2011.

[24] M. Buiat, M. Piotto, G. Sacchi, and D. Stanzial. Rapporto tecnico siht a conclusione del primo anno di attività. Technical report, CNR- IDASC and CNR- IEIIT, 2013.

[25] M. Buiat, D. Bonsi, P. Bruschi, and M. Piottoand G. Sacchi andD. Stanzial. Comparison calibration of a pressure-velocity (p-v) tympanometric probe prototype. In *Proceedings of 39° AIA- 40° DAGA Conference*, Merano, Italy, March 2013.

[26] D. M-Donskoy and B. A. Cray. Acoustic particle velocity horns. *J. Acoust Soc. Am.*, 131:3883–3890, 2012.

[27] M. Buiat, D. Bonsi, P. Bruschi, F. Fimiani, M. Piotto, and D. Stanzial. Application of acoustic horns for the amplification of a p-v probe velocimetric signal. In *Proceedings of Forum Acusticum*, Krakow, Poland, September 2014.

[28] A. G. Webster. Acoustical impedance and the theory of horns and of the phonograph. *Proc. Natl. Acad. Sci.*, 5:275–282, 1919.

[29] B. Kolbrek. Horn theory: an introduction, part 1 and 2. *audioXpress*, 2008.

[30] D. M-Donskoyand B. A. Cray. Horns as particle velocity amplifiers. *J. Acoust Soc. Am.*, 130:311–315, 2011.

[31] M. Buiat, D. Bonsi, P. Bruschi, F. Fimiani, M. Piotto, and D. Stanzial. Utilizzo di cornette per l'amplificazione acustica del segnale velocimetrico di sonde p-v. In *Proceedings of 41° National Conference AIA*, Pisa, Italy, June 2014.

[32] *Introduction to acoustics module- COMSOL 4.3*, 2012.

[33] R.D. Kent. *The MIT Encyclopedia of communication disorders*, chapter Tympanometry, pages 558–562. 2004.

[34] K.J. van Camp, R.H. Wilson, D.F. Greten, and J.E. Shanks. *Principles of tympanometry*, volume 24. 1986.

[35] Y.W. Liu, C.A. Sanford, J.C. Ellison, D.F. Fitzpatrick, M.P. Gorga, and D.H. Keefe. Wideband absorbance tympanometry using pressure sweeps: system development and results on adults with normal hearing. *J. Acoust Soc. Am.*, 130(6):3708–3719, 2011.

[36] D. Stanzial, M. Buiat, G. Sacchi, and S. Prosser. Timpanometria a banda larga con microsonde p-v. In *Proceedings of 39° National Conference AIA*, Roma, Italia, July 2012.

[37] D. Stanzial, M. Buiat, and G. Sacchi. Wide band pressure and velocity (p-v) tympanometry with calibrated sound intensity micro-probes. In *Proceedings of Meetings on Acoustics*, Kansas City, Missouri, January 2013.

[38] G. Sacchi. *Calibration of pressure-velocity probes and measurement of sound power and ear canal conductance*. PhD thesis, University of Ferrara, 2011.

[39] G. Sacchi, M. Buiat, F. Fimiani, and D. Stanzial. Monitoring the filling state of capsules using p-v micoprobes. In *Proceedings of 39° National Conference AIA*, Roma, Italia, July 2012.

[40] T. Leephakpreeda. Novel method to weigh medical capsules in continuous process. *Measurement*, 42:1053–1058, 2009.

[41] C.F. Carvalho, C.R. Martins, and M.S. Nunes. Remote train detectrion system. In *Proceedings of 12° International Congress on Sound and Vibration*, Lisbon, Spain, July 2005.

[42] D. Stanzial, G. Sacchi, and M. Buiat. *Campagna di misura Railway Noise*, 2013.

[43] D. Stanzial, D. Bonsi, and M. Buiat. *Condition monitoring di lavatrici*, 2014.

Acknowledgements

This thesis has been made possible thanks to the contribution of the Institute of Italian National Research Council CNR- IDASC and the Deltatech industry in Sogliano al Rubicone (FC, Italy).

First of all I would like to thank Prof. Domenico Stanzial, who has guided me through this path, transmitting to me the passion for research.

Thanks to Prof. Claudio Rafanelli and to Prof. Paolo Bruschi, for agreeing to be my referees.

Thanks to Giorgio Sacchi for his patience, his support and for being a precious colleague and friend.

Thanks to Davide Bonsi for his willingness, for the advices, but also for his congeniality and enthusiasm.

Thanks to IEIIT of Pisa for developing the probe, and in particular to Prof. Massimo Piotto for his constant availability, his patience and for his precious help.

Thanks to Gianni Fondriest, Ivan Fondriest, the municipality of Sogliano al Rubicone, the mayor Quintino Sabattini and the assessor Loredana Zamagni for the precious contribution to the project.

Thanks to Microflown (Arnhem, The Netherlands), and in particular to Prof. Hans-Elias de Bree, to Marcin Korbasiewicz and to Rien Platenkamp, for their kindness and their helpfulness during my visit at Microflown.

Thanks to Roberto Trebbi, eng. Giorgio Tarozzi and Prof. Silvano Prosser for their contribution to the SIHT project.

Thanks to eng. Carlo Urbanet for the availability.

Personally, I would like to thank all my friends for the support and the love throughout these years.

My love and thanks to Nicola, for the understanding and support, and for being my second family.

Last, and most importantly, thanks to my family, my parents Giorgio and Fiorella and my brother Andrea, for the love, the support and for letting me follow my dreams.